Fast and accurate methods to unveil the mechanisms of contrast formation in High Resolution Force Microscopy

Universidad Autónoma de Madrid
Departamento de Física Teórica
de la Materia Condensada

Dissertation submitted to obtain the degree of *Doctor en Física*

Author: Michael Ellner
Supervisors: Prof. Rubén Pérez Pérez / Dr. Pablo Pou Bell

Madrid, May 2018

Table of terms

8–hq 8–hydroxyquinoline.

AFM Atomic Force Microscopy.

AM Amplitude Modulation.

bfA Breitfussin A.

BPPA bis(para–pyridyl)acetylene.

C_{60} Buckminsterfullerene.

CH Constant Height.

CVD Chemical Vapor Deposition.

dAFM Dynamic Atomic Force Microscopy.

DFT Density Functional Theory.

ES Electrostatic.

FM Frequency Modulation.

HR High–Resolution.

KPFM Kelvin Probe Force Microscopy.

LJ Lennard–Jones.

LT Low Temperature.

MD Molecular Dynamics.

MM Molecular Mechanics.

NC Non–Contact.

NTCDI Naphthalenetetracarboxylic diimide.

OpenMX Open source package for Material eXplorer.

PAW Projector-Augmented-Wave.

PES Potential Energy Surface.

PTCDA perylene-tetracarboxylic-dianhydride.

SAM Self–Assembled Monolayer.

SPM Scanning Probe Microscopy.

SR Short–Range.

STM Scanning Tunneling Microscopy.

STMH STMH.

STS Scanning Tunneling Spectroscopy.

SWCNT Single Wall Carbon Nanotubes.

TH Tersoff-Hamann.

UHV Ultra–High Vacuum.

VASP Vienna Ab initio Simulation Package.

vdW van der Waals.

XC Exchange and Correlation.

Contents

Abstract

Frequency Modulation Atomic Force Microscopy (FM-AFM) has become an indispensable tool in nanoscience as it allows to visualize and manipulate surfaces and molecules at the atomic scale. It has been used to characterize 2D materials like graphene on metals with images capturing impressive atomic and topographic details. The technique entered a new era with the use of metal tips decorated with CO molecules to visualize the internal structure of molecules with unprecedented resolution. The contrast enhancement provided by these functionalized tips enabled the identification of unknown organic compounds, imaging intermediate reaction states, discrimination of covalent bond orders, and the visualization of features associated with H–bonds.

Great strides in theory have been made in order to understand the mechanisms responsible for the atomic-scale contrast. On one end of the spectrum, Density Function Theory (DFT) provide the framework to understand the contrast inversion observed in carbon nanostructures images, and the role of the Pauli interaction and tip flexibility in the high resolution (HR) captured by functionalized tips. However, DFT is computationally costly and only a limited number of atoms can be simulated. On the other end, theoretical images can be easily produced with methods based on pair–wise interactions. The interaction parameters are fitted to reproduce the experimental results, and thus, the resulting model can aid in the identification of molecules. In this thesis, we develop three computationally efficient methods that retain the accuracy provided by DFT calculations. First, we introduce a multi-scale potential that is able to describe the mechanical response of large areas of weakly coupled 2D materials probed by a metallic tip. Second, we develop a method to simulate

the contribution of the main interactions –van der Waals (vdW), electrostatic (ES), short-range (SR)– to AFM images taken with flexible close shell probes that includes an accurate description of the ES interaction between the electric field created by CO-metal tips and the charge density of the sample. Third, we modify the previous method to include a description of the SR interaction based on the overlap of the tip and sample charge densities. With these three approaches, we tackle several open questions in the literature regarding: (1) the mechanism behind atomic scale dissipation and atomic scale variations of the mechanical properties of 2D materials; (2) the proper ES description of CO–metal tips; (3) the role played by the ES, SR, and vdW interactions, and the associated tip tilt, on the intramolecular and intermolecular contrast observed on adsorbed molecules with CO probes.

The thesis manuscript is organized as follows: The first chapter describes the basic instrumentation and operation modes of the AFM with a special focus on the ingredients needed to achieve atomic scale contrast. Subsequently, we outline the experimental works that motivate the thesis and describe the current state–of–the–art in HR imaging simulations.

In the second chapter, we study the atomic scale variations of the mechanical response of weakly coupled 2D materials probed by a cantilever based AFM. We present topography and dissipation images that resolve the atoms and the moiré patterns in graphene on Pt(111), despite its extremely low geometric corrugation. The imaging mechanisms are identified with a multi–scale model based on DFT calculations, where the energy cost of global and local deformations of graphene competes with SR chemical and long-range vdW interactions. The simulations show that the atomic contrast of the carbon atoms is related to the SR tip–sample interactions, while the dissipation can be understood in terms of global deformations in the weakly coupled graphene layer. Surprisingly, the observed moiré modulation is linked with the subtle variations of the local interplanar graphene–substrate interaction. We also explore the capabilities of the AFM to achieve sub–surface resolution with a study of single defects on the Pt(111).

The third chapter presents a study of the ES field of CO decorated metallic

tips and its relevance for HR–AFM imaging. With DFT calculations, we investigate the ES field generated by CO molecules in gas phase, as adsorbates on surfaces, and bonded to metallic tips. We postulate that CO tips cannot be described by single dipoles; a proper description takes into account the positive dipole behavior of the metallic apex and the negative charge cloud strongly localized in front of the oxygen atom. This description is incorporated into a model developed in this chapter to simulate rapidly interaction–decomposed AFM images with flexible close shell probes. We validate the model of the tip by reproducing experimental qPlus based images of localized ionic defects (Cl vacancies on a metal–supported NaCl bilayer).

In the next chapter, we focus on H–bonded layers of triazine molecules as probed by CO tips. We describe the changes require in the methodology developed in chapter 3 (for studying surfaces) to simulate molecules. With interaction decomposed images generated by the model, we identify the interplay of the ES, SR, and vdW forces on the contrast formation and discuss the intra– and intermolecular features commonly observed in the images. We also demonstrate the existence of different potential energy surface (PES) minima for the CO tilt and discuss its influence on imaging.

In the fifth chapter, we develop a new methodology to simulate HR–AFM images that puts on equal footing the SR and ES interaction. Whereas the previous method used pair–wise potentials to describe the SR, this one uses the overlap of the charge densities of the tip and the sample. With this, we investigate intra– and intermolecular features observed in AFM images that are closely related to subtle effects in the charge density of the sample. First, we demonstrate that not only structural similar molecules with different stoichiometry provide qualitatively different AFM images, but that the chemical environment (i.e., bonding structure) is also relevant. Second, we pinpoint the Pauli repulsion as the underlying mechanism responsible for the discrimination of covalent bond orders with CO tips. Lastly, the probing of H-bonds with CO tips is investigated.

Resumen

El Microscopio de Fuerza Atómica por Modulación de Frecuencia (FM-AFM) se ha convertido en una herramienta indispensable en la nanociencia por su capacidad para visualizar y manipular superficies y moléculas a escala atómica. Se ha usado para caracterizar materiales 2D como grafeno en metales y las imágenes resultantes tienen detalles atómicos y topográficos impresionantes. La técnica entró en una nueva era con el uso de puntas metálicas funcionalizadas con moléculas de CO para visualizar la estructura interna de moléculas con una resolución sin precedencia. El aumento del contraste proporcionado por estas puntas funcionalizadas ha permitido identificar compuesto orgánicos desconocidos, capturar imágenes de estados intermedios de reacciones, la diferenciación de órdenes de enlaces covalentes, y la visualización de rasgos asociados con enlaces de hidrogeno.

Por parte de la teoría se han hecho grandes avances para intentar comprender los mecanismos responsables del contraste a escala atómica. En un extremo del espectro, la Teoría de la Densidad Funcional (DFT) proporciona el marco para comprender la inversión de contraste observada en las imágenes de nanoestructuras de carbono, y el papel que juega tanto la interacción de Pauli como la flexibilidad de las puntas en la alta resolución capturada por puntas funcionalizadas. Sin embargo, DFT es computacionalmente costoso y solo permite simular un número muy limitado de átomos. En el otro extremo, imágenes teóricas se pueden realizar rápidamente usando métodos basados en interacciones a pares. Los parámetros de las interacciones se ajustan para reproducir resultados experimentales y, por lo tanto, el modelo resultante puede ayudar en la identificación de moléculas. En esta tesis, desarrollamos tres métodos computacionalmente

eficientes que conservan la precisión provista por los cálculos de DFT. Primero, presentamos un potencial multiescala que es capaz de describir la respuesta mecánica de grandes áreas de materiales 2D débilmente acoplados y sondeados por una punta metálica. En segundo lugar, desarrollamos un método para simular la contribución de las principales interacciones – van der Waals (vdW), electrostática (ES), de corto alcance (SR) – a imágenes de AFM hechas con puntas flexibles de niveles cerrados y que incluye una descripción precisa de la interacción electrostática entre el campo eléctrico creado por las puntas de CO-metal y la densidad de carga de la muestra. En tercer lugar, modificamos el método anterior para incluir una descripción de la interacción de corto alcance basada en el solape de las densidades de carga de la punta y de la muestra. Con estos tres enfoques, abordamos varias preguntas abiertas en la literatura sobre: (1) el mecanismo detrás de la disipación a escala atómica y las variaciones a escala atómica de las propiedades mecánicas de los materiales 2D; (2) la descripción electrostática correcta de las puntas de CO-metal; (3) el papel desempeñado por las interacciones ES, SR y vdW, y la flexibilidad de la punta, en el contraste intramolecular e intermolecular observado en imágenes de alta resolución hechas con puntas de CO.

El manuscrito de la tesis está organizado de la siguiente manera: El primer capítulo describe la instrumentación básica y los modos de operación del AFM con un enfoque especial en los ingredientes necesarios para obtener contraste a escala atómica. Posteriormente, describimos los trabajos experimentales que motivan la tesis y describimos el estado actual de la técnica en simulaciones de imágenes de alta resolución (HR).

En el segundo capítulo, estudiamos las variaciones a escala atómica de la respuesta mecánica de materiales 2D débilmente acoplados sondeados por un AFM basado en micropalancas. Presentamos imágenes de topografía y disipación que resuelven lo átomos y los patrones de moiré del grafeno en Pt(111), a pesar de su mínima corrugación geométrica. Los mecanismos de escaneo se identifican con un modelo multiescala basado en cálculos DFT, donde el costo energético de las deformaciones globales y locales del grafeno compite con las interacciones químicas de corto alcance y de vdW de largo alcance. Las simula-

ciones muestran que el contraste atómico está relacionado con las interacciones de corto alcance, mientras que la disipación se puede entender en términos de deformaciones globales en la capa de grafeno débilmente acoplada. Sorprendentemente, la modulación del moiré está vinculada con las variaciones sutiles de la interacción interplanar local de grafeno-sustrato. También exploramos las capacidades del AFM para obtener resolución subsuperficial con un estudio de defectos individuales en el Pt(111).

En el tercer capítulo se presenta un estudio del campo eléctrico (ES) de las puntas metálicas funcionalizadas con moléculas de CO y su relevancia para la obtención de imágenes de HR–AFM. Con cálculos DFT, investigamos el campo ES generado por moléculas de CO tanto en fase gaseosa, como adsorbidas en superficies y unidas a puntas metálicas. Postulamos que las puntas de CO no se pueden describir con dipolos individuales; una descripción adecuada debe de tener en cuenta el comportamiento de dipolo positivo del ápice metálico y la nube de carga negativa fuertemente localizada frente al átomo de oxígeno. Incorporamos esta descripción a un modelo desarrollado en este capítulo para simular rápidamente imágenes de AFM con descomposición de interacciones usando sondas flexibles de niveles cerrados. Validamos el modelo de la punta reproduciendo imágenes experimentales de AFM basadas en qPlus de defectos iónicos localizados (vacantes de Cl en una bicapa de NaCl soportada por un substrato de metal).

En el próximo capítulo, nos enfocamos en capas de moléculas de triacina unidas por enlaces de H sondeadas por puntas de CO. Describimos los cambios requeridos en la metodología desarrollada en el capítulo 3 (para estudiar superficies) para simular moléculas. Con las imágenes generadas por el modelo, estudiamos la competencia que existe entre las fuerzas ES, SR y vdW para la formación del contraste y discutimos las características intra– e intermoleculares que se observan comúnmente en las imágenes experimentales. También demostramos la existencia de diferentes mínimos en la superficie de energía potencial (PES) de la inclinación del CO y discutimos su influencia en las imágenes.

En el quinto capítulo, desarrollamos una nueva metodología para simular imágenes HR–AFM que pone en igualdad de condiciones la interacción SR y

ES. Mientras que el método anterior usaba potenciales a pares para describir el SR, este nuevo método usa la superposición de las densidades de carga de la punta y la muestra. Con esto, investigamos rasgos intra– e intermoleculares observados en las imágenes de AFM que están estrechamente relacionados con efectos sutiles en la densidad de carga de la muestra. En primer lugar, demostramos que no solo las moléculas estructuralmente similares con estequiometría diferente proporcionan imágenes AFM cualitativamente diferentes, sino que el entorno químico (es decir, la estructura de enlaces) también es relevante. En segundo lugar, identificamos la repulsión de Pauli como el mecanismo subyacente responsable de la diferenciación de los órdenes de los enlaces covalentes con puntas de CO. Por último, se investiga el sondeo de enlaces covalentes con puntas de CO.

1 High Resolution Atomic Force Microscopy

Over the last two decades, technological developments have permitted the Atomic Force Microscopy (AFM) to image surfaces and molecules with details that go beyond atomic resolution. By this we mean, extra atomic–scale information in addition to the position of the atoms. Such details seem to be linked to specific properties of the sample, for instance, the chemical species of individual atoms, sub–angstrom topographic corrugations, local contact potential differences, local mechanical stiffness, and the order of covalent bonds. Although capturing any of these details could be called "high resolution" imaging, the literature reserves this term for the probing of samples with mobile functionalized tips. Specifically, CO–terminated tips produce such sharpness that images of molecules record intra– and inter–molecular features that resemble their bond structure.

The outstanding improvement in the quality of the images call for detailed theoretical studies in order to help discern the origin of the features, pinpoint the underlying interactions responsible for the contrast, and understand the properties of the sample it reflects. In this thesis we study a wide variety of experimental setups that capture such details. The experimental setups include AFMs with large amplitude cantilever and AFMs with small amplitude qPlus sensors, tips terminated in metallic apexes and CO functionalized tips, and both molecular and surface samples.

In this chapter we give a brief description of the experimental apparatus needed to capture images with details beyond the atomic resolution (sec. 1.1). Then, we present the experimental results that motivate this work (sec. 1.2) and the state–of–the–art of the theory (sec. 1.2.3). At the end of the chapter, an

overview of the thesis is given (sec. 1.3).

1.1 The AFM basics

Scanning Probe Microscopy (SPM) is an experimental technique that makes possible the imaging of a surface or molecule in real space. A physical probe, in the form of a sharp tip attached to a piezoelectric actuator, comes very close to the sample and collects data. By raster scanning the sample, the collection of data points creates the image. The data can have different forms depending on the type of SPM. The two original and most popular forms are the Scanning Tunneling Microscopy (STM) [1] and the AFM [2, 3]. The former uses the tunneling current induced by a bias voltage applied between the tip and a semi–conductor or metallic surface and the latter senses the force between the tip and the sample. The force is measured indirectly by mounting the tip on a lever and monitoring its motion.

Although in principle both techniques are capable of reaching atomic resolution, the AFM is more versatile. In contrast to STM, the AFM works with non-conductive surfaces and senses all the electrons in the sample (not just at the Fermi level). In addition, the AFM's experimental setup can be modified to image different types of interactions and thus collect different properties of the materials. However, the experimental setup and the interpretations of AFM images is much more challenging. This is especially true for High–Resolution (HR) imaging where, in addition to atomic resolution, very subtle characteristics of the sample are captured.

In what follows, we briefly outline the basic instrumentation aspects of the AFM; these have been widely covered in the literature [4–7]. Fig. 1.1 shows the most basic scheme of an AFM. The sample under study is mounted on a piezo translator that changes the relative position between the tip and the sample. Movements in the $x-y$ direction are used to create a 2D image and z–direction movements to control the tip–sample distance. Originally, the translators were made of a piezo tripod [1], but now, tube scanners are more widely used [8]. The probe or tip that interacts with the sample is mounted on one end of a force sensor. This can be a self–sensing sensor like the qPlus or a traditional

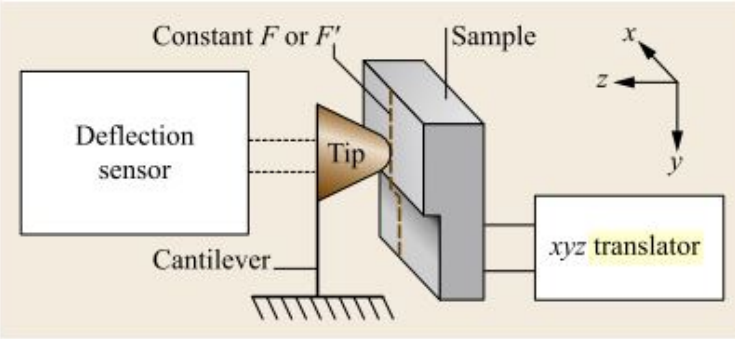

Figure 1.1: Principle of operation of the AFM. The sample which is mounted on a piezoelectric scanner is scanned against the tip and the cantilever deflection is measured. Reproduced with permission from [7].

microcantilever. With the latter, an external setup to measure the cantilever deflection is needed, most typically, a beam deflection system. The tip–sample interactions are determined from the deflection of the cantilever, either directly, or indirectly through its dynamics. The measured deflection is used by the unit control system to make adjustments on the operational parameters of the AFM.

Measuring the cantilever displacement is not an easy task because the deflections can range from 100 nm to 0.1 nm. To accomplish this, several experimental setups have been used. The original AFM experiments used an STM head [1] mounted on top of a cantilever whose top part (opposite to the tip) had a metallic coating [3]. This worked as the conductive surface for the STM "experiment" that measured the tunneling current (and thus the cantilever deflection) between the STM tip and the AFM cantilever. Other successful setups to measure the deflection include capacitance detection [9] and optical techniques such as optical interferometry with [10] and without optical fibers [11, 12], optical polarization detection [13], laser diode feedback [14], and the most widely used technique of optical laser beam detection [15]. In this last setup, a laser is reflected on the vertex of the cantilever onto a split photodetector with four quadrants. It is a fairly simple setup to implement yet it has many advantages compared to the other methods: it has a large working distance, it is insensitive

to distance changes, and it also reports angular changes of the cantilever (and thus lateral forces).

The easiest way to operate the AFM is in contact mode. In this mode, the tip is raster–scanned along the surface in either Constant Height (CH) or constant interaction mode. In the former, the tip height is kept constant and the deflection of the cantilever is measured directly. In the latter, which is a more common mode, the deflection of the cantilever is kept constant using a feedback loop that modulates the tip height through a piezoelectric actuator. Though simple to perform, the contact mode is invasive and atomic resolution is nearly impossible to achieve [16].

1.1.1 Dynamic AFM

In Dynamic Atomic Force Microscopy (dAFM), an external excitation is applied on the force sensor in order to diminish tip–surface contact. This is an important ingredient for HR imaging. There are two modes of dAFM. In Amplitude Modulation (AM)–AFM, the cantilever is vibrated at a fixed frequency and excitation amplitude at the same time that the cantilever amplitude and the phase are read. In Frequency Modulation (FM)–AFM, the cantilever is vibrated at a fixed cantilever amplitude and a fixed phase (90°phase difference with respect to the excitation), and the frequency shift and the excitation amplitude are read. Although both modes diminish the tip and sample contact, only the latter guarantees that the cantilever remain in the regime of attractive interactions. For this reason, this non-destructive mode is sometimes referred to as Non–Contact (NC)–AFM [17].

Amplitude modulation

In AM–AFM, the external signal that excites the cantilever is kept fixed, both in amplitude and frequency. In order to maximize the sensitivity of tip–sample interactions, the cantilever is driven at its natural frequency (the first eigenfrecuency of the cantilever in the absence of the tip–sample interaction). At this frequency, the phase difference between the excitation signal and cantilever response is $\pi/2$ and the cantilever oscillates at its maximum amplitude. The

response of the cantilever to an external quasi–static tip–sample interaction is to diminish the amplitude of the cantilever and to change the phase difference with respect to the excitation signal. While scanning the surface, a constant height map can be obtained by directly recording the change in the amplitude (ΔA) of the cantilever. More commonly, a z–feedback loop is used to change the tip–sample distance while keeping the amplitude of the cantilever constant to obtain a topographical image of the sample. However, both types of maps require accurate measurements of the amplitude of the cantilever that, in the absence of environmental damping (i.e. air or a liquid buffer), are timely. The tip–sample interaction distorts the dynamics of the cantilever and provokes transient regimes that for typical AM–AFM cantilevers in Ultra–High Vacuum (UHV) reach $\sim$2 s (bandwidth of 0.5 Hz) [5, 18]. With such high transient times, it is virtually impossible to create an image in UHV.

The AM–AFM solves many problems that arise in static and semi-static modes. Mainly, the oscillation diminishes the tip and sample degradation due to lateral forces caused by adhesion and by jump–to–contact instabilities [19]. On limited scenarios, this operational mode can achieve molecular resolution in air [20] or atomic resolution in liquid [21]. However, it is not capable of reaching atomic resolution in a consistent way, much less to produce HR images. The main limitation is, as described above, that the AM–AFM is incompatible with the UHV (i.e., vacuum) needed to preserve the integrity of the tip and the sample and to increase the sensitivity of the measurements. Furthermore, at the close tip–sample distances needed to probe individual atomic information of the sample, the tip–sample interaction energy is so great that it becomes comparable to the elastic energy of the cantilever. This produces instabilities in the oscillation dynamics of the cantilever.

Frequency modulation

The second and more sophisticated dAFM operational mode is FM–AFM. Here, the excitation of the cantilever is not kept constant. Rather, it is generated from the response of the cantilever using an FM demodulator. Typically, the cantilever is first made to oscillate near its natural frequency and then a phase-

lock loop generates a signal that is proportional in amplitude to the cantilever motion but dephased by $\pi/2$. An automatic gain control circuit modifies the amplitude of the signal to ensure that the cantilever oscillates at a fixed predetermined amplitude. The tip–sample interaction modifies the resonance frequency of the cantilever, however, using the dephased signal as the input excitation keeps the cantilever oscillating in resonance [22]. The shift in resonance frequency (referred to as frequency–shit Δf) is the key figure in FM–AFM. The main advantage of this mode (as compared to AM–AFM) is precisely that the cantilever is kept oscillating at resonance and thus transient times are negligible also in UHV. With the increase in the quality factor of the cantilever gained by keeping the microscope in vacuum, Δf differences of 5 mHz can be detected while keeping the bandwidths as high as 500 Hz [5]. As a result, the acquisition of images with atomic contrast on a regular basis becomes feasible. In addition, by keeping the oscillation amplitude constant, the feedback loop ensures that the elastic energy of the cantilever is much larger than the tip–sample interaction ($F = kA \gg F_{\text{int}}$) and thus the tip is able to approximate the surface more than in AM–AFM. This opens the possibility of accessing the individual atomic information required to produce HR images.

Different kinds of maps can be recorded in FM–AFM. For CH images, the tip is placed at a fixed distance and the Δf is recorded on a 2D grid. In contrast, a z–feedback loop can be used to control the tip height while keeping Δf constant. This produces a topographic image of the sample. However, this mode is usually unsuitable for HR imaging because the z–feedback loop only works correctly on positive slope frequency shifts. Specifically, all the images with intra–molecular contrast [23] obtained with reactive mobile probes are captured in CH mode where crossing points to negative slope Δf are readily available.

Typical 2D maps are created by moving the tip line by line. The line direction defines the fast scan direction and the perpendicular defines the slow scan direction. More sophisticated data acquisition methods use data from different planes. In order to compare images at different tip–sample distances (or Δf set points), it is useful to record the images simultaneously. This is done using the second pass method where lines in the fast directions are recorded at two differ-

ent heights (or set points) before moving the tip in the slow scan direction. Using this technique, one ensures that the two images are recorded without structural changes of the tip or the sample. Related to this, the multipass method [24] records an image in two passes. In the first, a topography image is acquired at a large tip–sample distance and in the second pass, the tip is moved close to the sample and the profile of the first pass is used to feed the z–piezo during the scan. This is useful for imaging nonplanar molecules and 3D surfaces [24]. Recent technological advances [25] enabled the recording of volumetric data in AFM (3D force field spectroscopy) from which 2D maps and interaction curves can be extracted [26].

1.1.2 Force sensors

The most important element of the AFM is the force sensor that probes the small forces between the tip and the sample [27]. Originally, dAFM modes used Si microcantilevers with stiffness constant between 10 and 43 N/m. In principle, the spring constant of the cantilever should be as small as possible in order to maximize the range of frequency shift. However, the cantilever must be as stiff as possible in order to prevent the probe from snapping into the surface [15] due to long–range forces. Initially, the oscillation amplitudes needed to achieve atomic lateral resolution were discerned empirically. They varied between 1.5 and 40 nm and allowed imaging metallic and semiconducting surfaces [28–31, 31–35] with true atomic resolution.

Upon studying systematically the optimal imaging parameters for atomic resolution, Giessibl *et al.* [36] concluded that the signal–to–noise ratio could be increased by up to two orders of magnitude by using stiffer cantilevers and smaller amplitudes than the ones allowed by Si cantilevers. Additionally, reducing the amplitude is crucial for optimizing sensitivity to Short–Range (SR) forces [36]. These were the main motivations for the creation of stiffer force sensors based on quartz crystal resonators that enable sub–angstrom amplitude measurements. They are made from a quartz tuning fork similar to the ones used in high precision watches [37]: two coupled parallel quartz tines that oscillate out of phase. However, for AFM the two coupled modes used for time keeping are

not needed and thus one prong of the fork is fixed to the base of the mount. The enhanced sensitivity to the SR forces is not the only advantage of quartz resonators. In contrast to Si cantilevers which require an external setup to measure deflections, these resonators are self–sensing. The external setup typically used with Si cantilever, optical laser beam detection [15], requires a more complicated scheme that is hard to implement in Low Temperature (LT)–UHV conditions.

Another advantage to using quartz resonators is its stability with respect to changes in temperature. In FM–AFM, the most important quantify, Δf, is obtained from the natural frequency of the cantilver. While f_0 of Si cantilever changes around 35 ppm per K [38], on quartz resonators it changes less than 1 ppm per K [27].

Although images with impressive detail have been acquired with high amplitude measurements in surfaces, and in limited cases, in molecules [24, 39], the switch to stiff force sensors and small oscillation amplitudes was crucial for imaging the internal structure of molecules [40].

1.1.3 Ingredients for atomic resolution: LT, UHV, and a sharp tip

The first images obtained with the AFM were of the graphite surface [41]. These showed periodic lattices without point defects and thus clearly did not have true atomic resolution. The common explanation of these experiments is that the surface was sensed with a blunt tip with many contact points that average out the details of the defects. Several advances in instrumentation were required before obtaining true atomic resolution. First, it was necessary to operate the AFM in FM mode which, as described before, allows non–invasive imaging of the sample. Second, it was imperative to perform the experiments in a controlled environment. This refers to LT [42], typically the 5 K achieved by a liquid helium cryostat, and UHV [15, 43] ($\rho \sim 10^{-10}$ mbar). This ensures clean and stable experimental conditions [44] for the tip and the sample. Lastly, advances in the fabrication of sharp tips were critical.

There are several motivations for keeping the whole microscope system (tip, sample and electronic apparatus) submerged on a constant LT thermal bath. The thermal bath keeps the microscope at a constant temperature which reduces

thermal fluctuations. This is important for reducing thermal drift of the sample and for stabilizing the natural frequency of the cantilever. If the thermal bath is of LT (mostly referring to liquid helium temperature), then the experimental setup favors not only from a further reduction of the thermal drift but also a reduction of the thermal noise of the experimental apparatus, a reduction of piezo relaxation or creep, and an increase in the stability of the tip and the sample. An additional advantage of keeping the AFM at LT is that many interesting phenomena in the nano– and atomic–scale occur at these temperatures. For full reviews on LT–SPM refer to [45, 46].

The most important condition to obtain atomic resolution is the size of the tip. It must have a similar size to the sample's features that one seeks to visualize. For atomic resolution, the tip needs to have atomic size. However, in practice, the whole tip contains a "macroscopic tip" (with size ranging from several nanometers to tens of nanometers) and a "nanoscopic tip" which is the atomically terminated apex. Consequently, the forces sensed by the AFM have long–range components due to the macroscopic tip–sample interactions, including van der Waals (vdW), Electrostatic (ES), magnetic, adhesion, hydrodynamic, capillary, and contact potential. They do not provide atomic contrast and need to be reduced as much as possible because they can compensate for changes in the SR interaction and reduce the sensitivity to the atomic contrast. This is done by operating the AFM in a controlled environment (LT–UHV), and by increasing the sharpness of the nanoscopic tip. This effectively increases the separation between the macroscopic tip and the sample. The remaining long–range forces provide a common attractive background that is typically subtracted from the reported results.

The interactions that have short ranges provide the atomic contrast. These come from the nanoscopic tip (the few atoms closest to the sample) and include ES, Pauli repulsion, chemical bonding, and London dispersion forces (referred to as vdW). Unless explicitly stated, in this thesis we refer to the "nanoscopic tip" as just "tip".

A way to create an atomically sharp tip is through tip functionalization. It consists of picking up a molecule or atom from the surface and attaching it to the

tip apex. Specifically, tip functionalization with a CO molecule, in combination with small amplitude self–sensing sensors [37], has virtually revolutionized the field of NC–AFM by not only yielding atomic contrast, but in many instances, producing HR images of molecules that display atoms and bonds as in their textbook sketches [40].

Before its use in NC–AFM, CO molecules were extensively studied with STM. The adsorbed molecule was imaged with a bare metal tip [47] and lateral atomic manipulation techniques [48] were used to induce single adsorption site hops away from the tip [49]. More importantly, Bartels *et al.* [47] described a reliable procedure for controlled vertical transfer of a single CO molecule between a Cu(111) surface and an STM tip. The transfer procedure is complicated because the molecule is adsorbed upright on the Cu(111) on a top site [50] with the carbon atom bonded to the surface. A CO molecule has a similar adsorption geometry on isolated Cu atoms adsorbed on Cu substrates [51], and thus the molecules has to flip around when being transferred vertically. For the transfer, first, a metallic tip is positioned on top of a CO molecule using a sample bias of +2 V with a typical current of 1 nA. The feedback–loop used to maintain constant tunneling current is turned off and the sample voltage is increased to +3 V. Subsequently, the voltage is decreased to 0 V while decreasing the tip–sample distance by 0.1 nm to compensate the decrease in current. The process takes a few seconds and has a yield of over 50%. This vertical manipulation of CO molecules on Cu(111) by an STM tip originates from a single electron excitation process of the CO-2π* resonance [52]. Later, CO decorated tips were used in STM imaging to discern adsorbed CO molecules from adsorbed oxygen atoms [47]. More recently, it was also shown that CO tip functionalization enhances resolution of molecular orbitals in STM experiments [53].

The key to the success of the CO functionalized tips in NC–AFM is twofold: as a tip, it has an extremely sharp termination, and it is quite inert. The CO molecule is roughly 112.8 pm long and bonds to the metallic apex leaving a separation between the carbon and the metal of 190 to 290 pm. Consequently, the macroscopic part of the tip is pushed back over 300 pm. This greatly reduces the long–range forces that hinder the atomic contrast.

The inertness of the tip is inherited from the inertness of the CO molecule. Thanks to it, the tip can be approximated to the sample close enough in order to probe with SR interactions. However, it also means that the CO molecule forms a weak bond with the meal apex, resulting in a moiety that can tilt easily. Due to the tip flexibility, the images have appreciable distortions [40].

With the motivation of eliminating image distortions, Mönig *et al* [54, 55] investigated the contrast produced by an oxygen atom rigidly connected to a copper probe (Cu–CuO tip). The O–terminated tip is produced simply by crashing a pure Cu tip into the oxide domain of a partially oxidized Cu(110) [56] surface. The strong covalent binding between the O termination and the Cu apex results in a tip with high chemical and structural stability and chemical inertness. The authors argue that, compared to the CO–terminated tip, the Cu–O tip is fairly rigid and that the images have no artifacts due to tip flexibility. With this tip, submolecular resolution on the organic DCLN molecule [54] and dense monolayer films of atomically precise graphene nanoribbons [57] has been obtained.

HR–AFM images have also been acquired with atomic Br–, Cl–, and Xe–terminated tips [58–63]. This last one is an important probe particle because it can have different dipoles (or effective charges) [62] depending on the configuration and chemical nature of the metal apex [64] and the attachment coordination. Hapala *et al* [62] suggested that by comparing images obtained from tips with different effective charges, the ES potential of the sample can be discerned.

In addition to atomic and diatomic molecular tip terminations, more complex molecules have been used to produce HR–AFM images[23, 65–67]. Sweetman *et al* [66, 67] reported spontaneous tip functionalization of an Si coated tip by Naphthalenetetracarboxylic diimide (NTCDI) molecules. The orientation of the molecule was discerned through inverse imaging [68, 69] and Density Functional Theory (DFT) calculations. With this tip, for the first time a molecule (NTCDI) was imaged with intra–molecular contrast on a reactive semiconducting surface, Ag:Si(111)-($\sqrt{3} \times \sqrt{3}$)R30° [67]. What is more, even subtle distortions to the molecular structure produced by different chemisorptions of the molecule onto the substrate were observed [23]. The tip also resolved inter–molecular features

in a hydrogen–bonded assembly of NTCDI molecules [66]. The authors argue that there is no significant difference between the NTCDI–terminated tip and the CO–terminated tip.

1.1.4 Non-conservative forces: dissipation

As mentioned in sec. 1.1.1, there are additional channels (to the Δf) of data available in AFM measurements and an important one is the dissipation or damping signal. Physically, dissipation indicates a hysteresis in the approach and retraction tip path due to nonconservative tip–sample interactions [70, 71]. In FM–AFM, where the oscillation amplitude of the cantilever is kept constant, the dissipation is the extra energy needed by the piezo actuator to keep the amplitude of the cantilever constant. In general, the damping is less understood than the Δf signal [5]. It has qualitative features that are hard to describe and quantitative orders of magnitude that sometimes cannot be reproduce from *ab intio* calculations, at the same time, the actual measurements are hard to reproduce [72]. However, it can offer valuable information both at the micro and atomic scales.

In contact mode, stick–slip processes are the microscopic origin of dissipation [5]. Lateral forces that build up while the tip sticks to an atomic site are stored as energy and then released when the tip slips to a new relaxed positions. The energy is transformed into phonons, electronic excitations and irreversible deformations of the sample.

The picture for dAFM is more complex. In principle, the technique preserves the integrity of the tip and the sample and it is not as obvious that damping should occur. However, early in the NC–AFM literature, dissipation measurements were reported in layered GaAs/AlGaAs semiconductors heterostructures [73]. The dissipation was localized, yet non-atomic, and was induced by an applied voltage between the oscillating lever and the sample. It generates energy losses (or Joule dissipation) due to currents [74]. More interestingly, the NC–AFM resolves atomic–scale variations in the dissipation. This was first shown on the Si(111)-7 $\times$ 7 surface with dissipation signals that had an inverted contrast with respect to Δf [75]. Atomic–scale variations in the dissipation have also

been observed in ionic surfaces [76], and graphite [77]. In this last case, there is a characteristic plateau in the evolution of the dissipation signal with respect to the tip–sample distance. Although initially macroscopic dissipation mechanisms were suggested to explain the atomic dissipation [5, 75], it is now well established that the signal is mediated by SR interactions and that the underlying processes can be described at the atomistic or molecular level [70, 71]. Inaccessibility of some solutions of the cantilever equation of motion [72, 78] due to variations of the tip's state [79, 80] or single atomic contact adhesion [71] provoke the tip to take different attraction and retraction paths while probing the surface. Using transition state theory [81], Kantorovich *et al.* [70] described a general theory that explains how the bistabilities in the Potential Energy Surface (PES) lead to temperature dependent atomic–scale dissipation images.

1.2 FM–AFM state of the art

In what follows, previous works that motivate this thesis are reviewed. In sec. 1.2.1 we discuss experiments of graphene on metals with a special focus on the limits of vertical precision of the AFM. This is important for the work developed in chapter 2 where we study low–corrugated graphene on Pt(111) moirés. In sec. 1.1.1 HR–AFM measurements with CO–fuctionalized tips are discussed. We review experiments that observe the internal structure of molecules, bond order discrimination, inter–molecular features, and molecular identification. This is relevant for the work developed in chapters 3- 5 where we study the contrast formation of HR–AFM images with CO decorated metallic tips. Lastly, in sec. 1.2.3, we review the most important simulation methods for FM–AFM.

1.2.1 Graphene on metals

Atomic–scale characterization is of utmost importance in the fabrication of technological devices based on low–dimensional materials. Among these, fullerenes, nanotubes, graphene, and carbon nanoribbons are promising candidates to lead the next technological revolution due to their unique electronic and

mechanical properties. FM–AFM experiments on carbon–based materials [82–89] show atomic contrast in Δf images and, depending on the setup, in the dissipation channel. While the Δf contrast has been linked to the nature of the tip–sample interaction [90], the origin of the dissipation is not well understood.

Due to its bidimensional nature, for most applications, graphene is grown or placed on a substrate, most commonly a metal. This effectively tunes the properties of the carbon material due to the interaction with the metal [91, 92]. The interaction strength varies widely, from the strong coupling with Rh [93, 94] and Ru [95], to the weak limit (Ir [96], Pt [97]), where graphene retains its unique electronic properties [98]. The different lattice parameters of graphene and the metal underneath are accommodated through the formation of commensurate structures known as moiré patterns, where C atoms become inequivalent due to their different bonding configuration with the metal. The resulting "true" topographic corrugation of graphene –the difference in height among the topmost and the bottom C atom– varies widely, even in the weakly interacting cases, where it ranges from ≈ 50 pm on Ir [99, 100] to practically flat (≤ 3 pm) on Pt [97]

While STM can easily resolve these moiré patterns, even in the case of graphene/Pt [101], AFM experiments have only been reported in highly corrugated cases as Ru [102], Rh [103], and Ir [88, 104]. Focusing on the most challenging case, graphene/Ir, experiments with a Kolibri sensor using a W tip clearly resolved the moiré in CH–AFM images [104]. Measurements with a qPlus sensor using both inert (CO–terminated) and reactive metallic tips [88] were able to identify the atoms with both tips at any tip–sample distance. In both works, the AFM contrast of the moiré was attributed to differences in the height and interaction strength of different areas of the moiré.

According to this analysis, low–corrugated moirés, like the quasiflat graphene on Pt(111), pose an insurmountable challenge for AFM imaging. In the absence of a large topographic corrugation, we have to resort to subtle differences in the electronic and mechanical properties of the individual C atoms induced by the different interaction with the metal substrate. STM on graphene/Pt(111) has resolved several moiré patterns [101], whose large apparent corrugation arises

from a purely electronic effect [97]. On the mechanical side, AFM has been extensively used to explore the local mechanical properties of materials [105, 106], but with lateral resolutions up to the nanometer scale [102, 107].

1.2.2 HR with CO decorated metal tips

Resolving the atomic structure of surfaces and molecules is the primary goal of surface microscopy [17, 108, 109]. STM is able to image atomic–scale features on surfaces, but resolving single atoms within an adsorbed molecule remains a challenge due to the sensitivity of the tunneling current to the LDOS. In principle, classical cantilever based AFMs with metallic or semiconducting tips sense all the atoms of the sample, independent of their electronic occupancy. Indeed, in simple cases, the AFM records all the atoms of the system; for example, and in contrast to STM, at low bias the AFM is able to image the honeycomb lattice of a graphene bilayer. However, the large oscillation amplitudes diminish the sensitivity to SR forces [36] and these carry the atomic contrast information. Also, these tips tend to have high reactivity and large radii, both of which translate into large attractive forces that impede the tip from reaching the SR distance range. Both of these things changed with the invention of small amplitude force sensors and CO tip functionalization.

The internal structure of molecules

NC–AFM entered a new era with the combination of qPlus sensors and metal tips decorated with CO molecules. With this combination, Gross *et al.* [40] demonstrated the imaging of the pentacene molecule with an unprecedented HR (fig. 1.2). While the CO molecule only slightly affects the STM image (compared to the bare metal tip [110]), the AFM images resembled the textbook–like sketches of the molecule. The internal structure of the molecule is captured at very close tip–sample distance where Pauli repulsion is the dominant interaction and the tip senses high charge density areas: the atomic sites and the covalent bonds. Although the CO molecule is bonded to the metal apex, the lateral spring constant associated with this bond is small. Thus, at high charge

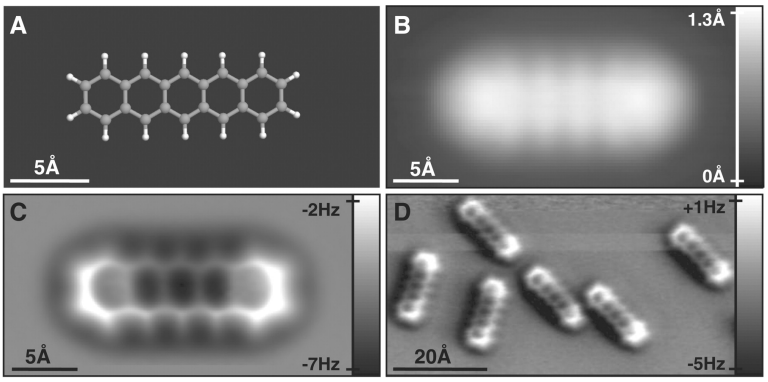

Figure 1.2: STM and AFM imaging of pentacene on Cu(111). (a) Ball-and-stick model of the pentacene molecule. (b) Constant-current STM and (c and d) CH–AFM images of pentacene acquired with a CO tip. Reproduced with permission from [40].

density positions, the CO tilts towards more energetically favorable areas. In this way, the mobility of the CO molecule enhances the PES saddle lines and reveals bond–like features in the image.

The contrast enhancement provided by these non–reactive closed shell probes has made it possible to unveil the molecular structure of natural compounds [111], small metallic clusters [112], and even complex molecular mixtures like asphaltines which pose a challenge for classical structural analysis [113]. Although it is a very demanding technique, HR imaging is now a common practice [24, 39, 40, 54, 58, 59, 62, 63, 65–67, 111, 113–159].

Bond order discrimination

In this section we review a seminal work on bond order discrimination on the Buckminsterfullerene (C_{60}) with CO decorated tips [119]. The motivations is twofold. First, it is an extension of the imaging of the internal structure of molecules where subtleties of the charge density of the system are reflected on the images. We use the results from this experiments to test a HR–AFM simulation method developed in chapter 5. Second, it is an ideal experiment to explain how the CO tilt affects the contrast of the images.

The enhancement provided by mobile closed shell tip functionalization go beyond the ability of imaging the skeleton of the molecule. The tilt–induced sharpening along the covalent bonds that enhances the resolution is actually different depending on the strength of the bond. This is measured by the bond order which is an important concept to predict the geometry, stability, aromaticity, reactivity, and electronic structure of covalently bonded molecules. The bond order also determines the bond length, which is roughly the distance between the bonded atoms; in general, it decreases with increasing Pauling bond order. Gross *et al.* [119] showed that the different bond orders of individual C–C bonds in the C_{60} molecule can be distinguished by NC–AFM with CO tips. The bond arrangement of the hexagon face of the molecule have alternating single and double bonds. On these bonds, the Δf images capture differences in interaction strength (best observed in fig. 1.3(c)) and, more strikingly, in bond length (best observed in fig. 1.3(d,e)). The greater electron density in bonds of higher bond order lead to a stronger Pauli repulsion, which enhanced their brightness in HR–AFM images. As expected, the apparent bond length in the AFM images decreased with increasing bond order. However, they are slightly shifted to the outside of the molecule and the difference in lengths are overestimated.

The apparent bond length and its placement is explained by the tilting of the CO molecule at the tip apex. A rigid probe would sense the highest forces on the line joining the atoms. Lateral forces provoke the CO to always tilt inwards due to a the strong vdW exerted by the large molecule. As the CO approaches the molecule, the lateral Pauli repulsion compensates the vdW attraction, resulting in less tilt towards the molecule. At a point before the bond, the CO rapidly increases its tilt (towards the molecule) so as to overpass the high density area at the bond. The tilt at the turning point is larger on the side of the stronger bond (more repulsion). As the position of each pixel in the image is determined by piezoelectric movement and not the CO tilt, the bond appears in the image at the turning point – the piezo position where the tilted CO detects the greatest repulsion. Furthermore, because of this mapping of the coordinates, variations in the degree of tilt translate into image distortions, with increasing tilts becoming image compression and decreasing tilts expansions along the tilt direction. Thus,

the larger tilt induced by the stronger bond causes the apparent bond to appear shifted further away from the molecular center, resulting in a decreased length as compared to the weaker bond.

Note that the difference in bond lengths are overestimated (differences of $\sim 30\%$ compared to expected differences of $\sim 5\%$). Paradoxically, this is a consequence of the tip property that is responsible for the high sharpness in the HR images: the high mobility of the CO tip. Indeed, recent experiments with a CuO tip [54], a more rigid close shell probe, report more accurate bond length differences [55] with the trade off of recording blunter images.

Inter–molecular features

Previous we examined how the contrast enhancement provided by CO functionalized tips result in images with intra–molecular features that are associated with covalent bonds, and even to discriminate their bond orders. The next logical question is whether these tips can capture inter–molecular features associated with inter–molecular bonds (by nature of weaker strength than covalent bonds).

The arrangement of molecules and supramolecules assemblies depend on a delicate balance of molecule–substrate and molecule–molecule interactions. Understanding these inter–molecular interactions, which include H–bonds, dipole–dipole, vdW, and ES interactions, is of particular importance in surface science. After demonstrating that intra–molecular features obtained with NF–AFM can provide insight into their associated intra–molecular bonds [119], the question becomes, can insight into inter–molecular bonds be gained by imaging inter–molecular features?

The first images with inter–molecular features captured with a CO probe was presented by Zhang *et al* [123] in assemblies of 8–hydroxyquinoline (8–hq) molecules deposited on Cu(111) (fig. 1.4). As expected, they show the internal structure of each molecule and the associated tip–induced distortions. In addition, the images of the aggregates reveal bonding–like features between adjacent molecules in positions where H-bonds are expected. The authors rationalized the features in terms of the charge redistribution that occurs during the bond

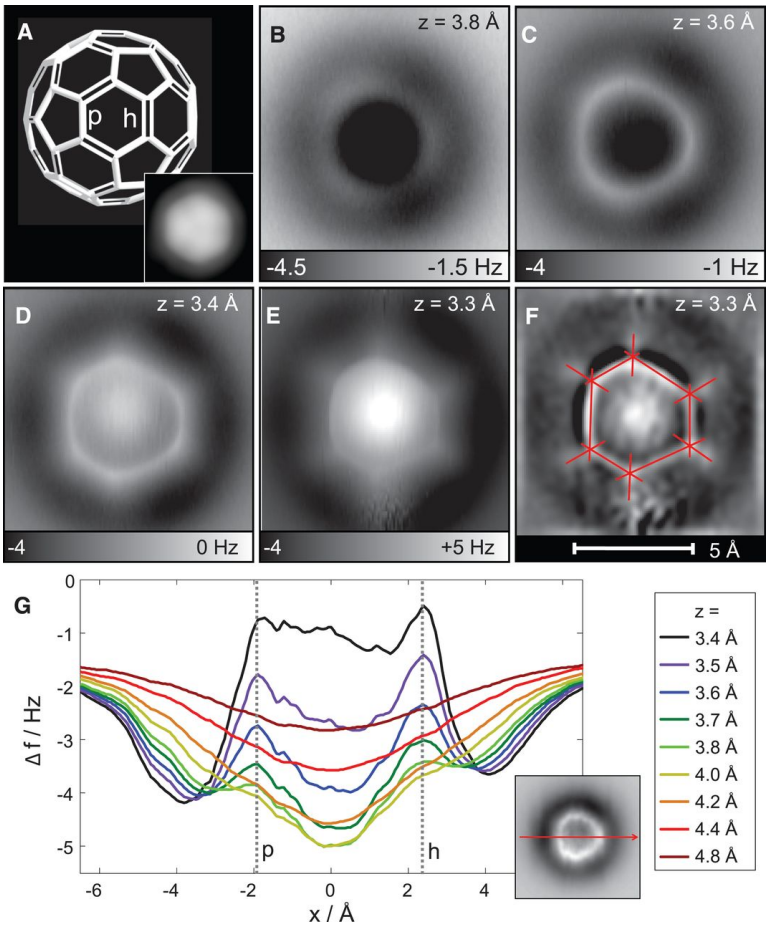

Figure 1.3: Bond–order discrimination of C_{60}/Cu(111) with CO tips. (a) C_{60} model showing the single bonds fusing a pentagon and a hexagon (p) are the double bonds fusing two hexagons (h). The inset shows an STM image. (b-f) Δf images for different tip–sample distances. (g) Line profiles across a p and h bond. Reproduced with permission from [119].

formation. In the same way that the CO tilt sharpens intra–molecular features associated with covalent bonds, the CO tip is capable of detecting the subtleties in the charge density of the H–bond. According to this interpretation, rigid passivized apex [54] could have real access to the H–bonds in the same way it does for bond order discrimination [55].

Newer images with inter–molecular features [66, 123, 132, 146, 155, 160,

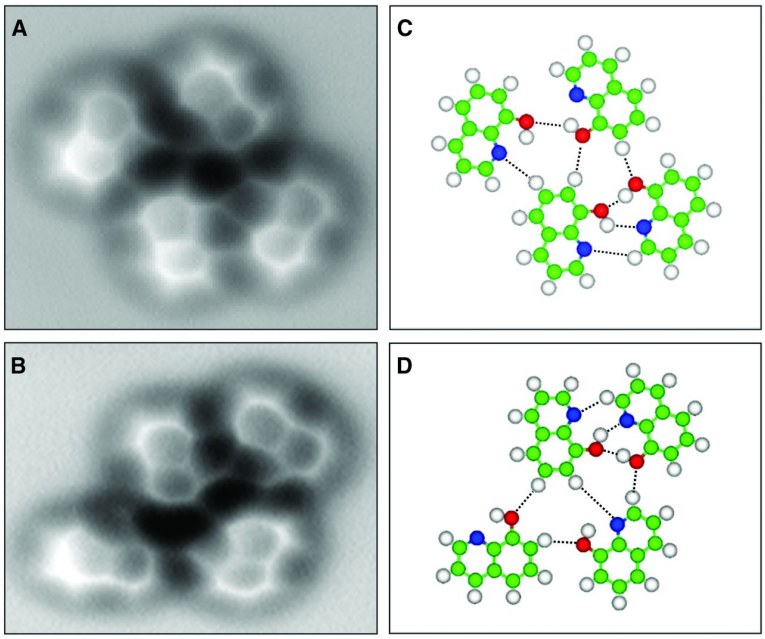

Figure 1.4: AFM measurements of 8–hq assembled clusters on Cu(111). (a and b) Δf images of H–bonded molecular assembled clusters and (c and d) their corresponding structure models. The dashed lines in (c) and (d) indicate likely H bonds between 8–hq molecules. Color code: green for carbon, blue for nitrogen, red for oxygen, and white for hydrogen. Reproduced with permission from [123].

161] has sparked a debate on the origin of the contrast. While the proposed interpretation pertaining the direct sensing of the charge distribution [123] has been supported by other works [162, 163], alternative interpretations require taking into account tip charge redistribution effects [66]. Also, it was proposed that the feature is simply an artifact of the probe finding its minimum energy configuration, regardless of the presence of an H-bond [127, 160, 164–167]. This argument was used to explain inter–molecular features observed in images of bis(para–pyridyl)acetylene (BPPA) tetrameters along non-bonded N–N atoms [127].

On–surface synthesis

The ability of the NC–AFM to identify and manipulate molecules *in situ* resulted in rapid increase of research works in the novel field of on–surface synthesis [168–170]. de Oteyza *et al.* [120] pioneered the use of the NC–AFM to investigate on–surface reactions. In their seminal work, the detail internal bond transformations of oligo-(phenylene-1,2-ethynylenes) on Ag(100) was clearly revealed by HR images as the molecules underwent thermally induced cyclization processes. Fig. 1.5 shows STM and AFM images of the three most common product molecules and the initial reactant. Although the STM unambiguously distinguishes the molecules, images (which reflect molecule's electronic LDOS) are diffused. In contrast, the NC–AFM revels the internal structure of the molecule with a sub-nanometer spatial resolution and even some information of the molecular bond conformation.

More precise mechanisms to induce the chemical reactions are now used for on–surface synthesis. For instance, force induced tautomerizations was applied to single porphycene molecules on Cu(110) surface to activate the rearrangement of H atoms via chemical bond breaking and formation [140]. Chemical reactions are also activated via the application of tip–sample voltage ramps. This was used to induce and image a reversible Bergman cyclization on the DBA molecule deposited on an insulating film.

With many successfully examples of on–surface synthesis [120, 122, 126, 131, 133–135, 138–143, 145, 147, 148, 171–175], it has become a very exciting field of research [169, 170, 176, 177]. All these works have two ingredients in common: the controlled application of the voltage ramps and tip–induced forces on precise positions defined by specific chemical elements of the molecule; and the readily available HR images that are used to identify the molecules. An accurate knowledge of the origin of the contrast and the role played by all the interactions in the AFM experiments is necessary for understanding chemical identification [178] and improving molecular elucidation [179]. HR–AFM permits discriminating molecules by finding distinctive features in the images. This has been achieved in complex organic structures [111], Asphaltenes [113], complex Halogenated Dipeptides [117], insolulabel graphene precursors [125] and on–

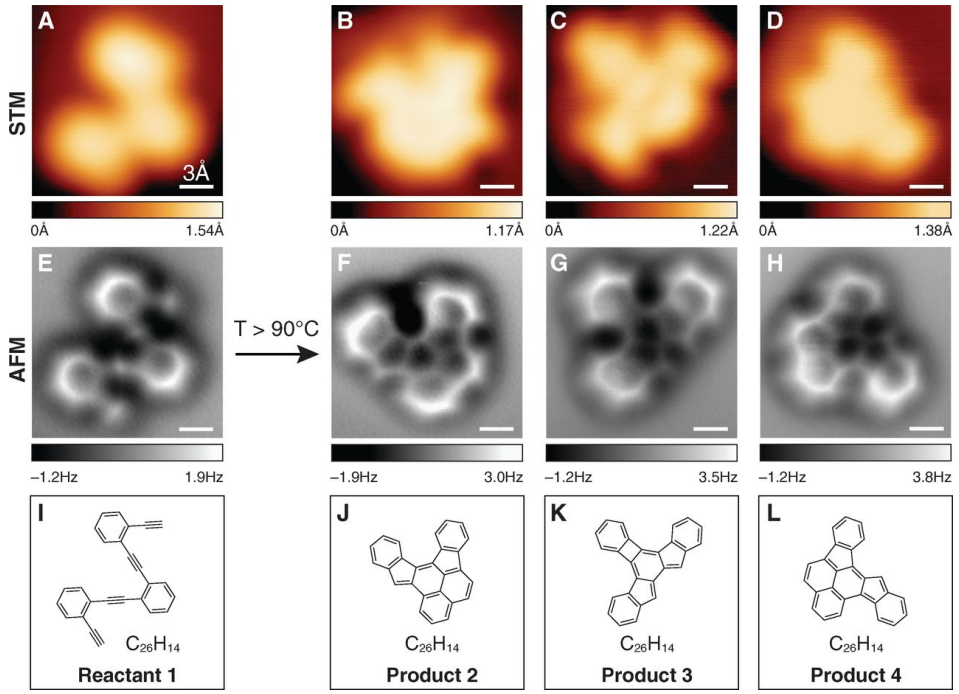

Figure 1.5: Imaging intermediate states with SPM. (a) STM image of 1,2-bis((2-ethynylphenyl)ethynyl) benzene before annealing and (b)-(d) individual products after annealing at $T > 90°C$ ($I = 10$ pA, $V = -0.2$ V, $T = 4$ K). (e)-(h) Same molecules imaged with a NC–AFM using a CO tip ($V = -0.2$ V, qPlus sensor resonance frequency 29.73 kHz, $k = 1800$ N/m, $Q = 90000$, $A = 60$ pm). (i)-(l) Schematic representation of molecules. Reproduced with permission from [120].

surface reaction intermediates and products [120, 131, 138, 141, 142, 147, 171, 180]. Indeed, early on, Guo *et al.* [181] pointed out that the CO termination is capable of achieving chemical sensitivity in molecules by examining distortions in the images. These distortions have been observed in hydrocarbon rings with heteroatoms [144, 148, 149, 171] and surface with dopants [182], but it is still unclear what causes them [61, 63, 148, 149, 167, 182–185].

1.2.3 HR–AFM simulation methods

Computational calculations have played a key role in understanding surface science phenomena and in particular, the contrast mechanisms of the AFM. A wide variety of computational tools are used for this. On one end of the spectrum, we have DFT. It is a variational procedure used to solve Schrödinger's equation where a functional of the energy is minimized with respect to the charge density. It is an accurate and versatile tool in that it can predict the most stable electronic configuration of an atomic arrangement. That is, it can create and break bonds. On the other end of the spectrum, we have Molecular Mechanics (MM) and Molecular Dynamics (MD) simulations. In these, the electronic configurations of the atoms and their interactions are incorporated through effective classical potentials. These can be parametrized from DFT calculations or experimental results. Although less accurate and versatile than DFT, the use of classical potentials make it possible to explore a wide variety of atomic configurations rapidly.

DFT calculations supplemented by vdW interaction are used to simulate force spectroscopy curves at different sites, and in limited cases, full AFM images. It has been successfully used to understand the contrast inversion in carbon structures [88, 90]. In HR–AFM imaging with CO functionalized tips, DFT has not only reproduce the qualitative (and sometimes quantitative) behavior of experimental images, but also aided in isolating the Pauli repulsion as the most crucial interaction in the contrast formation at small tip–sample distances [40, 119, 181, 186]. However, DFT methods have two shortcomings. First, they can only incorporate a limited number of atoms in the calculations; very efficient codes can treat thousands of atoms. For instance, this is too limited to simulate the large surfaces needed to describe AFM experiments in graphene moirés with macroscopic size deformations. The other limitation is the computational cost. DFT calculations require long self–consistency electronic cycles and are thus impractical for simulating full–size images on a routine basis, especially when ionic relaxation are required. Consequently, other fast, but less accurate, methods to simulate HR–AFM images within the DFT framework have been developed. For instance, the density embedding method [187] requires no

fitted parameter and, in principle, can be used for different tips in all kinds of samples. So far, the results reported offer a good description of the images, but do not deal with the probe tilting and the accuracy is improvable.

Although accurate and reliable, simulating AFM with DFT is computationally expensive, especially when including tip and sample ionic relaxation. However, if the tip–sample interaction is weak, the effect of the CO tilt can be approximated without carrying out ionic minimization by interpolating the frequency shift of the relaxed probe on a static map using the lateral force acting on the rigid CO molecule [166, 188]. Although the method gives a crude but fairly accurate picture of AFM experiments, simulated images significantly lack sharpness and furthermore bond–like features are not predicted along the PES saddle lines.

A popular method to simulate HR–AFM images with functionalized tips is achieved by using parametrized MM pair–wise potentials. The functional form of the force field is typically a Lennard–Jones (LJ) potential that includes an r^{-6} term to simulate attractive interactions, mainly vdW, and an r^{-12} term to simulate repulsive interactions, mainly Pauli repulsion [160, 189]. In addition, tip–sample interactions induced by inhomogeneous charge distributions are implicitly accounted for through the Coulombic interactions between a small point charge placed at the probe and the electrostatic potential of the sample [164]. In order to simulate the cylindrical confinement of the CO molecule onto the metallic apex, the movement of the probe is constrained by a lateral harmonic potential.

Although these MM models provide a way to simulate rapidly AFM images that account for probe tilt, the results can be misleading. First, the parameters may not be exportable from system to system. Second, the terms that describe the potentials may encompass a variety of interactions. Taking into account the widespread use of these models [127, 144, 160, 164, 189], it is imperative to address the validity of methods that use point–like tips to simulate AFM images, to understand why they work and the nature of their limitations.

An important goal in AFM theory is to create a methodology analogous to the Tersoff-Hamann (TH) approach for STM. With such a method, images

could be created from the isolated properties of the sample and possibly the tip. The closest method in HR–AFM that accomplishes this was created by Moll *et al.* [190] to simulate images captured with CO tips. It relies on the fact that at close–tip sample distances, the contrast is dominated by the Pauli repulsion. The method models this interaction with input from the charge density of the sample. Although the simulated images capture some features of the experimental images, by excluding the other interaction it forfeits quantitative accuracy. In addition, as it uses no input from the charge density of the tip, it cannot incorporate tip tilting effects.

1.3 Summary and thesis organization

In the first part of this chapter we described the experimental apparatus of the AFM with a special focus on the ingredients needed for HR: 1) FM mode, 2) LT–UHV, and 3) sharp tips. Two setups are commonly used for this; large amplitude cantilever based AFMs with metallic tips, and AFMs with small amplitude self–sensing sensors with functionalized tips. The first setup has been used extensively to characterize highly corrugated moirés. However, it is unclear if it can resolve a weak interacting graphene on metal with tiny topographic corrugations. Furthermore, the dissipation signal typically present in measurements of weakly coupled 2D systems is not well understood and complicates the interpretation of the images. The second setup, small amplitudes and close shell probes, benefits from an increase in sensitivity to the SR forces responsible for the atomic resolution. Among these probes, the CO tip benefited from a surge of success due to the stunning images of molecules reported in the literature, which resolve inter– and intra–molecular features. Although it is well known that Pauli repulsion and the CO tilt play an important role in the contrast formation, the role of other interactions, in particular the ES, is not well understood. In this regard, there is not even a consensus on the proper characterization of the CO functionalized metallic tips. There is also an open debate in the scientific community regarding the probing of H–bonds with flexible close shell tips. Notwithstanding, the success of CO tips is undisputed. It contributed to the creation a new field of research that explores molecular chemical reaction on surfaces. It heavily relies

on molecular elucidation and chemical sensitivity, goals which are not yet fully achievable with the AFM.

The thesis is organized as follows:

- In chapter 2, we study the atomic scale variations of the mechanical response of weakly coupled 2D materials probed by a cantilever based AFM. We present topography and dissipation images that resolve the atomic and moiré patterns in graphene on Pt(111), despite its extremely low geometric corrugation. The imaging mechanisms are identified with a multiscale model based on DFT calculations, where the energy cost of global and local deformations of graphene competes with SR chemical and long–range vdW interactions. The simulations show that the atomic contrast of the carbon atoms is related to the SR tip–sample interactions, while the dissipation can be understood in terms of global deformations in the weakly coupled graphene layer. Surprisingly, the observed moiré modulation is linked with the subtle variations of the local interplanar graphene-substrate interaction. We also explore the capabilities of the AFM to achieve subsurface resolution with a study of single vacancies on the Pt(111).

- Chapter 3 presents a study of the ES field of CO decorated metal tips and its relevance for HR–AFM imaging. With DFT calculations, we investigate the ES field generated by CO molecules in gas phase, as adsorbates on surfaces, and bonded to metallic tips. We postulate that CO decorated metallic tips cannot be described by single dipoles; a proper description takes into account the positive dipole behavior of the metallic apex and the negative charge cloud strongly localized in front of the oxygen atom. This description is incorporated into a model developed in the chapter to simulate rapidly interaction–decomposed AFM images with flexible close shell probes. We validate the model of the tip by reproducing experimental qPlus based images of localized ionic defects (Cl vacancies on a metal–supported NaCl bilayer). With this, we address contradictory statements in the literature about the nature and strength of the ES field of CO tips.

- In chapter 4, we focus on H–bonded layers of triazine molecules as probed

by CO tips. We describe the changes require in the methodology developed in chapter 3 (for studying surfaces) to simulate molecules. With interaction decomposed images generated by the method, we identify the interplay of the ES, SR, and vdW forces on the contrast formation and discuss the intra– and inter–molecular features commonly observed in the images. A strong cancellation between the ES and SR results in a net interaction dominated by the ES and vdW far from the molecules, and by the SR at short distance. We also demonstrate the existence of different PES minima for the CO tilt and discuss its influence on imaging.

- In chapter 5, we develop a new methodology to simulate HR–AFM images that puts on equal footing the SR and ES interaction. Whereas the previous method used pair–wise potentials to describe the SR, this one uses the overlap of the charge densities of the tip and the sample. With this, we investigate intra- and inter–molecular features observed in AFM images that are closely related to subtle effects in the charge density of the sample. First, we demonstrate that not only structural similar molecules with different stoichiometry provide qualitatively different AFM images, but that the chemical environment (i.e., bonding structure) is also relevant. Second, we pinpoint the Pauli repulsion as the underlying mechanism responsible for the discrimination of covalent bond orders with CO tips. Lastly, the probing of weak intra–molecular bonds associated with H-bonds are investigated.

- The conclusions of the work and the perspectives are presented in chapter 6.

2 Atomic–scale variations in the dissipation signal of weakly coupled 2D materials

AFM has become the tool of choice for atomic scale characterization in a wide range of surfaces. However, obtaining atomic resolution in 2D materials, such as graphene, is still challenging. This is due to the small geometric corrugation the surface adopts when deposited on the substrate. Furthermore, dissipative processes that take place when the substrate is weakly bonded to the substrate complicate the interpretation of the measurements.

In this chapter, we show that large-amplitude cantilever-based NC–AFM is capable of resolving graphene on Pt(111) in the Δf and the dissipation signal. Images show the atomic structure of the graphene network and, despite an extremely low geometric corrugation, the moiré pattern. Through first-principle calculations, we show that the atomic contrast is related to the SR tip–sample interactions [90]. We also develop a multiscale model to explain the moiré contrast and the origin of the dissipation. They are rationalized in terms of global and local deformations in the weakly coupled graphene layer. With this, we show that NC–AFM is sensitive to the local stiffness in the atomic scale limit on weakly coupled 2D materials, as graphene on metals. Furthermore, we explore the possibility of obtaining subsurface resolution that allow sensing defects underneath the graphene. The experiments presented in this chapter were performed by the group of Prof. José María Gómez-Rodríguez of Universidad Autónoma de Madrid.

2.1 Introduction

2.1.1 Atomic contrast in carbon structures

In spite of the simplicity of the atomic arrangement of the honeycomb structure of graphite, graphene, and carbon nanotubes, the contrast observed in SPM images changes depending the tip material, applied bias voltage, and the tip–sample distance range [83, 191–193].

First we focus on STM. Out of all the carbon structures, the graphite(0001) surface has been imaged the most [41, 194–201]. Graphite is formed of weakly coupled graphene layers in a Bernal stacking. Each graphene layer has two triangular sublattices with atoms forming a honeycomb arrangement. The stacking breaks the symmetry of the sublattices; with the most important consequence that, near the Fermi energy, only the atoms of one sublattice have available electronic states to tunnel current. Theory predicts that, for low bias voltages, STM images have bright spots, corresponding to topographic maxima, over atoms of one sublattice [196]. That is, for low bias voltages, STM images should have a triangular symmetry. Additionally, theory predicts that the honeycomb pattern of the atomic positions should be recovered for larger bias voltages [90]. However, experimental images of graphite and graphene bilayers have triangular symmetry [41, 77, 84, 194–197, 202, 203] or honeycomb symmetry [197–201] over a broad range of bias voltages. The lack of agreement can be explained considering two factors. On the one hand, the models assume that during the imaging, the graphene layers remain adhered. However, even in STM, the tip and the sample interact through forces. The weakly bonded graphene layers are prone to decoupling and adhering to the tip. This is evidenced by the large dissipation signal typically recorded in AFM experiments [77]. On the other hand, when the tip comes close to the sample, standard perturbation approaches [84, 196, 197] that rely solely on the charge density and the density of states of the sample [204] are incomplete. A more complete theory that maps the first-principles Hamiltonian in a local orbital basis and uses nonequilibrium Green's function formalism and includes multiple scattering effects to all orders [205] predicts an inversion of contrast at smaller tip–sample distances [90]. The implication being

that maxima in STM images observed in the experiments may not even correspond to atomic positions. This complicates the interpretation of AFM images that use the simultaneously–recorded tunneling current to identify the atomic positions [77].

Whereas the tunneling current is sensitive to subtle electronic effects, the AFM, relying on the forces between the tip and the surface, is expected to reflect the real atomic structure of the sample. However, FM–AFM experiments on carbon structures paint an even more complicated picture than STM. The first experiments on the graphite surface with atomic resolution showed maximum attractive tip–sample forces with triangular periodicity [82, 83, 87]. From simple LJ MM simulations, the bright spots in the images were interpreted as hollow sites [206]. Later, more sensitive qPlus experiments revealed the hidden atom [77, 84, 85, 207] providing images with the honeycomb symmetry of the atomic positions. Additionally, these experiments on graphite: 1) demonstrated that the contrast can vary as a function of the tip–sample distance and 2) consistently recorded a large dissipation signal. Yet, experiments on Single Wall Carbon Nanotubes (SWCNT), carbon structures that are stiffer and less prone to manifesting dissipation, again provided images with triangular symmetry [87, 191]. In contrast to the graphite experiments [77, 82–85, 87, 207] where (most likely) a metallic tip was used, the SWCNT was imaged with a semiconducting tip. The resulting forces, a factor of 10 less attractive than on graphite, are attributed to vdW interactions. Consequently, the bright spots in the images are assigned to the hollow sites [206].

Ondráček *et al.* [90] explained the rich variety of patterns observed in SPM images of carbon based nanostructures in terms of the chemical reactivity of the tip and the tip–sample distance range. With the aid of DFT calculations, the authors studied the interaction between rigid tips with different chemical reactivity and a variety of carbon nanostructure samples. Fig. 2.1 shows force curves of a SWCNT and a graphite(1000) surface as probed with different tips: a reactive W tip and an inert dimer-terminated Si tip [1]. Fig. 2.1(a-b) shows the

[1] The dimer-terminated Si tip has a very low reactivity on a graphene surface, however, when probing semiconducting surface the apex readily bonds to adatoms [208].

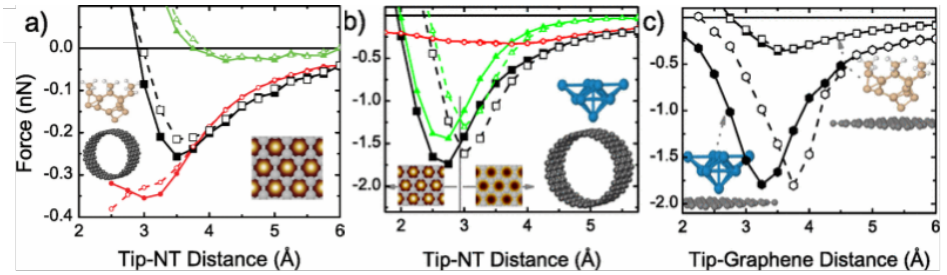

Figure 2.1: Forces on a SWCNT using (a) an inert dimer-terminated Si tip and (b) a reactive W tip. Open (solid) symbols correspond to the tip on a carbon atom (hollow site). Black lines represent the total force, red lines the vdW contribution, and green lines the non-dispersive interaction (E^{PBE}_{KS-DFT}). (c) Comparison of both tips on a graphite(0001) surface. Reactive tips change locally the hybridization and provide force maxima on the atoms. Adapted with permission from [90].

total force (black lines), the vdW contribution (red lines) and the non-dispersive (E^{PBE}_{KS-DFT}) interaction [2] (green lines) obtained with both tips on the SWCNT. Open (solid) symbols correspond to the tip on a carbon atom (hollow site). With both tips, an observable difference in the total force between the atoms and the hollow sites, or atomic contrast, is obtained below 4 Å. The contrast is dictated mainly by the E^{PBE}_{KS-DFT} contribution. The vdW interaction provides a common attractive background that modifies the absolute value of the force but does not yield by itself atomic contrast. Differences over hollow and top sites for distances smaller than the force maximum do contribute to enhance the atomic resolution, but they are a consequence of the different atomic relaxations induced by the SR interaction (repulsive part of E^{PBE}_{KS-DFT}). The non-dispersive interaction has a different nature depending on the reactivity of the tip. For the inert tip, it is essentially the Pauli repulsion between electronic clouds, and is larger on the areas of higher electron density (e.g., on top of the carbon atoms). Consequently, the dimer Si apex yields larger attractive forces on hollow sites that correspond to the bright spots in the experimental FM–AFM images [191].

[2] E^{PBE}_{KS-DFT} is the interaction as calculated from standard DFT using the PBE [209] Exchange and Correlation (XC) functional.

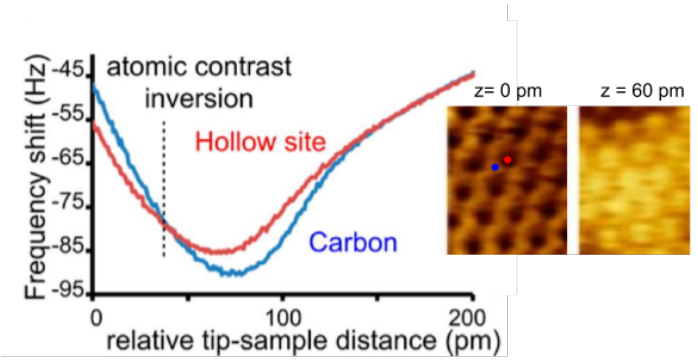

Figure 2.2: Graphene on Ir(111) as imaged with FM–AFM and a metallic tip. Frequency shift versus distance measured on the hollow site and carbon site (indicated in the inset). There is an inversion of the atomic contrast at $z \sim 4$ Å. Adapted with permission from [88].

In contrast, for $z > 3$ Å the W tip yields more attractive forces on the top sites compared to the hollow sites. This is explained by the reactivity of the W tip which makes energetically favorable a change in the hybridization, from sp^2 to sp^3, of the probed carbon atom, resulting in the formation of a chemical bond [90, 178, 208]. However, for shorter tip–sample distances, the interaction on the top site decreases due to the strong Pauli repulsion, and there is a crossing of the force curves that results in force maxima on the hollow sites. This result, which also holds for graphite and graphene (see fig. 2.1(c)), predicts a reversal of the FM–AFM image contrast for very close distances when metallic tips are used to image carbon based nanostructures samples.

Although FM–AFM images of the graphite surface showed changes in the atomic contrast as a function of the tip–sample distance [77, 85, 207], the first clear–cut images and spectrocopies of the contrast inversion were recorded on the graphene on Ir(111) [88]. Fig. 2.2 shows CH–AFM images and a force curve of epitaxial graphene on Ir(111) with a metallic tip. In the attractive regime, a triangular pattern of light spots (less attraction) is obtained. Contrary to previous interpretations [83, 87, 207], the authors attribute these positions to hollow sites. At smaller distances, in the repulsive regime, the contrast inverts. The bright spots (smaller attraction) take on the honeycomb symmetry of the

atomic positions. The Δf versus distance plot over the proposed hollow and carbon positions shows the inversion of contrast at $z \sim 40$ pm. The authors also image the sample with an inert CO-metallic tip and find no inversion of contrast. The behavior of the reactive metallic tip and inert CO tip is consistent with the explanations of Ondráček *et al.* [90].

2.1.2 Graphene on metals with AFM

Graphene is a novel material with unique electronic and mechanical properties and high nanotechnological value [210]. Due to its bidimensional nature, for most applications, it is grown or placed on a substrate, most commonly a metal. The graphene's properties can be efficiently tuned by the interaction with metals [91, 92]. The interaction strength varies widely, from the strong coupling with Rh[93, 94] and Ru [95], to the weak limit (Ir [96], Pt [97]), where graphene retains its unique electronic properties [98]. The different lattice parameters of graphene and the metal underneath are accommodated through the formation of commensurate structures known as moiré patterns, where C atoms become inequivalent due to their different bonding configuration with the metal. The resulting "true" topographic corrugation of graphene –the difference in height among the topmost and the bottom C atom– varies widely, even in the weakly interacting cases, where it ranges from ≈ 50 pm on Ir [99, 100] to practically flat (≤ 3 pm) on Pt [97, 104].

While STM can easily resolve these moiré patterns, even in the graphene on Pt case [97, 211], AFM experiments have only been reported in highly corrugated cases as Ru [102], Rh [103], and Ir [88, 104]. Focusing on the most challenging case, graphene/Ir, experiments with a Kolibri sensor using a W tip clearly resolved the moiré in CH–AFM images [104]. Measurements with a tuning fork using both inert (CO–terminated) and reactive (Ir–terminated) tips [88] were able to identify the atoms with both tips at any tip–sample distance. This atomic–scale resolution allowed them to observe an inversion from attractive to repulsive atomic contrast with decreasing tip–sample distance predicted theoretically for reactive tips [90]. Except for graphite [85, 86], atomic resolution in weakly coupled graphene based materials using cantilever AFM with large

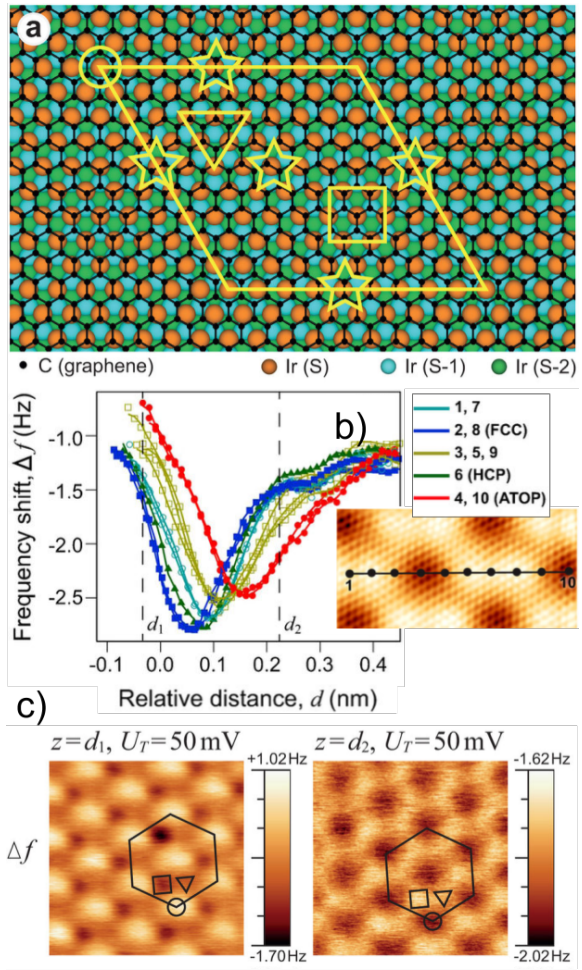

Figure 2.3: (a) Crystallographic structure of (10×10) graphene on (9×9) Ir(111). The high-symmetry places are marked by circle, rectangle, down-triangle, and stars for ATOP, FCC, HCP, and BRIDGE positions. (b) Δf as a function of the relative distance between the tip and the sample. The inset shows the corresponding STM image ($UT = +50$ mV, $IT = 400$ pA) with the path where Δf was measured. (c) CH Δf images obtained at two different heights, d_1 and d_2. Adapted with permission from [104].

oscillation amplitudes has not been reported.

In the previous section (sec. 2.1.1), experiments on the graphene/Ir(111)

were used to discuss the contrast inversion of the atomic array of the graphene network. Actually, this system forms a highly corrugated moiré. In addition to the atomic resolution, the full size CH–AFM images [88] have a superstructure with the periodicity of the moiré and with a contrast that inverts. The origin of this moiré and its contrast inversion was explored by Voloshina *et al.* [104]. The unit cell of graphene on Ir(111) is shown in fig. 2.3(a) with the corresponding high–symmetry local arrangements of carbon atoms above Ir layers marked in the fig.: ATOP (circles), FCC (squares), HCP (down-triangles), and BRIDGE (stars). Experimental Δf versus distance curves on the ATOP (highest) and FCC (lowest) areas (Fig. 2.3b)) have minima that differ by $\sim$20% and are displaced by $\sim$1 Å. DFT calculations with a 5-atom W tip, that do not include any atomic relaxations, provide very similar interaction energy curves that are only shifted by 0.40 Å. Based on this comparison, the CH–AFM contrast (see fig. 2.3(c)) was attributed to differences in height and interaction strength (not captured by the simulations) for those areas [104].

AFM can also be used to measure the elastic properties of the graphene on metals. One of the most important features of graphene monolayers is their exceptional mechanical strength. With a high Young's modulus of the order of 1 TPa [212], as reported in flakes of tens to hundreds of micrometers, it is considered one of the strongest materials ever measured. However, for nanotechnological applications, it is important to measure the mechanical response down to the nano– and atomic scale. Koch *et al.* [171] reported nanoscale measurements of the elastic response of graphene nanodomes in the graphene/Ru(0001) system. When grown on Ru(0001), graphene spontaneously forms a honeycomb lattice of 3 nm periodicity with domes that have 0.075 nm of height [213]. The nanomechanical properties of the graphene are quantified by indenting an AFM tip periodically on the different parts of the domes. The structure, which responds reversibly, can hold relative normal displacements up to 0.12 nm with response frequencies in the terahertz range [171].

2.1.3 Graphene/Pt moirés

Within the family of graphene on metals, Pt is considered as a model for low–interacting systems. The first STM work on the system observed a superstructure on top of the expected honeycomb lattice [214]. Later, STM experiments [101, 211] identified a variety of moiré patterns. These are formed due to the mismatch of the graphene lattice (2.46 Å) and the Pt(111) lattice (2.78 Å) and depend on the relative rotation of the two lattices. In principle, an infinite number of moirés can be obtained, however, those that minimize the deformation of the graphene network are favored [215]. Within the moiré cell, each carbon atom has a different chemical environment that depends on the position with respect to the substrate atoms. This dictates the graphene–metal interaction and thus, the height of each carbon atom in the cell. As a general rule–of–thumb, the greater the interaction of the carbon atom and the substrate, the closer it binds to it.

The 3×3 is the most commonly observed moiré in the graphene/Pt(111) surface [97]. It is a relatively flat moiré (≤ 3 pm) formed by a 19.1°rotation of the graphene lattice with respect to the Pt lattice, corresponding to a lattice misfit of 0.60% [101]. Ugeda *et al.* [97] imaged with STM a large area of an atomically perfect graphene on Pt(111) surface and identified two moiré structures: on the top left corner of fig. 2.4(a) the $(\sqrt{21} \times \sqrt{21})$R11°and on the bottom right corner the (3×3)R19.1°. dI/dV spectra measured in the pristine graphene surface showed a clear dip at $\sim +300$ mV accompanied by a V shaped rise at both sides (see fig. 2.4(c)). This is consistent with DFT theory [97, 216] and photoemission experiments [217], and suggest that the dip is associated with the position of the Dirac point in the graphene/Pt(111) surface. The implication being, that, when grown on Pt(111), graphene retains its unique electronic properties, less a slight doping that shifts the Fermi energy. STM simulations with nonequilibrium Green's function formalism to evaluate the current [218] explain the moiré in terms of purely electronic effects [97]. The simulated images are anticorrelated with respect to topograpic corrugation. In other words, the brightest features in the calculated image correspond to C atoms that are lowest in the graphene sheet.

2.1.4 Overview

For the AFM, the graphene/Pt system poses an insurmountable challenge. First, according to the analysis of the graphene/Ir (sec. 2.1.2), in the absence of a large topographic corrugation, the quasi–flat graphene/Pt(111) moiré should not be detectable with AFM. In the absence of a large topographic corrugation, we have to resort to subtle differences in the electronic and mechanical properties of the individual carbon atoms induced by the different interaction with the metal substrate. Although STM on graphene/Pt(111) has resolved several moiré patterns [211], the large apparent corrugation arises from a purely electronic effect [97]. On the mechanical side, AFM has been extensively used to explore the local mechanical properties of materials [105, 106], but with lateral resolutions up to the nanometer scale [102, 107]. Second, as discussed in sec 2.1.1, weakly bonded layers materials are prone to AFM dispersive processes that complicate the interpretation of the experiments.

In this chapter, we address these problems with a combined experimental and theoretical NC–AFM study of the contrast formation of graphene on Pt(111) moirés. The chapter is structured as follows. In sec. 2.2 the experimental methods used to grow and image the graphene/Pt moiré and the details of the DFT calculations used throughout the chapter are described. In sec. 2.3 the experimental results are presented: topographic and dissipation images, and Δf and dissipation spectroscopies of the graphene/Pt(111) 3×3 moiré. In sec. 2.4, the atomic contrast is explained in the attractive and repulsive regime with first principle calculations. In sec. 2.5 we develop a multiscale model, fitted from DFT calculations, to explain the moiré contrast as well as the role of the dissipation in the imaging mechanism of the AFM in weakly bonded 2D surface. Finally, in sec. 2.6 we explore the capabilities that the AFM has to achieve subsurface resolution by studying single defects in the Pt substrate.

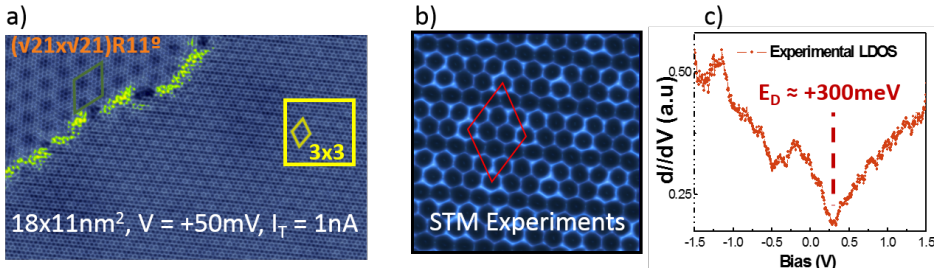

Figure 2.4: (a) STM image of the pristine graphene/Pt(111) surface showing two different moiré structures. (b) Zoom of the 3×3 region highlighted in (a). Sample bias: 50 mV, tunneling current: 1.0 nA for (a) and (b). (c) Scanning Tunneling Spectroscopy (STS) measurement of the local density of states of pristine graphene on Pt(111). Adapted with permission from [97].

2.2 Methods

2.2.1 Experiments

The experiments carried out by our collaborators were performed with a home-made ultra-high vacuum cantilever based NC–AFM operated at 5 K. In this setup, optical interferometry is used to detect the dynamics of the cantilever. The AFM was operated using the FM method, where the shift of the cantilever free resonance frequency is measured, while keeping constant the oscillation amplitude. Large oscillation amplitudes (10–20 nm) were required to maintain the stability of the cantilever during the measurements. A sample voltage (V_{bias}) was established to minimize the long–range electrostatic force at the beginning of the acquisition. The microscope was controlled by a DULCINEA SPM controller (Nanotec electronica S.L.) in combination with the easy PLL plus controller (Nanosurf). Simultaneous images and 2D mapping were performed using the WS×M software [219]. Simultaneous images, using the second pass method, were performed by acquiring the fast scan direction in topography images twice at two different set point before moving the tip in the slow scan direction. The 2D mapping was recorded along 128 points on the graphene surface. During the acquisition, the tip is required to move parallel to the surface

without topographic feedback. After a forward movement, the tip is displaced in z–direction an amount of 1 nm/128 points = 7.8 pm up to a distance of 1 nm. Each 2D mapping takes about 4 minutes so thermal drift has no impact in the data (typical drift $\sim$ 0.03 nm/h). All the data was analyzed using the WS$\times$M software [219].

Epitaxial graphene on Pt(111) was grown from ethylene Chemical Vapor Deposition (CVD) in UHV. The Pt(111) surface was cleaned by several cycles of argon ion sputtering at 1 keV and annealing at 900 K followed by a flash heating up to 1300 K in oxygen pressure (2×10^{-7} Torr). After obtaining a clean Pt(111) surface, graphene was grown *in situ* by ethylene decomposition (P = 3×10^{-7} Torr; 60 s) while keeping the surface at $\sim$ 1300 K. With this procedure, very large graphene regions on Pt(111) can be grown [220]. Commercial platinum-iridium covered silicon cantilevers (NCLPt Nanosensors; resonance frequency $\sim$ 160 KHz, k $\sim$ 30 N/m) were cleaned of impurities in UHV by Ar+ ion sputtering (0.6 keV). The spring constant k is calculated from the geometrical dimensions of the cantilever and its eigenfrequency [221].

2.2.2 DFT details

The investigation of the 3×3 graphene/Pt(111) moiré was performed with the DFT code Open source package for Material eXplorer (OpenMX) [222], that is formulated on a localized orbital basis. Standard GGA–PBE [209] XC functional supplemented DFT–D3 [223] vdW corrections was used. The routine that calculates these corrections on the energy and the forces was coded into OpenMX as part of the work of this thesis. A double-zeta polarized (DZP) basis set was used for all atoms. A 7 au cut–off radius was used for both the C atoms and the Pt on the substrate and 9 au for the Pt on the tip. The k-sampling of the Brillouin zone was discretized with $3 \times 3 \times 1$ grids. A dense real space grid $E_{grid} = 200 \times 200 \times 300$ Ry and a stringent electronic convergence criterium ($E^{SCF} = 10^{-6}$ Ha) were used. The calculations included geometry relaxation of all the atoms of the system apart from the top layer of the tip and the bottom layer of the Pt slab. Atomic relaxations were stopped when forces on individual atoms were smaller than $F_{max} = 10^{-2}$ eV/Å. With this choice of basis set and

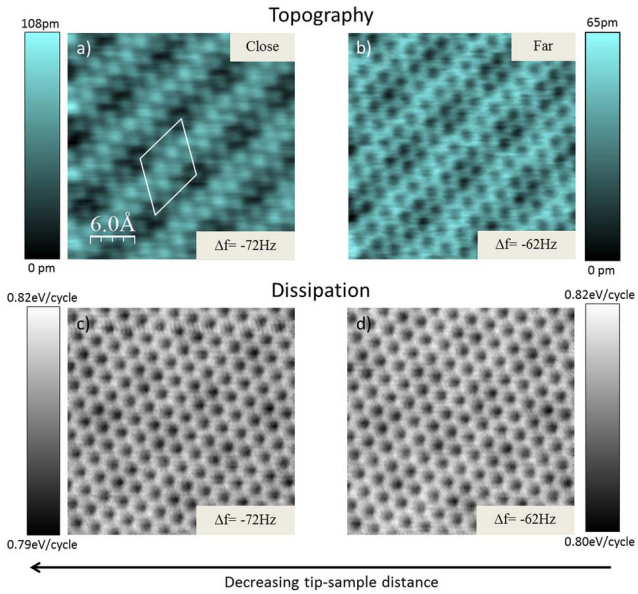

Figure 2.5: 3×3 nm^2 NC–AFM simultaneously acquired images on graphene/Pt(111). (a) and (b) show topography images at $\Delta f = -72$ Hz and $\Delta f = -62$ Hz. The 3×3 moiré pattern is marked in (a). The corresponding dissipation images are shown in (c) and (d). Parameters: $A = 20$ nm; $V_{bias} = 0$ V. All data were acquired with WS×M [219].

accuracy parameters, the graphene's lattice constant that minimizes the energy is 2.475 Å. All calculations retain graphene's DFT lattice constant, and, in order to commensurate the graphene and Pt lattices, a 0.7% strain was applied to the Pt substrate. In order to avoid interaction between image tips, a large supercell of 6×6 graphene/Pt with 4 layers of Pt atoms for a total of 194 atoms was used. This corresponds to a (14.85 Å, 14.85 Å, 30 Å) supercell. As for the AFM tip, in the main calculations we use a 10 atom pyramid Pt tip cluster cut from a Pt(111) slab.

2.3 Experimental results

Fig. 2.5 shows typical images measured on graphene/Pt(111) with a home–made UHV FM–AFM operated at 5 K with PtIr coated Si tip cantilevers using

large oscillation amplitudes. They are measured at two distinct Δf on the same region by using the second-pass method (see sec. 2.2.1). Both images display not only atomic resolution but also a periodic modulation corresponding to a 3×3 moiré. The atomic scale features have a honeycomb appearance at low Δf (fig. 2.5(b) or a simple triangular lattice, with bright protrusions corresponding to the center of the hexagons, at high Δf (fig. 2.5(a)). The low/high Δf corresponds to a cantilever oscillating far/close from the surface. This atomic contrast behavior on graphene could be expected for metallic reactive tips [90]. Strikingly, in both cases, the images show the 3×3 moiré induced by the Pt(111) substrate. Atomic-scale features and moiré patterns have already been reported in the more corrugated graphene/Ir(111) [88]. However, in graphene/Pt(111), the graphene–metal interaction is so low that this height variation is ≤ 3 pm [97] but our images show that the AFM is still able to display the moiré. The dissipation signal [79] was measured simultaneously to the topography (fig. 2.5(c-d)). Physically, dissipation indicates a hysteresis in the approach/retraction tip-path due to non-conservative tip–sample interactions [70, 71]. Although both dissipation images show atomic–scale features, no changes upon tip approach are observed.

Using 2D mapping measurements (fig. 2.6) the tip–sample interaction was fully characterized. In the 2D mapping, the Δf (fig. 2.6(b)) and dissipation signal (fig. 2.6(c)) along a selected line (dashed yellow in fig. 2.6(a)) are measured at different tip–sample distances. The Δf and dissipation versus distance on a topography maximum (red plot) and on a minimum (blue plot) are plotted in fig. 2.6(b-c). For large tip–sample distances ($Z > 0.55$ nm) there is no apparent difference between red and blue plots either in Δf curves (no contrast in topographic images) or in the dissipation. Getting closer to the surface, at $Z = 0.55$ nm, the dissipation energy increases abruptly up to a plateau ≈ 0.8 eV/cycle. At this point, atomic features with honeycomb symmetry can be distinguished both in Δf and dissipation images. As the tip–sample distance decreases, the relative corrugation of the dissipation between the hollow and top position stabilizes at less than 0.05 eV/cycle. In contrast, Δf slowly inverts its trend. When $Z = 0.20$ nm, Δf over the hollow position becomes

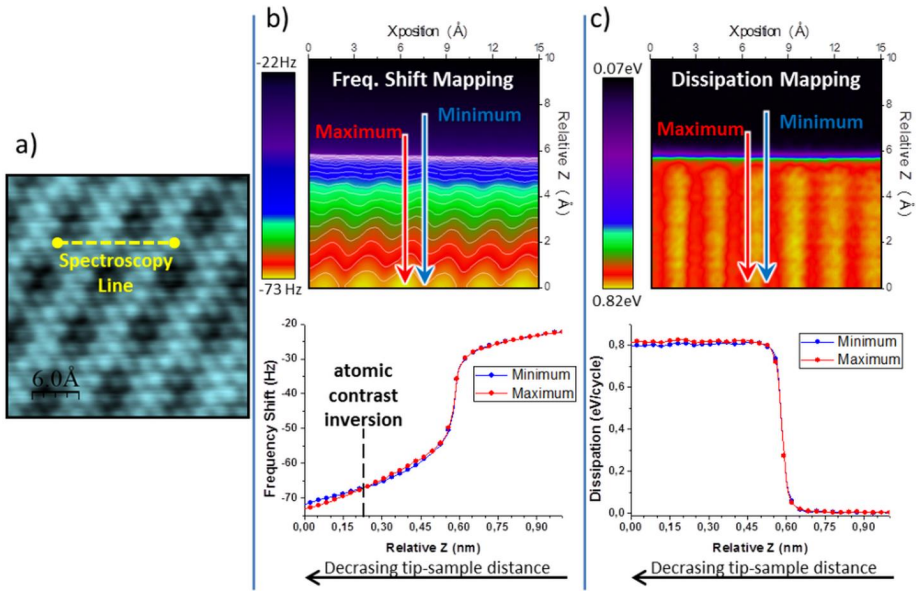

Figure 2.6: (a) 3×3 nm^2 topographic image acquired at $\Delta f = -73$ Hz, $A = 20$ nm, $V_{bias} = 0$ V. 2D plots of (b) Δf and (c) energy dissipation, measured along the mapping line while varying the tip–sample distance are displayed. Maximum (red) and minimum (blue) in the 2D mapping correspond to maximum and minimum in the topographic image.

more negative resulting in atomic features with triangular symmetry. In order to assess the negligible influence of instrumental artifacts due to transfer function effects [224], the dissipation measurements were successfully reproduced using several cantilevers and tips.

2.4 Atomic contrast first principle calculations

We have used DFT calculations to try to rationalize the experiments disscussed above. Fig. 2.7(a) shows the relaxed 6×6 graphene cell (14.85 Å, 14.85 Å, 30 Å) used in the calculations with a color scale that indicates the relative heights of the C atoms. The graphene layer adheres at 3.35 Å on top of the Pt substrate and remains very flat: the difference in height between the highest C atom and the lowest is ~ 2.5 pm.

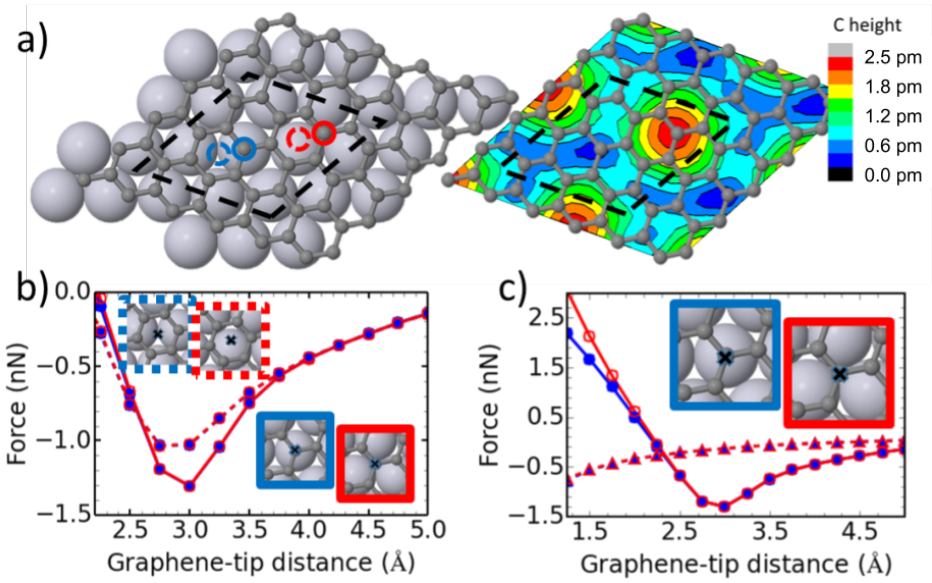

Figure 2.7: (a) DFT relaxed graphene/Pt(111) structure, highlighting the low and high moiré areas and the small corrugation. (b) Force versus distance curves in the attractive regime for the four sites marked in (a): top–low (solid blue), top–high (solid red), hollow–low (dashed blue) and hollow–high (dashed red). The plot shows atomic contrast on graphene and contrast inversion. (c) Different repulsive forces between the top–low and top–high sites for $z_t < 2.25$ Å explain the moiré contrast. Calculations on the bare Pt(111) surface for these sites (dashed lines and triangles) do not show any force difference.

2.4.1 Attractive regime

Force versus tip–graphene distance (z_t)[3] curves calculated with a 10 atom Pt tip and including tip and sample relaxations (see sec. 2.2.2 for details) are shown in fig. 2.7(b). Forces on top of C atoms (top sites) and on the center of the hexagons (hollow sites) are indistinguishable for $z_t > 3.75$ Å. Below this distance, atomic contrast is obtained and two contrast regimes can be appreciated. First,

[3] z_t is defined as the distance between the fixed layers in the tip and sample, so it is directly comparable to the piezo displacement measured in the experiments. An appropriate constant has been subtracted, so it corresponds to the distance between the tip apex atom and the graphene layer at large distances where no relaxations take place.

the forces on top sites are more attractive than on hollow sites and, at 2.6 Å, a change of contrast results in hollow sites being more attractive. As previously explained, for metallic tips, the top/hollow contrast and the inversion of atomic contrast may be rationalized in terms of the electronic density dependence of the Pauli repulsion [90]. Contrast on the moiré superstructure should yield differences on the forces between top sites. However, for $z_t > 2.25$ Å, the force versus distance curves of all top sites are indistinguishable (fig. 2.7(b)). For instance, force calculations done on the topographic lowest and highest top sites fall on top of each other.

Although DFT predicts top/hollow atomic–scale contrast of the graphene layer in the attractive regime, it predicts neither the moiré contrast nor the dissipation experimentally observed. In AFM measurements, the dissipation is produced by hysteresis in the indentation/retraction forces sensed by the tip during the oscillation path. As can be seen in fig. 2.8, indentation and retraction forces on the top site are identical and no appreciable hysteresis is observed. In this simulation, the tip is initially 5.25 Å away from the graphene layer. As the tip descended in steps of 0.25 Å of length, the bottom two layers of the tip, all the C atoms of the graphene and the top two layers of the Pt substrate were allowed to relax. The retraction curve was calculated by placing the tip at 1.25 Å above the graphene sheet, using the relaxed positions obtained from the indentation at this distance.

2.4.2 Repulsive regime

Although in the attractive regime, DFT calculations do not exhibit moiré contrast, this changes in the repulsive regime where the atomic contrast is dominated by the Pauli repulsion. For $z_t \leq 2.25$ Å the contrast between equivalent sites in the low and high areas of the moiré can be appreciated. For example, fig. 2.7(c) shows contrast between top sites (solid lines) in the low (blue) and high (red) parts of the moiré.

When removing the graphene layer and repeating the calculations only with the Pt substrate, the difference between different sites of the moiré disappears. For example, force curves on the equivalent top-high site (dashed red line) and

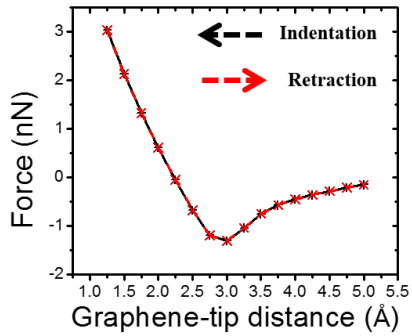

Figure 2.8: DFT tip–sample force curves on a top site of a 6×6 graphene sheet on 4 layers of Pt(111) substrate using a 10 atom Pt tip cluster. The black curve shows the indention forces (calculated during the approach path of the tip) and the red curve the retraction forces (calculated during the retraction path of the tip). The trajectory described by the curves does not show hysteresis.

the top-low site (dashed blue line) are identical (fig. 2.7(c)). This shows that the moiré contrast is not due to the direct tip–Pt substrate interaction but to the effect that the substrate has on graphene when indenting the tip. This view is also supported by calculations in which the C atoms are kept fixed: these yield no contrast between force curves of different top (or hollow) sites of the moiré.

When examining the ionic relaxation it is apparent that (in this regime) upon tip approach, the distance between the outermost apex atom of the tip and the graphene is only slightly varying. However, the local graphene–Pt substrate distance changes. The deformation of the graphene induced by the tip is so large, that the displaced C atoms are able to sense the Pt substrate: a Pt top site on the topographic low area of the moiré, and a Pt hollow on the high area. This interaction changes the local stiffness of the C atoms that now depends on its location with respect to the Pt substrate. The ionic relaxations obtained through DFT show that in the repulsive interaction regime the tip apex–graphene separation varies little. While the tip–sample distance is reduced, the graphene layer is locally deformed acting itself as a tip that allows sensing of the Pt surface.

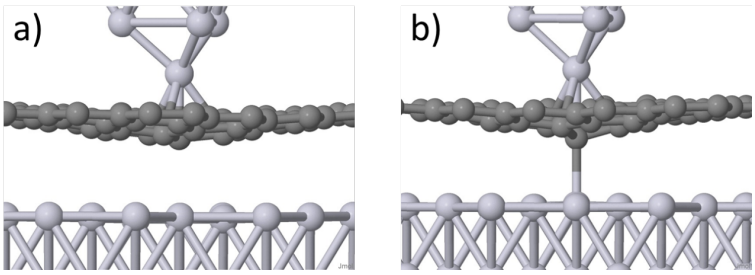

Figure 2.9: Relaxed atomic positions with the tip located at 1 Å above the graphene sheet. The tip is directly positioned on (a) a top–high site and (b) a top–low site of the 6×6 graphene/Pt moiré.

Thus, in this regime, the moiré modulation in the graphene layer is a result of the atomic–scale graphene–Pt interaction.

This can be clearly observed in fig. 2.9 where the relaxed structure of a Pt_{10} tip indenting onto the graphene/Pt(111) surface is shown. Fig. 2.9(a) shows the tip on a top–high site of the moiré pattern while fig. 2.9(b) shows the tip is on a top–low site. The high/low area of the moiré is determined by the graphene environment with respect to the Pt substrate: the high area corresponds to a C atom whose closest environment has a hollow site of Pt(111) directly below, while the low area corresponds to a C atom with a Pt atom directly underneath. These differences are sensed by the tip while in the repulsive regime, and yield the moiré pattern contrast. Consequently, this shows the possibility of obtaining atomic subsurface resolution on graphene on weakly coupled substrates with the AFM – this is explored more in depth in sec. 2.6.

2.5 Multiscale model for non-local atomic scale deformations

2.5.1 Defining the model

The DFT calculations explain the atomic contrast, its inversion, and the moiré contrast in the repulsive regime. However, they fail to reproduce the moiré contrast in the attractive regime and the dissipation in the experiments. It has been proposed that SPM tips are capable of detaching layered materials as

graphite [77, 85, 225]. This tip–induced detachment could explain the dissipation signal observed in the experiments: During tip approach, the graphene is attached to the substrate, but, upon tip retraction, the sheet locally adheres to the tip temporally, inducing a large–scale deformation of the surface. This cannot be described with the limited size of DFT simulation cells which prevent to include the effect of: a) a large graphene area, and b) a macroscopic tip. The large attractive vdW background induced by a macroscopic tip adds to the SR tip and graphene binding and promotes global deformations on an area larger than few nanometers (we use *global* for large macroscopic areas while *local* refers to the local effective area used in the DFT simulations).

In order to address these shortcomings, we have created a multiscale model, characterized through DFT calculations, that simulates the tip approach–retraction route taking into account both global and local deformations. It includes effective potentials for the interaction of graphene with the nanoscopic tip cluster, the macroscopic tip, and the Pt substrate, as well as the elastic response of the graphene sheet due to out-of-plane deformations (see fig. 2.10). The potential has the form

$$\begin{aligned} &V(z_{global}, z_{local}, z_t) = \\ &V_{t-G}(z_t - z_{local}) + A_1 V_{T-G}(z_T - z_{global}) + A_1 V^{global}_{Pt-G}(z_{global} - z_{Pt}) \\ &+V^{local}_{Pt-G}(z_{local}) + V_{BR}(z_{local} - z_{global}) + A_2 V_{E2D}(z_{global}), \end{aligned} \tag{2.1}$$

where z_{local} is the z-coordinate of the graphene area just under the tip and z_{global} is the mean z–coordinate of the globally deformed graphene flake, then $z_{local} - z_{global}$ measures the local deformation. As before, z_t is the separation between the nanoscopic tip and the graphene sheet. z_T is the macroscopic tip–graphene separation (with $z_t + z_T = \text{const.}$), and z_{Pt} the position of the Pt surface. All distances are measured with respect to the graphene's equilibrium position without the tip (see fig. 2.10). V_{t-G} describes the interaction of the nanoscopic apex with the graphene and includes both vdW and SR chemical interactions. V_{T-G} and V^{global}_{Pt-G} approximate the mean interaction between the deformed global area of the sheet and the macroscopic part of the tip and the Pt substrate respectively; they include both dispersion and chemical interactions.

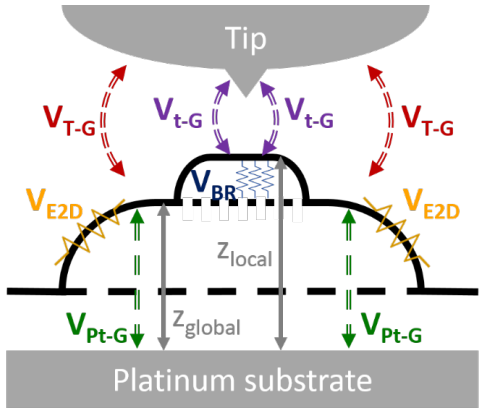

Figure 2.10: A scheme of the theoretical model which includes: a macroscopic and nanoscopic Pt tip, the graphene surface divided into a local and global area, and the Pt substrate. The potential depends on the position of the tip and the global and local deformations of the graphene.

V_{Pt-G}^{local}, effectively takes into account the interaction of the local area of graphene with the Pt substrate, i.e. it incorporates in the model the atomic scale variations of the graphene–Pt interaction. V_{BR} and V_{E2D} describe the energetic response of graphene flake to out–of–plane deformations [212]. Finally, we note that V_{T-G}, V_{Pt-G}^{global} and V_{E2D} interactions depend on the spatial area of the global deformation. We consider this effect through parameters A_1 and A_2 chosen to reproduce the dissipation energy plateau measured in the experiments: $A_1 = 0.68$, $A_2 = 0.09$. These parameters as well as the energies calculated with DFT used for the fittings are referred to the 6×6 graphene cell. The parameterization of the interaction terms are described below.

2.5.2 Parametrization of interactions

Nanoscopic tip–graphene interaction V_{t-G}

This term describes the nanoscopic Pt tip–graphene flake interaction. It was fitted from simulations of a Pt_{10} on a 6×6 graphene flake with all atomic positions fixed. Fig. 2.11 shows the energy as a function of the distance between the graphene and the tip apex for two sites: a top site

and a hollow site. The fitting was done using a Morse potential and an integrated (over one plane) vdW term,

$$V_{t-G} = V_0 \left((1 - \exp -k(r - r_c))^2 - 1 \right) - \frac{C}{r^4},$$

with $V_0 = 0.25$ meV, $k = 2.31$ Å^{-1}, $r_c = 3.82$ Å, $C = 7.37$ eVÅ^4 for the top site and $V_0 = 6.82$ meV, $k = 1.57$ Å^{-1}, $r_c = 3.59$ Å, $C = 7.26$ eVÅ^4 for the hollow site.

Macroscopic tip–graphene interaction V_{T-G}

This term describes the interaction between the macroscopic tip and the graphene sheet. The typical radius of the Pt coated Si tips used in the experiments is 200 nm. For the interaction of this macroscopic part with the graphene layer, for all practical purposes, we can approximate $R_{tip} \to \infty$. Thus, we simulate the macroscopic tip–graphene interaction as the one originated between a 6×6 graphene sheet and a 4 layer Pt(111) slab. Although the main contribution is due to vdW interaction, at short tip–sample distances, a repulsive term in needed in order to describe Pauli interaction. Fig. 2.11(b) shows the plot of the energy as a function of the tip–graphene positions along with the fitting. We fit the data using an integrated (over both planes) vdW term and a Morse potential,

$$V_{T-G} = V_0 \left((1 - \exp -k(r - r_c))^2 - 1 \right) - \frac{C}{r^2},$$

with $V_0 = 1.44$ meV, $k = 1.06$ Å^{-1}, $r_c = 3.39$ Å, $C = 3.83$ eVÅ^2.

Global Pt substrate–graphene interaction V_{Pt-G}^{global}

This term describes the interaction between the Pt substrate and the global graphene area. The same DFT simulation and fitting as in V_{T-G} is used.

Local Pt substrate–graphene interaction V_{Pt-G}^{local}

In order to examine the difference in force between different sites of the moiré using the multiscale model, we need an extra term to the graphene–substrate interaction which takes into account the mechanical energy difference due to out–of–plane deformations of the graphene layer from two

different areas of the moiré: a high–top site and a low–top site. We calculate the difference in energy through DFT by displacing a single atom of a 6×6 graphene flake on 4 layer Pt(111) substrate and allowing all the atoms of the graphene to relax. The difference in energy shows a linear response with respect to the displacement. However, due to the limited size of the layer used in the simulation, after 2 Å of displacement, the whole sheet starts to separate from the substrate. In order to erase this artifact form the fitting, we saturate the response at this height. Fig. 2.11(c) shows the elastic energy difference due to out-of-plane deformations between the two sites of the moiré. The plot also shows the fitting which was done using

$$V_{G-Pt}^{local} = E^{low} - E^{high} = E_0 \left(\frac{1}{e^{-z-z_0}+1} - \frac{1}{2} \right),$$

with $E_0 = 0.24$ eV and $z_0 = 3.35$ Å. The interaction is referenced with respect to the high part of the moiré, thus the term is only included on the low part of the moiré.

Elastic response of graphene to out–of–plane deformations $V_{BR} + V_{E2D}$

These terms describe the mechanical response of the graphene sheet to out–of–plane elastic deformations. Since pristine graphene is a 2D membrane, the energy versus deflection has a quadratic term due to the pretension or bending rigidity V_{BR} and a quartic term due to the two–dimensional Young's Modulus V_{E2D} [212]. These two terms were fitted from a simulation of a 6×6 graphene flake in which a single C atom was displaced vertically and all atoms of the layer except the corner atoms were allowed to relax. Fig. 2.11(d) shows the plot of the energy as a function of the displaced atom position along with the fitting. The fitting contains

$$V_{BR} + V_{E2D} = \frac{G_0}{2}\delta^2 + \kappa\delta^4,$$

with $G_0 = 1.13$ eVÅ^{-2} and $\kappa = 0.053$ eVÅ^{-4}.

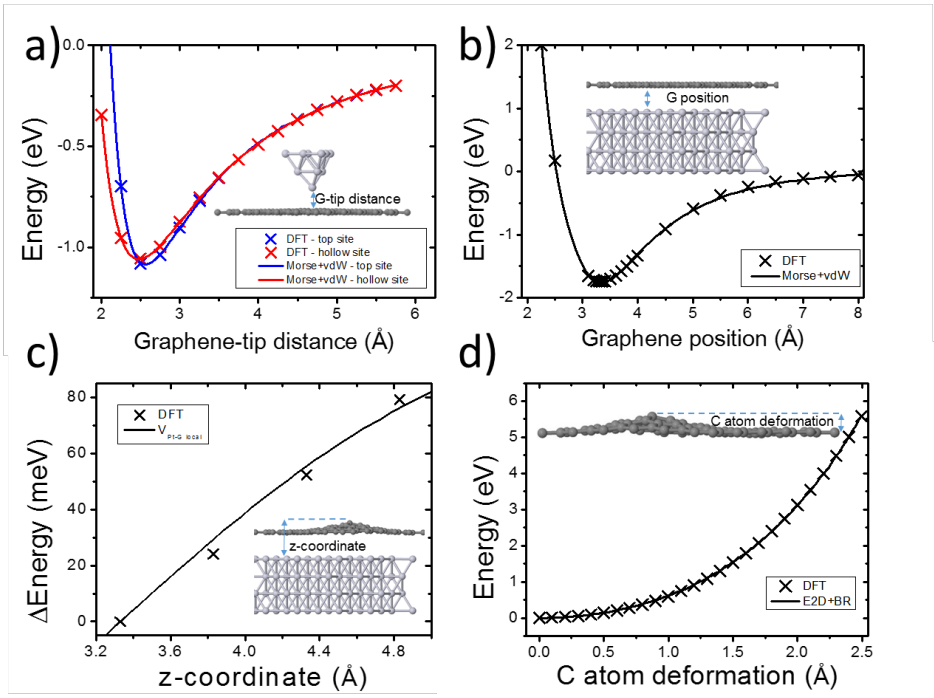

Figure 2.11: Fittings for the model. (a) The nanoscopic–graphene interaction V_{t-G}, (b) the macroscopic tip–graphene V_{T-G} and Pt substrate–graphene V_{Pt-G}^{global} interaction, (c) the Pt–graphene interaction difference (V_{Pt-G}^{local}) between the high–top and low–top sites and d) the elastic response of the flake to out–of–plane deformations $V_{BR} + V_{E2D}$. Crosses are the DFT results and lines the fitted contributions of the multiscale model.

2.5.3 Potential energy landscape

Fig. 2.12(a) shows the full potential of the model with respect to the global and local deformations of the graphene sheet and for different z_t. When the tip is far, the system has only one minimum corresponding to the the graphene being adsorbed on top of the Pt in its equilibrium position. As the tip approaches, both the local and global deformations slightly increase. At $z_t \approx 5.5$ Å, a new local minimum appears at $z_{global} \approx 2.5$ Å away from the equilibrium position. As the distance is further reduced, the two minima start to converge towards each other. At $z_t \approx 3.5$ Å, the second minimum becomes the global minimum

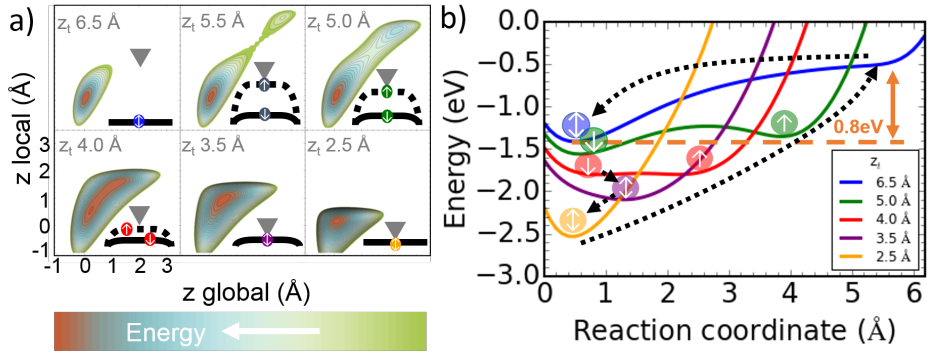

Figure 2.12: (a) 2D minimization of the eq. 2.1 potential with respect to the local and global deformation, and (b) energy profile versus the reaction coordinate, $RC = \left(z_{local}^2 + z_{global}^2(V_{min})\right)^{-1/2}$. Distances are referenced to the equilibrium position of the graphene on Pt. The reaction coordinate is calculated by minimizing eq. 2.1 along z_{local}.

but quickly merges with the first one. The potential profile is summarized in fig. 2.12(b) where the energy versus the reaction coordinate is plotted.

The approach–retract procedure presents two types of cycles depending on whether the retraction occurs before or after the energy barrier between the two energy minima disappears at $z_t = 3.5$ Å. In both cases, as the tip approaches, the system follows the first solution (left minimum in fig. 2.12(b)). If the tip retracts before the barrier, it returns through the first minimum. However, if it retracts after the barrier, the graphene sheet adheres to the tip, and the system jumps to the second minimum (right minimum in fig. 2.12(b)) and retracts through this minimum until $z_t = 5.5$ Å, where graphene disadheres from the tip, and the system jumps back to the first minimum. The difference in energy between the two solutions is 0.8 eV which corresponds to the dissipation plateau, i.e. 0.8 eV/cycle, observed in the experiments.

2.5.4 Non-Local Atomic Scale Deformations: Dominant contributions

In order to clarify the dominant contributions that stabilize the energy minima, we plot in fig. 2.13 the contributions to the energy along the reaction coordinate

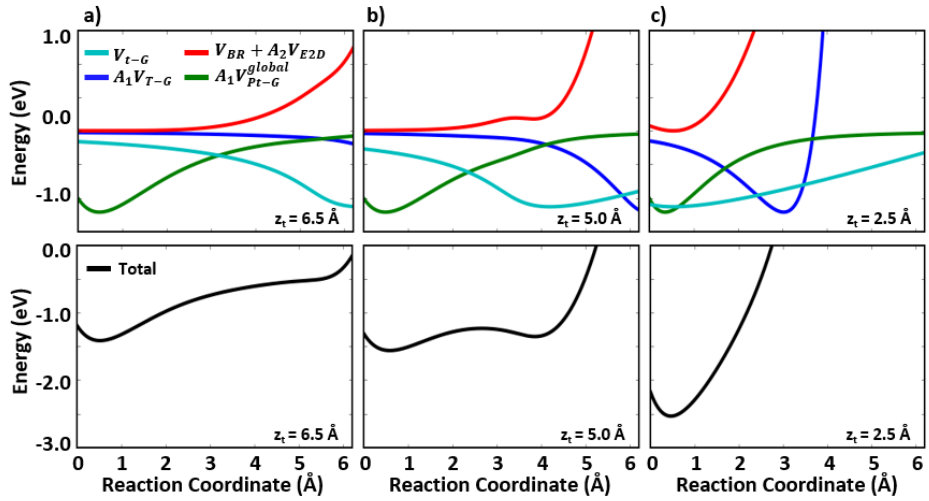

Figure 2.13: Decomposed (upper row) and total (bottom row) energy as a function of the reaction coordinates for tip–graphene distance (z_t) (a) 6.5 Å, (b) 5.0 Å, and (c) 2.5 Å.

for tip–graphene separations (z_t) (a) 6.5 Å, (b) 5.0 Å, and (c) 2.5 Å. The reaction coordinate is calculated by minimizing the total potential along z_{local}: $RC = \left(z_{local}^2 + z_{global}^2(V_{min})\right)^{-1/2}$. At large z_t (fig. 2.13(a)) the system presents one minimum. It comes from the graphene–Pt interaction, which is responsible for binding the flake to the substrate. The elastic response of the graphene to out–of–plane deformations oppose the nanoscopic and macroscopic tip–sample interactions that would otherwise create a second minimum, binding the flake to the tip. **For intermediate z_t (fig. 2.13(a)) the elastic energy decreases allowing the second minimum, primarily coming from the nanoscopic tip–graphene interaction, to appear.** For small z_t (fig. 2.13(a)), both minima converge into one.

2.5.5 Force curves from multiscale model

In order to compare with experiments, fig. 2.14(a) shows force versus distance curves reconstructed from the potential energy of the model (gradients of minimized potentials with respect to the global and local deformations for different

tip–sample distances). Solid lines correspond to indention curves (1st minimum) and dashed lines to retraction (2nd minimum). Force curves are calculated for the tip on a top (red line) and a hollow (green line) graphene position. Upon indentation, the shapes of the curves follow those obtained through DFT (compare with fig. 2.7). However, for approaching distances closer than ~ 3.5 Å, upon retraction, the graphene sheet adheres to the tip resulting in a large attractive force. When the elastic deformation cost exceeds the graphene-tip adherence energy, the graphene sheet returns towards its equilibrium position. This tip oscillation cycle yields both the dissipation and an increase in the frequency shift; as in the experiments (see fig. 2.6), it occurs at the same z_t as the start of the top/hollow contrast.

The model shows that, upon retraction, the graphene-tip remain adhered, keeping the separation between the apex and the closest atoms of the graphene layer near constant, while these C atoms separate from the Pt substrate. Consequently, in this regime, as in the repulsive regime, the tip is also sensing the local graphene-Pt interaction. These local variations are incorporated into the model through V_{Pt-G}^{local}. It represents the energy difference required to separate the graphene layer from the Pt substrate by pulling from different parts of the moiré (see sec. 2.5.2). With this term, the model predicts AFM moiré contrast. For example, it yields differences in the forces probed on the top–high and top–low sites (see fig. 2.14(b)). **This result points out that the sensing of the moiré through AFM in the attractive region is effectively mapping the local elastic properties of the graphene.**

2.6 Subsurface resolution

SPM techniques are local probes to study surfaces. However, there is an open question about their capabilities to achieve subsurface resolution [226–228]. In order to get subsurface resolution, atoms below the surface should locally modify the tip–surface current/force and these variations have to be large enough compared with those ones coming from the surface atoms. Ideally, the surface should be a weakly coupled thin film or 2D material, like graphene on Pt(111), to prevent propagation of elastic deformations.

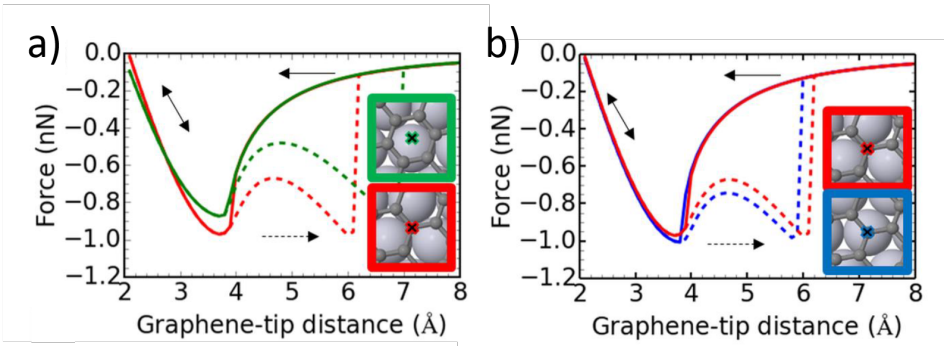

Figure 2.14: Tip–sample force versus distance curves calculated with the multiscale model. For tip approach (solid lines) and retraction (dashed lines). a) For a top site (red lines) and a hollow site (green lines) of the graphene. The model predicts top/hollow contrast of the graphene. b) For the tip on a top-low site (blue lines) and top-high site (red lines). Upon tip approach, the graphene remains adhered to the substrates, however, upon retraction the graphene adheres to the tip giving rise to dissipation energy when the graphene layer disadheres from the tip. Subtle changes in the effective local elastic constant of the graphene gives rise to contrast in the moiré.

In sec. 2.4.2 we discussed how, in the repulsive regime, the non-topographic corrugation of the graphene/Pt(111) 3×3 moiré is obtained by indenting the tip into the graphene sheet deep enough so the displaced carbon atoms act as a tip (see fig 2.15(a)) that allows sensing the Pt surface with local resolution. The obvious questions that arise are: To what extent is this a manifestation of subsurface resolution? What are the limitations of AFM characterization of graphene coated substrates/molecules? To answer these questions, we perform AFM simulations of graphene/Pt(111) with defects: a vacancy, a C and a Pd substitutive atom, and an adsorbed carbon and oxygen atom. As described in sec. 2.2.2, a supercell of 6×6 graphene/Pt with 4 layers of Pt atoms is used in the calculations. For these simulations, the large cell size is not only important for avoiding image tip interaction, but also because the defect breaks the symmetry imposed by the moiré. The deformations induced by the defects should be contained within the unit cell. For our case, none of the defects

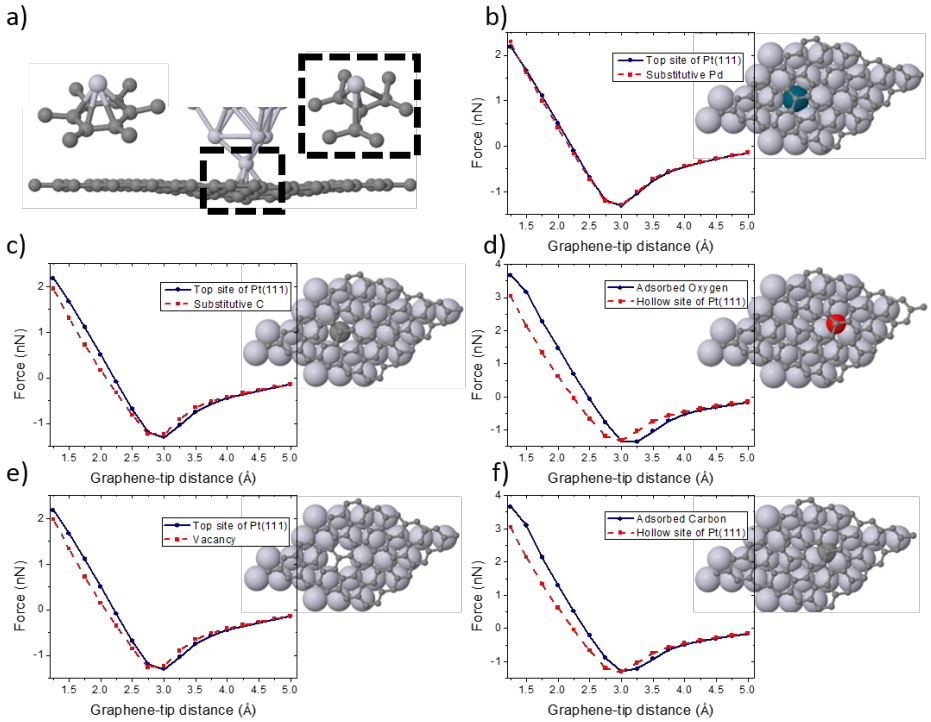

Figure 2.15: Subsurface resolution of single defects on graphene/Pt(111). (a) Relaxed positions of the tip indenting the graphene. DFT force versus distance calculation on the graphene carbon atom that is on top of the (b) substitutive Pd, (c) substitutive C, (d) intercalated O, (e) vacancy, and (f) intercalted C defect, along with the equivalent site without the defect.

promote a significant topographic corrugation and the graphene sheet remains adhered to the substrate.

We performed DFT force versus distance calculations on the graphene's carbon atom that is on top of the defect and compare with the forces on the equivalent sites of the pristine graphene on Pt(111). Fig. 2.15(b-f) shows the comparison of all the defects that were tested. The substitutive Pd atom, the most abundant defect of bulk Pt, resulted in forces very similar to the pristine graphene on Pt(111). This makes sense because both elements have similar chemical characteristics and belong to the same group in the periodic table. In contrast, discrimination was possible for all the other defects. The vacancy

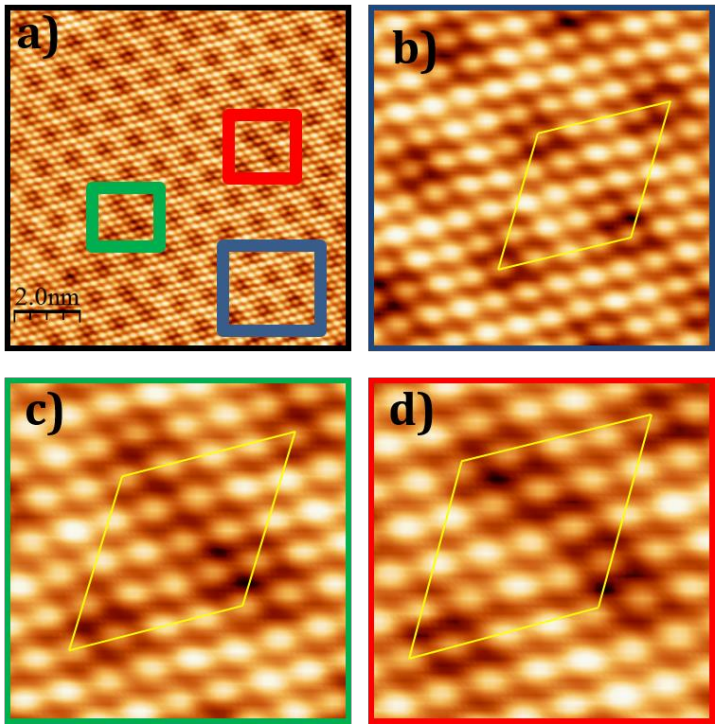

Figure 2.16: Possible subsurface resolution. (a) Topography image in a large graphene/Pt(111) region. (b-d) Zoom of squares marked in (a). While (b) clearly shows a 4×4 moiré, (c-d) have distortions within the marked unit cells. Likely, they are defects of the Pt(111) substrate. Imaging parameters: Δf=-16.9 Hz, A_{osc}=19.3 nm, V_{bias}=0.55 V.

weakens the Pt–graphene coated tip–substrate interaction with the indentation requiring a less energetic cost. The carbon atom, which is highly allotropic, recombines with the Pt atoms and moves towards the bulk and effectively acts as a vacancy site. Lastly, the adsorbed oxygen creates a small bubble in the graphene sheet. Though this slightly decreases the cost of elastic energy deformations [171], the reduced Pt–graphene distance translate into a shift of the interaction curves. For this defect, the increased deformation of the sheet would allow for longer lateral range detection as compared to the other defects.

There is also experimental evidence that the NC–AFM is able to sense Pt defects through the graphene sheet. Although CVD growth facilitates the prepara-

tion of large sheets of graphene without defects, it is still possible to find regions with defects within the moiré modulation. Fig 2.16(a) shows a large region of graphene/Pt(111) with atomic resolution of the 4×4 moiré. In this image there are defect free regions (see fig. 2.16(b)) as well as regions with distortions (see fig. 2.16(c-d)) Likely, they are defects of the Pt(111) substrate sensed through the graphene sheet.

The results described in this section are preliminary and call for a detailed experimental and theoretical study. From the part of the experiments, a precise controlled generation of the defect is needed. In this sense, oxygen intercalation [229] or nitrogen substitution [230] are the best options. On the theory side, more calculations to study the evolution of the contrast along profiles of the unit cell are needed.

2.7 Conclusions

The NC–AFM measurements with Pt–coated Si cantilevers and large oscillation amplitudes presented in this chapter, not only provide atomic contrast but they are able to resolve the moiré pattern formed on the very flat graphene/Pt substrate, where differences in height among the carbon atoms are less than 3 pm. 2D frequency shift and dissipation maps show that the onset of atomic contrast takes place at the same distance where a sudden jump on the energy dissipation is observed. At closer distances, both our images and the 2D frequency shift maps show an inversion of contrast, from honeycomb to hexagonal.

The imaging mechanisms have been unveiled with a combination of direct DFT simulations supplemented with vdW interactions and the development of a multiscale model designed to capture the subtle interplay between local and global deformations in the graphene induced by the combination of chemical and dispersive interactions with the tip. Our calculations confirm that the atomic contrast and the contrast inversion is due to the interaction of a reactive metal apex with the graphene layer. The dissipation is caused by the adhesion of the graphene layer to the tip that deforms the graphene upon retraction. The contrast on the moiré pattern is yielded by the different conformation of the C atoms of the graphene with the underneath Pt atoms, that originates not only

the small graphene buckling and the variation of the electronic structure observed by the STM but also atom–by–atom variations on the graphene–Pt interaction energy which are sensed by the AFM tip. Therefore, the moiré contrast is a local–atomic scale–map of the stiffness of the graphene on Pt. The local differences on the metal–graphene interaction can be measured by the AFM because the tip displaces the atoms of the graphene layer on both the attractive and repulsive regimes. In the attractive regime, upon tip retraction, the graphene layer adheres to the apex. In the repulsive regime, upon tip indentation, the graphene wraps the apex. Thus, the tip–graphene distance varies much less than the graphene–Pt distance leading the tip to sense the graphene–substrate interaction. Our results also suggests that the AFM could achieve sub–surface resolution, locally sensing defects on the substrate. These conclusions, based on the 2D nature and weakly interacting character of graphene, can likely be extended to other substrates and 2D materials.

3 Characterization of CO decorated metal tips for HR–AFM of surfaces

In the previous chapter we studied how the large amplitude cantilever based AFM is capable of capturing very tiny details in the topographic corrugation of weak interacting graphene on metal surfaces. In this chapter, we turn our attention to a different kind of HR imaging, the one obtained from small amplitude AFM measurements with CO functionalized tips.

The HR achieved by the CO tips has been explained in terms of a strong Pauli repulsion between the closed-shell molecule acting as the probe and the electronic charge of the molecule being probed [40, 186]. In addition, the associated tilting of the CO molecule [119, 128, 160, 189] amplifies the spatial variations of the charge density on the sample. Although Pauli repulsion plays a dominant role at very close distances, recent experiments on polar molecules [129, 137, 164, 231], ionic samples [232] and metallic surfaces [112] consistently show that other interactions, in particular ES forces, are also relevant to understand the complex observed contrast. However, contradictory descriptions of the ES behavior of CO molecules when acting as a tip or probed as an adsorbed, make the interpretation of the experiments particularly difficult.

Due to the success of HR imaging with CO tips, it is imperative to have an adequate description of the ES field created by CO tips and to understand how it affects the contrast formation of images. In this chapter we tackle this problem through an *ab initio* study of metallic tips, CO molecules, and CO tips. Additionally, we create a novel model to simulate rapidly interaction–decomposed images using an accurate description of the charge distribution of the CO tip.

With this, we identify the contrast formation mechanisms for localized ionic defects (Cl vacancies on a metal–supported NaCl bilayer) as probed by a CO tip in a qPlus based NC–AFM. With the insight gained from our analysis, we address the apparent contradiction present in the literature pertaining to CO molecules, either as a tip on a metallic apex probing ionic surfaces or as an adsorbate probed with a pure metallic tip. The experiments presented in the chapter were performed by the group of Prof. Leo Gross from IBM Research–Zurich.

3.1 Introduction

3.1.1 Contradictions with regard to the dipole of CO tips

The recent literature includes contradictory statements about the nature of the charge distribution of the CO molecule when acting as a tip or probed as an adsorbate. In the gas phase, CO has a total electric dipole of ~ 0.12 D with its positive pole pointing to the oxygen. However, a CO tip dipole with its negative pole at the O atom (hereinafter called negative dipole) has been invoked by [232] to explain atomic corrugation in AFM measurements with a CO tip on an ionic copper nitride (Cu_2N) surface. The presence of a negative charge at the oxygen in CO tips is also supported by ref. [164] in their analysis of AFM, STM and inelastic electron tunneling spectroscopy (IETS) images of Co phthalocyanines.

Schneiderbauer *et al.* [232] investigated insulating Cu_2N islands grown on Cu(100) by means of combined qPlus sensor STM and AFM with two different tips: a bare Cu metal tip and a CO tip. N and Cu atoms on Cu_2N form a periodic charge arrangement, as calculated by DFT [233]. The polar thin insulating is created by sputtering N gas on a clean Cu(100) crystal, with the N atoms absorbed ~ 21 pm above the Cu hollow sites [234] and with island boundaries and sharp edges determined by the N atoms [235]. This makes possible the designation of the atomic positions of the N^- anions, the Cu^+ cations and the hollow sites thorough STM measurements. Fig. 3.1(a,d) shows the vdW background-subtracted forces [236] obtained experimentally for the metallic tip and the CO tip at closest approach. The authors estimate the distance, referenced with respect to the bare Cu(100), as 125 pm for the Cu

tip and 80 pm for the CO tip. According to the lattice assignment, for the metallic tip, N sites appear most attractive, followed by Cu sites and hollow sites. For the CO tip, the contrast inverts, with N atoms having the most repulsive interactions and hollow sites the most attractive interactions. The authors attribute the contrast inversion to opposite dipole moments of Cu– and CO–terminated tips. Using a point–charge ES model that assigns to the Cu_2N atoms their Barder charge, the magnitude of the dipoles are fitted from the experimental forces; +0.874 D for the Cu tip and -0.166 D for the CO. Fig. 3.1(b,e) shows simulations for the two tips using the purely ES model and fig. 3.1(c,f) experimental/theory line profile comparisons that are in agreement. The positive dipole of the metallic tip (partial positive charge at the apex) is consistent with the Smoluchowski effect [237] that causes charge redistribution on corrugated metal surfaces and leads to the formation of electric dipoles. It is also consistent with previous experimental results [64, 238].

Contrary to this, Schwarz *et al.* [239] use a positive dipole, as in gas phase, to explain the contrast formation of individual CO molecules adsorbed on Cu(111), NiO(001), and Mn/W(001) surfaces and probed with a metal tip. AFM topography images of the CO molecule on the three surfaces are shown in fig. 3.2. The molecule is imaged as hemispherical protrusions at relatively small negative Δf set–points and develop a dip at larger negative Δf set–points, approximately 200 pm closer. That the CO appears as a hemispherical protrusion in constant Δf images is expected, because of the attractive vdW interaction between tip and molecule dominates at large tip–sample distances. The dip observed on smaller tip–sample distances indicates that the interaction is locally repulsive. The authors rationalize the results in terms of the interplay of only two tip–sample interactions, the vdW and a parallel dipole–dipole ES interaction. The locally repulsive dip behavior (middle row of fig. 3.2) is reproduced using a very large dipole for the metallic tip and intricate placements of center of the interaction potentials. The positive dipole behavior is also used by Gao *et al.* [64] to explain the double rings that appear on images of a CO molecule adsorbed on an NiO(001) surface probed with metallic multi-tips.

Strikingly, the dipole orientation is not even consistent among studies of the

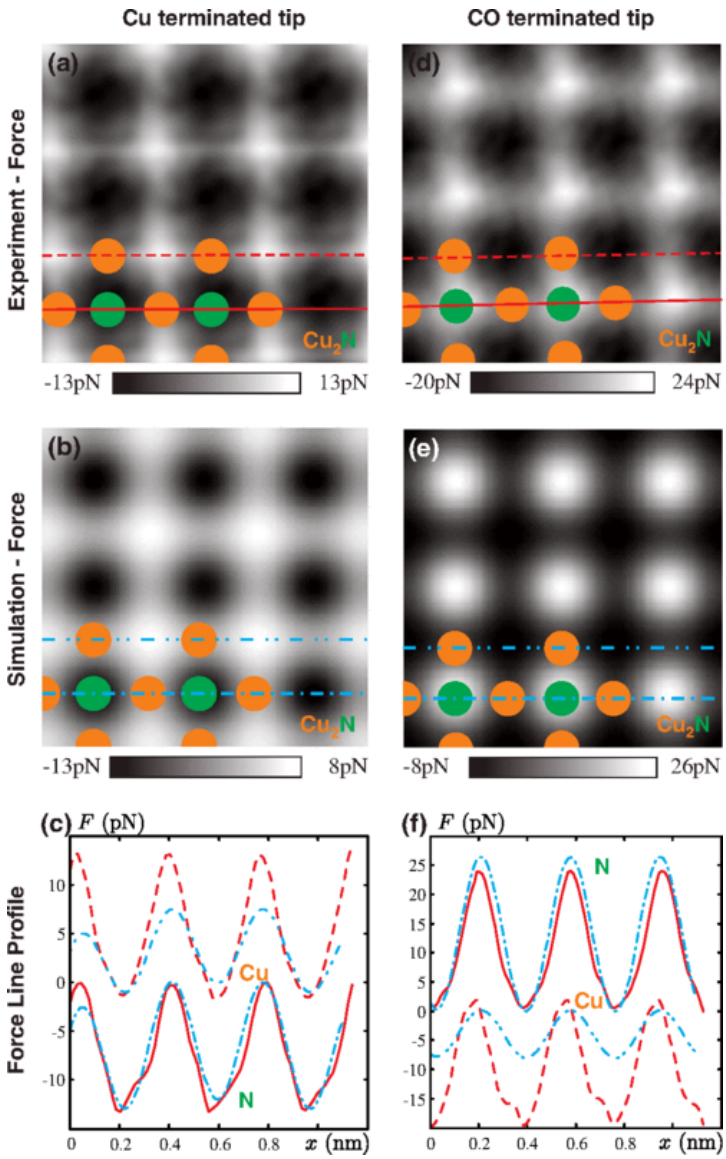

Figure 3.1: NC–AFM data of insulating Cu_2N islands grown on Cu(100) with a (left) Cu–terminated tip and a (right) CO tip. Top row: vdW–subtracted force between the tip and sample at closest approach. Middle row: Simulated dipole–charge tip–sample ES interaction. Bottom row: Line profiles along N–Cu–N and Cu-hollow site–Cu directions. Reproduced with permission from [232].

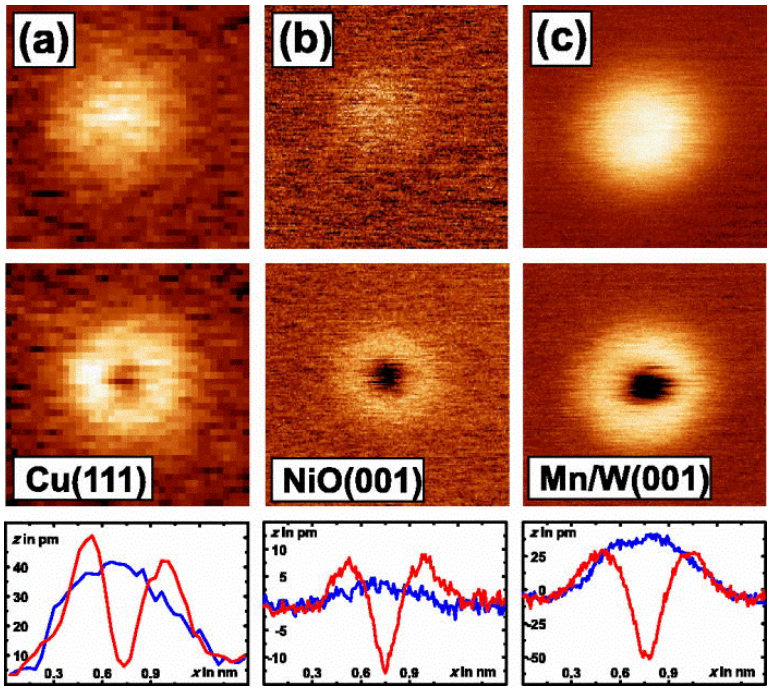

Figure 3.2: NC–AFM constant interaction (Δf) images of single CO molecules on (a) Cu(111), (b) NiO(001), and (c) Mn/W(001). Images in the middle row are recorded with more negative Δf set-points leading to < 0.2 nm smaller tip–sample separations. The lower row shows the corresponding line profiles. Reproduced with permission from [239].

CO molecule as an adsorbate, as ref [240] explain their measurements for CO on a Cu surface with a negative dipole, just the opposite of the proposal described above (and reported in [64, 239]) on the same system. Following [69, 241], Hofmann *et al.* [240] use the COFI (CO front atom identification) technique to study Cu tips with different orientations. The technique uses AFM images of CO molecules adsorbed on substrates to extract information of the probe. The authors studied three tip terminations, obtained through gentle poking [241] trial and error, and identified as high–symmetry Cu tips carved from directions (100) (fig. 3.3(a)), (111) (fig. 3.3(f)), and (110). The last one was later proven to be a tetramer tip [112, 242]. Images from the first two tips have circular symmetric (fig. 3.3(c),(h)) with an attractive dip and a small repulsive rings.

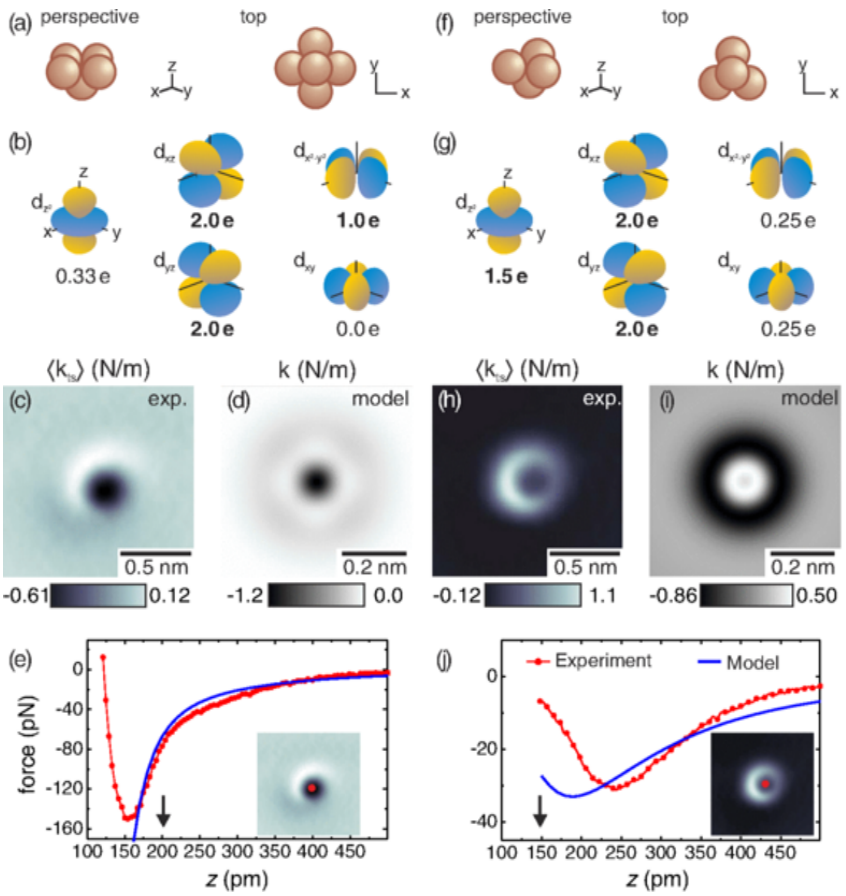

Figure 3.3: COFI images assigned to high–symmetry Cu clusters pointing in the (left) (100) and (right) (111) direction. First row: Schematic representation of the tips. Second row: Occupation of d orbitals, determined by the angular overlap with the nearest neighbors, that describes the model tip. Third row: experimental and theory images. Forth row: Experimental/theory force versus distance plots. The arrows indicate the tip–sample distance of (d) and (i). Reproduced with permission from [240].

The results are rationalized in terms of a simple ES model [241] that is based on the partial filling of the d orbitals of the Cu tip and a negative dipole for the CO adsorbed molecule. The model produces images (see fig. 3.3(d),(i)) with a qualitative acceptable resemblance to the experimental ones.

3.1.2 Tip characterization by probing surface charged states

Surface charge states are ideal systems for tip characterization. By placing markers with well known adsorption sites, the lattice of a surface is unambiguously identified without prior tip information [238]. Next, the interaction between the tip and known charge states of the surface is measured. This interaction, predominantly ES, determines the polarity of the tip [16].

Gross *et al.* [60] expand this concept by characterizing Cu, Au, Cl and Xe terminated Cu tips using single Cl vacancies on a 2ML-NaCl(100)/Cu(111) surface. In addition to providing unambiguous lattice identification for the Na^+/Cl^- ionic lattice position, the vacancy provides an extra (positive) charge state [243]. Fig. 3.4 shows CH–AFM images of the surface taken with the four tips. Whereas the Cu and Xe tip image the vacancy as repulsive (bright) features, the Au and Cl tips images the vacancy as an attractive (dark) feature. With calculated dipole moments of 0.53 D, -1.05 D, -5.87 D, and 2.92 D for the Cu_5, Cu_4Au, Cu_5Cl and Cu_5Xe respectively, as obtained from DFT, the contrast can be explained by the ES dipole–charge interaction between the tip and the positive vacancy: Cu and Xe tips have a positive dipole and image the positive vacancy as repulsive and the Au and Cl tips have negative dipoles and image the vacancy as attractive. In accordance, for all tips except the Au, the contrast on the Na^+ sites is the same as the contrast of the vacancy. The authors propose two possible explanations for the inconsistency of the Au tip: 1) the uncompensated positive charge of the vacancy induces an image charge on the tip that changes it's polarity as a function of the tip position and 2) a fuller picture of the ES nature that accounts for a higher order quadrupole [130] is needed to explain the ES interaction between the tip and the sample.

3.1.3 Overview

With a combined experimental and theoretical approach, in this chapter we study the ES field generated by CO functionalized metal tips and determine the role it plays in AFM experiments. The chapter is organized as follows. First, we analyze separately the ES field created by a CO molecule (sec. 3.3)

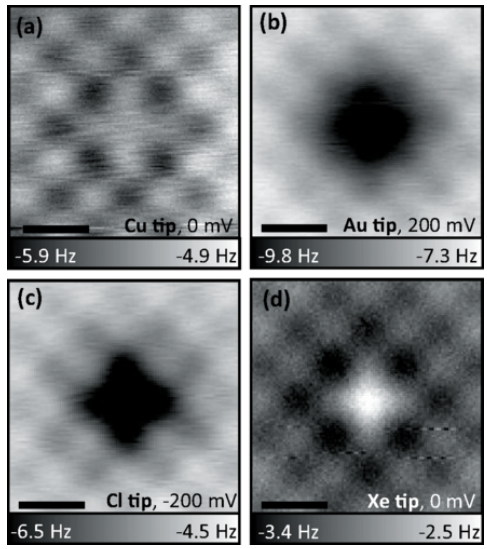

Figure 3.4: CH–AFM maps obtained at constant sample voltages V acquired with tips terminated with Cu, Au, Cl, and Xe, respectively. (a) Cu tip, $V = 0$ mV, (b) Au tip, $V = 200$ mV, (c) Cl tip, $V = -200$ mV, (d) Xe tip, $V = 0$ mV. The voltage V was chosen to roughly compensate for the local contact potential difference (LCPD). Oscillation amplitude $A = 0.5$ Å. All scale bars are 5 Å. Reproduced with permission from [60].

and a metal tip (sec. 3.4). DFT calculations provide the basis for the analysis of the CO–decorated metal tips presented in sec. 3.5. The theoretical model to simulate HR–AFM images with metal–CO tips is introduced in sec. 3.2.3. Sec. 3.6 validates our model through the comparison with AFM measurements of Cl vacancies on a supported NaCl bilayer. Here, we discuss how to determine the dipole of the metal tips used in the experiment, illustrate the very different nature of the ES contributions of the CO molecule and the metal tip, and show how their interplay gives rise to the complex AFM contrast observed. The chapter concludes with a detailed analysis of the inverse problem (sec. 3.7): the imaging with metal tips of CO molecules adsorbed on metal substrates. Our study reveals the limitations of previous models based on the assumption of a positive CO dipole and sheds new light on the interpretation of the AFM contrast in this classic surface science system.

3.2 Methods

3.2.1 Experimental

Measurements were performed by our experimental collaborators using a home-built combined STM and AFM operating in UHV (base pressure 10^{-10} mbar) at a temperature of $5\,\mathrm{K}$. The voltage V was applied to the sample. The AFM is based on a qPlus sensor [37, 244] (stiffness $k \approx 1800\,\mathrm{N/m}$, eigenfrequency $f_0 = 29664\,\mathrm{Hz}$, quality factor $Q \approx 2 \times 10^5$) operated in FM mode [22]. The PtIr tip was cut to length and sharpened using a focused ion beam setup. All AFM images were acquired at $V = 0\,\mathrm{V}$ to avoid any cross-talk of the current and force signals, and which was also within a few 100 mV of the local contact potential difference [60]. The oscillation amplitude was 50 pm to maximize the lateral resolution on atomic length scales [6].

A Cu(111) single crystal was cleaned by several sputtering and annealing cycles. Ultrathin NaCl films were grown by thermal evaporation of NaCl on Cu(111) at a sample temperature of about $270\,\mathrm{K}$. Defect-free (100)-terminated islands of mainly two atomic layers were formed [245]. Low coverages of CO molecules were adsorbed at sample temperatures below 10 K.

3.2.2 DFT calculation details

All DFT calculations were carried out using the Projector-Augmented-Wave (PAW) method as implemented in Vienna Ab initio Simulation Package (VASP) [245]. We have used the PBE [209] XC functional supplemented by semi-empirical DFT–D3 vdW interaction [223], a plane wave cutoff of 400 eV, and fine electronic convergence ($E_{\mathrm{SCF}} = 10^{-4}$ eV) on all calculations. Furthermore,

- All volumetric data was calculated on a uniform mesh with 0.075 Å grid spacing with the dipole correction applied to the z-direction. For the ES potentials, a uniform 1D filter in the z-direction was applied to the volumetric data in order to eliminate high frequency noise ($\lambda = 2$ grid points). The z-component of the E–fields shown in secs. 3.3, 3.4, 3.5, and 3.7 was calculated from the gradient of the ES potential.

- Calculations used to fit the model (sec. 3.2.3) used a $3 \times 3 \times 1$ grid for sampling the Brillouin zone.

- Sec. 3.2.3 calculations used the Γ point for the sampling of the Brillouin zone and ionic relaxations were considered converged when forces were less than 10^{-2} eV/Å.

- Sec. 3.2.3 calculations used a $7 \times 7 \times 1$ grid for the sampling of the Brillouin zone; ionic relaxations were considered converged when forces were less than 10^{-2} eV/Å.

3.2.3 HR–AFM image simulation method with metal–CO tips

In the preceding sections, we have characterized with DFT the ES field of a metallic tip functionalized with a CO molecule. We have shown that while the metallic tip acts as a large positive dipole (partial positive charge at the tip apex), the CO introduces a dome with an opposite sign that is repulsive towards electrons. As discussed in the introduction, previous works present contradictory explanations for the behavior of metal–CO tips. In order to solve this puzzle, we have to understand the interplay between the ES interaction of the extended positive dipole of the metallic tip and the localized repulsive dome of the CO molecule on the contrast formation of charged systems as probed by metal–CO tips.

In this section, we present the method that we have developed to calculate interaction-decomposed HR–AFM images with molecule decorated metal tips. It is based on DFT calculations and allows an efficient simulation of AFM images while retaining the first–principles accuracy needed to cover the whole distance range explored in the experiments, and to single out the different contributions to the total tip–sample interaction. In sec. 3.2.3, we introduce the potential used to simulate images. It encompasses ES, SR, and vdW interactions and explicitly accounts for tip tilting effects. It is clearly necessary to validate experimentally our model. Sec. 3.2.3 motivates and describes the system that we have chosen for the theory–experiment comparison: a Cl vacancy on a NaCl(100) bilayer supported on a Cu(100) substrate [60, 243, 246, 247]. Finally, in sec. 3.2.3, we

expand the discussion of the CO probe tilt by comparing AFM spectroscopies calculated with the model and with DFT.

Description of the tip–sample interaction potential

Our approach differs from previous theoretical models [160, 164] in two important aspects. We go beyond the simple dipole approximation for the CO probe and calculate the ES energy by the interaction of the sample ES potential (obtained from a DFT calculation) with the charge density of both the CO molecule (also calculated with DFT) and the metal tip apex (replaced by a positive dipole). While accounting for tip tilt, the full charge density of the CO molecule (on a real–space grid) is rotated. We also include a more accurate description of the SR interaction, which is modeled as a sum of pair–wise Morse potentials with species–dependent (in this case Cl and Na) parameters fitted to reproduce our DFT force calculations. The vdW contributions are included with a semiempirical DFT–D3 approach [223], while the CO tilting is simulated by a spring [160] with a force constant of 0.24 N/m [231].

HR–AFM images obtained from CO functionalized metallic tips are simulated by minimizing the potential

$$V = V_{\text{tilt}} + V_{\text{vdW}} + V_{\text{SR}} + V_{\text{ES}} \tag{3.1}$$

for the probe position.

The CO tilting is defined through

$$V_{\text{tilt}} = \frac{1}{2}\kappa\delta^2\theta^2, \tag{3.2}$$

where $\delta = 302$ pm is the lever arm (distance from the outmost Cu atom of the tip to the O of the CO probe), $\kappa = 0.24$N/m [231] is the spring constant, and θ is the tilt angle. Sec. 3.2.3 discusses the suitability of this model in terms of DFT calculations.

The vdW interaction, not properly described by any of the XC functionals commonly used in DFT simulations, can be included through any semi-empirical method as a correction to the DFT total energy. Specifically, here we use Grimme's DFT–D3 method [223]. The same correction is applied to the DFT

energy used in the parametrization of the model. All the atoms from the sample, the CO probe, and the metal tip – modeled by a 20 atom Cu cluster – are included in the calculation. Although absolute vdW forces depend on the macroscopic part of the tip, the vdW contribution to the force contrast (the difference between forces on different sites) is well converged for this cluster size.

The SR contribution is approximated using a sum of pair–wise interactions between the CO probe and all of the Na(Cl) atoms in the sample. We have found that the best description for each of these interactions is obtained with a Morse potential,

$$V(r) = D_e((1 - e^{-a(r-r_e)})^2 - 1), \tag{3.3}$$

where D_e , a, r_e are the well depth, width of the potential, and equilibrium bond distances, respectively. Note that the Cu substrate is not included in the calculation of the SR interaction. Due to the SR nature of the Morse potentials, the exclusion of the Cu atoms is justified. The procedure used to parametrize the potential is described in appendix 3.2.3.

The ES interaction is calculated from

$$V_{\mathsf{ES}} = \int (\rho_{\mathsf{CO}} + \rho_{\mathsf{metal}})\Phi_{\mathsf{sample}}\mathrm{d}\mathbf{r}^3, \tag{3.4}$$

where ρ_{CO} and ρ_{metal} are the charge density of the CO probe and the Cu metal tip, and Φ_{sample} the ES potential of the isolated surface (NaCl and substrate). The charge distribution and the ES potential are calculated on a real–space grid (see appendix 3.2.2 for details). The charge distribution of the Cu tip is simulated by two opposite localized charged Gaussian distributions (width at half-maximum of 10 pm) separated by 106 pm and centered 53 pm from the last Cu atom. It provides a net 1.5 D dipole. Notice the increase of the dipole size that simulates the metallic tip as compared to the dipole strength predicted by DFT and discussed in sec. 3.4. The increment will be justified in sec. 3.6.3.

Cl vacancy on a NaCl/Cu(100) Surface

In order to test the tip–sample interaction potential and the model tip described above, we have compared their predictions with an experimental NC–AFM study

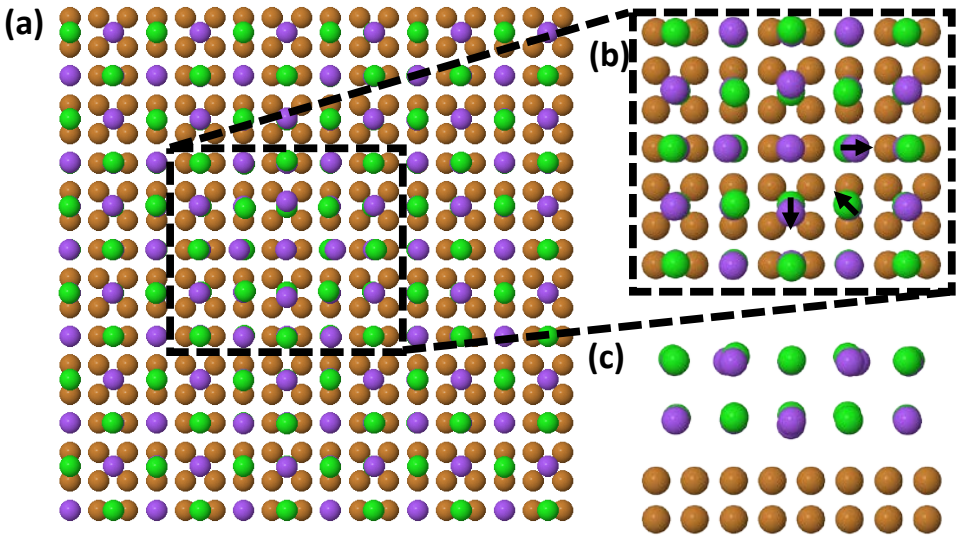

Figure 3.5: (a) Cell used for the simulation of AFM images. The cell size is (33.7 × 33.7 × 48) $Å^3$. It includes a NaCl bilayer with a Cl vacancy (143 Cl atoms and 144 Na atoms), on 2 layers of Cu(100) (324 atoms). (b) Top and (c) lateral view of the atoms near the vacancy (area marked by dashed lines in the left panel). Na atoms adjacent to the vacancy relax away from the vacancy, while Cl atoms relax towards the vacancy. In addition, the Cl atoms shift away from the substrate.

of a single Cl vacancy on a NaCl bilayer supported on a Cu(111) substrate probed by a Cu–CO tip. This sample is ideal for such a task because, in addition to the ionic lattice, there is a net positive charge at the vacancy site leading to three qualitatively different sites: Na cations (Na^+), Cl anions (Cl^-), and the net positively charged vacancy site [60, 243, 246, 247].

In our calculations, we have simulated this system with a single Cl vacancy on a NaCl bilayer supported on a 2-layer Cu(100) slab. We use a 6×6 surface unit cell and a large vacuum (33.7 Å × 33.7 Å × 48 Å) (see fig. 3.5). We calculate the ionic structure with VASP [245], using the PBE [209] XC functional supplemented by semi-empirical DFT–D3 vdW interaction [223], a plane wave

cutoff of 400 eV, a fine electronic convergence ($E_{\text{SCF}} = 10^{-4}$ eV), a $3 \times 3 \times 1$ grid for the sampling of the Brillouin zone, and a force cutoff for ionic relaxations of 10^{-2} eV/Å.

The main structural difference introduced by the Cl vacancy with respect to the clean NaCl bilayer is that Na ions adjacent to the vacancy shift away from the vacancy approximately 30 pm, while the Cl ions shift towards the vacancy by 15 pm (fig. 3.5(b)). In addition, the Cl ions adjacent to the vacancy also shift away from the substrate approximately 30 pm (see fig. 3.5(c)).

Parametrization of the SR interactions

In order to parametrize the Morse potentials of the SR interaction, we perform static DFT force calculations on a clean NaCl bilayer on a 4–layer Cu(100) slab probed by a CO molecule on a $2\sqrt{2} \times 2\sqrt{2}$ unit cell with a large vacuum (total cell size 15.9 Å $\times$ 15.9 Å $\times$ 42 Å) (see fig. 3.6(a)–(b)). Calculations were carried out in VASP [245], using the PBE [209] XC functional supplemented by semi–empirical DFT–D3 vdW interaction [223], a plane wave cutoff of 400 eV, a fine electronic convergence ($E_{\text{SCF}} = 10^{-4}$ eV), and a $7 \times 7 \times 1$ grid for the sampling of the Brillouin zone. Force curves were calculated with a 25 pm interval on 3 different sites: Cl, Na, and bridge (defined as the midpoint between a Na and Cl site). Figs. 3.6(c)–(d) show the total and vdW forces obtained for those three sites (red, blue, and yellow markers correspond to the Cl, Na, and bridge sites in fig. 3.6(c)–(d). The ES interaction is calculated, as in the model, from

$$V_{\text{ES}} = \int \rho_{\text{CO}} \Phi_{\text{sample}} \mathrm{d}\mathbf{r}^3$$

(see fig. 3.6(e)). Finally, the SR contribution (fig. 3.6(f)) is obtained from

$$V_{\text{SR}}^{\text{DFT}} = V_{\text{total}}^{\text{DFT}} + V_{\text{vdW}}^{\text{DFT}} + V_{\text{ES}}$$

and fitted, through a least-squares method, to a sum of Morse potentials,

$$V_{\text{SR}} = \sum_{i=\text{Na,Cl,ions}} D_e^i \left((1 - \exp\left[-a^i(|\mathbf{x} - \mathbf{x}^i| - r_e^i)\right])^2 - 1 \right),$$

where $|\mathbf{x} - \mathbf{x}^i|$ is the distance between the O atom in the CO probe and the corresponding ion, D_e^i (well depth), a^i (that controls the inverse of the width

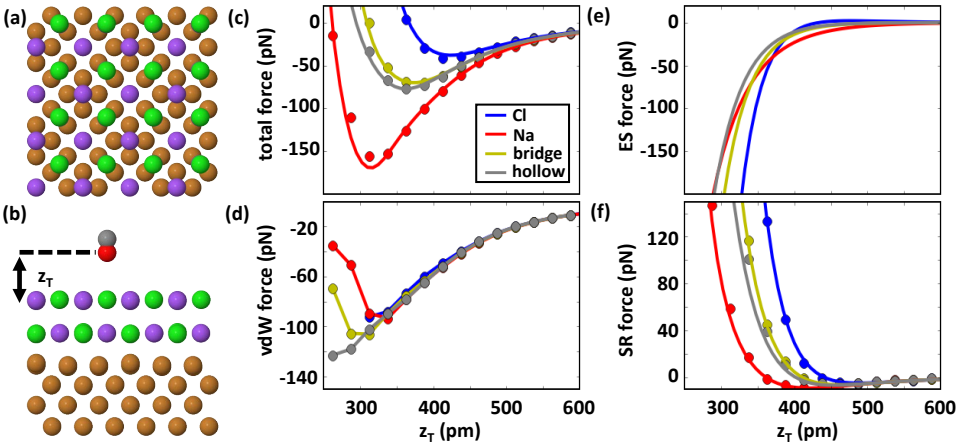

Figure 3.6: (a) Front view of the relaxed clean NaCl/Cu(100) surface used in the DFT spectroscopy calculations. (b) Lateral view of the surface along with the CO probe. (c) Total, d) vdW, e) ES, and (f) SR forces for Cl (blue), Na (red), bridge (yellow) and hollow (gray) sites. Markers correspond to DFT data while the lines to calculations with the model. The Cl, Na, and bridge sites were used in the parametrization of the SR interaction, while the hollow site is calculated to show the ability of the model to reproduce the DFT results on any point of the surface.

of the potential), and r_e^i (equilibrium bond distance) are the species dependent parameters determined by the fitting, and the sum extends to all the atoms of the ionic surface.

Results for the total, vdW, ES, and SR forces on the three sites are plotted on fig. 3.6(c)–(f). Bullets correspond to the values obtained from DFT calculations and lines represent the results from the model. Note that the DFT–D3 theory is used to estimate the vdW interaction both in the DFT calculations and in the model; hence, markers and lines of fig. 3.6(d) are identical. For the three sites, forces calculated with DFT and the model are in complete agreement. Table 3.1 shows the fitted parameters.

In order to assess the transferability of our model to sites different from the ones included in the SR fitting, we have tested the predictions of the model for a new site: a hollow position (defined as the midpoint between two Cl atoms).

	D_e (Ha)	a (Bohr^{-1})	r_e (Bohr)
Na-CO	8.15E-15	1.62	12.82
Cl-CO	7.65E-05	0.80	8.61

Table 3.1: Morse potential parameters fitted from DFT calculations. These parameters provide an excellent fit to the DFT force curves.

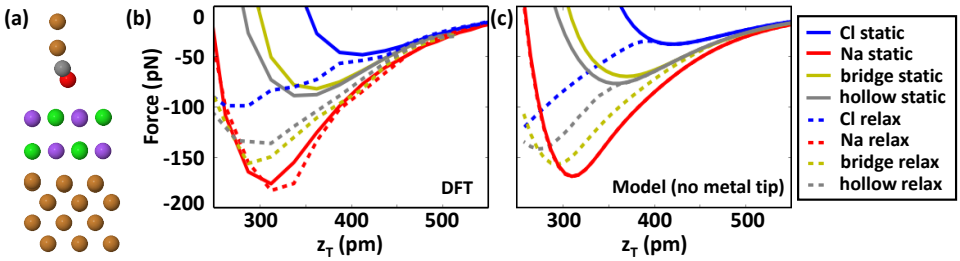

Figure 3.7: (a) Lateral view of the DFT cell and the Cu_2–CO probe used in the tests for the description of the CO tilting. (b) Force curves with (dashed) and without (solid lines) CO tilting. The tip was moved in 25 pm intervals. (c) Forces computed with the model (only the CO probe was used as a tip).

Fig. 3.6 shows the full agreement between the DFT calculations (grey markers) and the model (grey lines) on this site.

CO tilting: DFT versus model calculations

In order to corroborate that the spring model with $\delta = 302$ pm and $\kappa = 0.24$ N/m treats the CO tilting correctly, we have carried out DFT force calculations of a clean NaCl bilayer on a 4–layer Cu(100) slab probed by a Cu_2–CO tip on a small cell. The Cu_2–CO tip is a Cu dimer with a CO molecule attached from the C atom. Fig. 3.7(a) shows the NaCl/Cu(100) sample (7.95 Å $\times$ 7.95 Å unit cell) along with the tip. Fig. 3.7(b) shows DFT force curves with (dash) and without (solid) relaxation of the CO probe. Fig. 3.7(c) shows force curves calculated with the model on the sites mentioned above. The quantitative and qualitative behavior of the CO bending is well described by the model.

The arm length, $\delta = 302$ pm, used to describe the tilt of the CO molecule

on the Cu tip is obtained from DFT calculations of a CO molecule adsorbed on a 4 layer (111)-oriented Cu tip (Cu_{20} tip). It is the length from the O atom to the outmost Cu atom. This arm length is well converged for this tip size. It is worth noting that the CO bond length calculated from DFT is 115 pm, thus the C-Cu adsorption length is 187 pm.

3.3 The dipole of CO molecules in gas phase

In the gas phase, the carbon monoxide (CO) molecule has a total electric dipole of +0.12 D with its positive pole pointing towards the oxygen [248]. This is counterintuitive from an electronegativity point of view, however, because the CO triple bond contains one dative bond with both electrons stemming from the oxygen, the corresponding shift of electron density overcompensates the larger electronegativity of oxygen. The interplay between the oxygen lone pair and the overall positive dipole creates an ES field with complex characteristics. To investigate this, we plot in fig. 3.8(a),(d) the z-component of the E–field of the molecule in gas phase as calculated with DFT (see appendix 3.2.2 for details of the calculations) near the molecule and far from the molecule, and in fig. 3.8(b),(e) their respective profiles along the axial line that passes through the CO. Although the net dipole of the CO is positive, close to the molecule the O's lone pair dominates, resulting in an E–field that is repulsive towards electrons (represented by the red dome in fig. 3.8(a)). It is only past 20 Å that the multipolar approximation becomes valid and the field, dominated by the positive dipole, inverts sign (see figs. 3.8(d)–(e) for the far field). The question is whether such a dipole can be measured by AFM with a metallic tip. Supposing the metallic tip behaves as a positive dipole with a dipole moment $p = 1$ D, the ES force exerted by the CO can be computed as

$$F = -p\frac{dE_z}{dz}. \tag{3.5}$$

As shown in fig. 3.8(f), the maximum force exerted after the inversion of the field (positive dipole behavior) is 0.1 fN. This magnitude of force is outside the experimental range of measurement of the AFM.

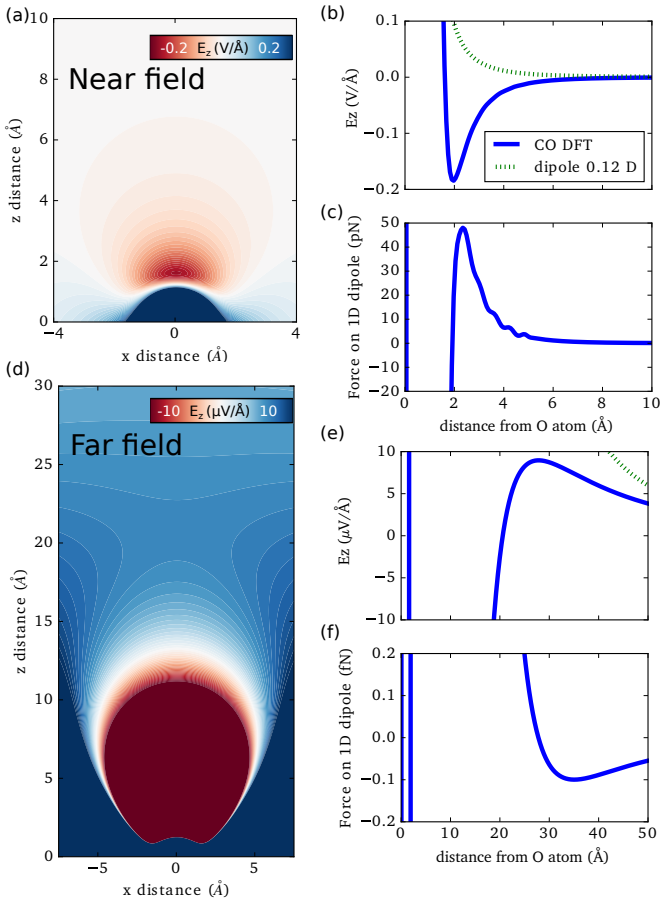

Figure 3.8: z-component of the E–field of a CO molecule in gas phase near (a) and far (d) from the molecule. z-component of the E–field along the axial line of the CO near (a) and far (d) from the molecule. The ES force exerted by the CO molecule on a 1 D dipole near (c) and far (f) from the molecule. In all cases, the oxygen atom is placed at the origin $x, z = 0$ Å.

3.4 The electric field of metallic tips

In many instances, Si cantilevers or quartz sensors are coated with a metal through direct evaporation or controlled contact with the surface. If the resulting tip apex is sufficiently sharp, it can be used to image surfaces with atomic resolution. The resolution of the AFM is further increased by functionalizing the

metallic tip with a CO molecule [40]. In either case, an accurate characterization of the charge distribution of metallic tips is of utmost importance for the correct interpretation of the AFM images.

It has been recently shown that metallic tips have a positive dipole (partial positive charge at the tip apex) [60, 64, 238, 249]. In analogy to the surface dipole of adatoms, it can be explained by the smooth contour followed by the charge density that leaves an excess charge at the base of the protrusion and a lack of charge at the cusp [237]. In order to characterize the E–field created by metal tips, we have considered a Cu_{20} tip (see fig. 3.9(a)) obtained by carving a 4–layer pyramid out of a Cu(111) slab. This pyramid is a realistic model tip as it exposes (111) faces that correspond to the more compact and more stable planes in an FCC structure.

Fig. 3.9(b) shows the z-component of the E–field of the tip as obtained with DFT (see appendix 3.2.2 for details of the calculations). Indeed the charge density results in an ES potential that acts quantitatively as a positive dipole, both in the z and x–y directions. Furthermore, the strength of the dipole is larger than that of the surface dipole of the Cu(111) surface. However, the field cannot be quantitatively reproduced by that of a dipole for the full range of distances. Thus, we attempt to quantify the dipole for two different ranges of distances. This is done through a least-square fit to the analytical equation of a dipole along the axial symmetry line, assuming that the dipole is located at the position of the apex atom. Close to the apex (z =1–5 Å), the field can be reproduced by a large +3.5 D dipole centered at the tip apex (see fig. 3.9(c)). This range of distance is relevant for interpreting NC–AFM images taken with metallic tips. Also, the result is consistent with previous works [64]. However, beyond $z = 5$ Å, the strength of the field decreases. At large distances, (z =6-13 Å), the dipole decreases to 0.9 D (see fig. 3.9(d)). A slightly better fit is obtained by relaxing the degree of freedom of the dipole origin. A dipole of 0.7 D centered 53 pm from the apex (away from the tip) best reproduces the field for intermediate distances. As we will see in the next section, this distance range is important for understanding the ES interaction of metallic tips decorated with CO molecules.

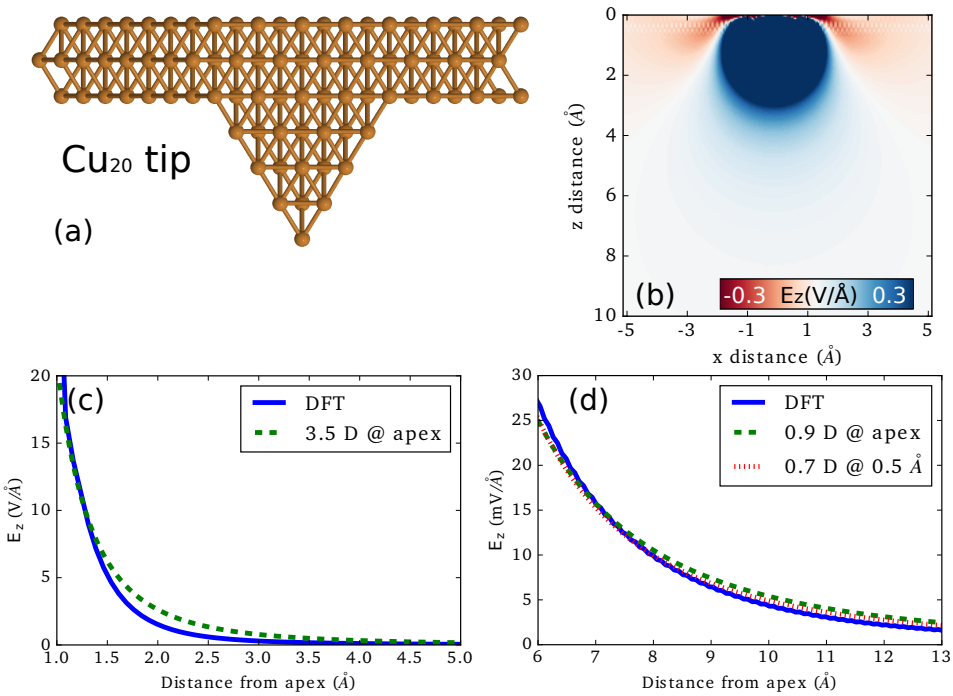

Figure 3.9: Cu_{20} pyramid tip carved from a Cu(111) surface. (a) Ball–and-stick model. (b) Contour plot of the z-component of the E–field obtained from DFT calculations. The tip apex is centered at the origin $z = 0$ Å. (c) Comparison of the z-component of the E–field along the axial line from DFT and that of a +3.5 D dipole located at the apex atom. (d) Same as (c) for the intermediate distance range, considering both a +0.9 D dipole located at the apex atom, and a +0.7 D dipole centered ~ 0.53 Å away from the tip apex that provides the best fit to the DFT results. Note that the z-component of the electric field for the +3.5 D dipole lies outside the scale in (d).

Although the presence of a positive dipole for metallic tips is consistent with experimental observations, DFT seems to constantly underestimate the value of the dipole of metallic tips as compared to the dipoles needed to explain experimental results [60, 64, 238, 249]. It can be argued that, since the metallic tip dipole originates from the Smoluchowski effect [237], it must increase as a function of the tip size (number of layers of the pyramidal cluster). DFT indeed

reproduces this behavior: As shown in fig. 3.10(a), the dipole for a Cu tip carved from a Cu(111) surface increases as a function of the number of layers, with the dipole/layer remaining constant. However, this increment in the size of the dipole moment is associated with the increase in the separation of the partial charges between the tip apex and the base of the cluster. In this case, it is no longer justified to assume that this dipole is located at the tip apex.

Alternatively, we propose to take the electric field created by metallic tips as the relevant physical magnitude. This quantity converges rapidly with the number of layers and can be well described fitting the value and the origin of an electric dipole, as discussed below. We have calculated with DFT the electric field of metallic tipsd as a function of the tip size. Fig. 3.10(b) shows the z-component of the E–field along the symmetry line of Cu tips carved from a Cu(111) surfaces of size 2 through 7 layers. In contrast to the net dipole (fig. 3.10(a)), there is no major change in the behavior of the field as a function of the tip size for tips larger than 4 layers. The small variations in the shape of the field for tips 4-7 can be attributed to the staking of the FCC[111] planes. The stark contrast between the pictures painted by the total dipole moment as calculated by integrating the charge density (fig. 3.10(a)) and by examining the electric field (fig. 3.10(b)) can be rationalized by a displacement of the origin of the dipole moment. If the dipole is increasing as a function of the tip size, then the origin of the dipole must be moving away from the apex and towards the inside of the pyramidal tip. It is worth noting that the behavior occurs on isolated clusters as well as on clusters attached to metal surfaces: The E–field is attractive towards electrons and there is no quantitative variation of the field as a function of the tip size.

In order to interpret AFM experiments and to construct models that simulate AFM images, one needs to go beyond a qualitative description of the potential of the tip. For the distance regime of interest for AFM (3-10 AA from the tip apex), the z-component of the E–field of the Cu_{20} metallic tip obtained from DFT (see fig. 3.9) is reproduced by replacing the Cu tip by a dipole of 0.7 D centered 53 pm away from the tip apex. With a slightly worse overall fit, if the dipole is placed at the tip apex, the dipole value is reduced to ≈ 0.5 D. This

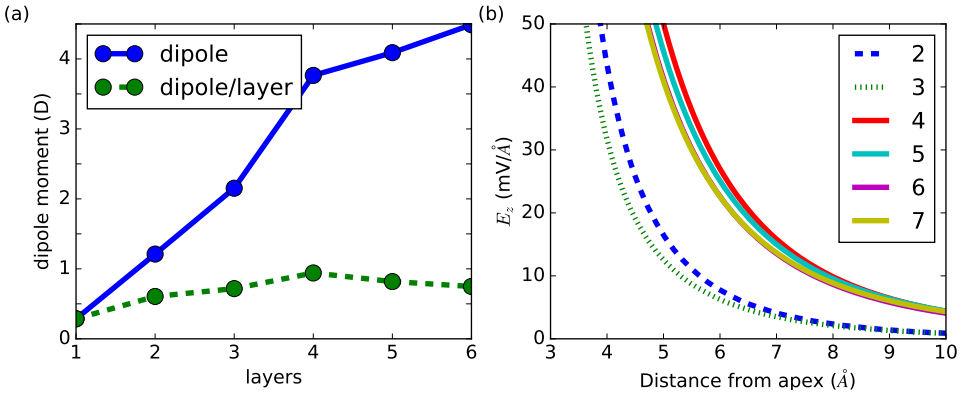

Figure 3.10: (a) Total dipole moment as calculated from the charge density (solid blue line) and dipole moment per layer (dashed green line) for Cu tips obtained by carving a Cu(111) slab with different number of layers. (b) z-component of the E–field along the symmetry line of the Cu tips, showing that, contrary to the total dipole moment, past 4 layers there is no significant change in the E–field as a function of the number of layers.

result is consistent with previous works [60].

3.5 The electric field of metal–CO tips

The use of metal tips functionalized with CO molecules has allowed AFM to image surfaces and molecules with unprecedented resolution [40]. Although most images are taken at close tip–sample distance where the dominant interaction is Pauli repulsion, on polar molecules and ionic surfaces, the ES interaction should play an important role on the contrast formation. Thus, the accurate characterization of metal–CO tips is important. In previous sections, we have examined separately the isolated CO molecule and metallic tips and found that they have opposite dipole behaviors at distances relevant for AFM imaging. We proceed now with the study of composite metal–CO tips in order to (1) find out how much does the metal–CO bonding affect the ES behavior of both the CO molecule and the metal tip, and (2) get a qualitative description of the net E–field. As before, we will use the Cu_{20} tip as a model tip.

DFT calculations of Cu–CO tips show that the CO molecule bonds to the

terminal Cu atom in an upright position with negligible structural changes (ionic relaxation) on the part of the CO molecule and the metal tip, and negligible charge transfer between the structures (see appendix 3.2.2 for details of the calculations). In fig. 3.11(a)–(b) the electronic charge density of a CO molecule and a Cu_{20}–CO tip are plotted. Around the CO molecule, the charge density is not affected by the presence of the metallic tip. This is seen more clearly in fig. 3.11(c)–(d) where we plot the xy–plane averaged charge density of the CO molecule (solid blue lines) and Cu_{20}–CO tip (dashed red lines) around the axial symmetry line. Around the CO molecule, the charge densities are superimposed, thus confirming the absence of a significant charge redistribution between the CO and the metallic cluster. This result suggests that the ES behavior of the compound Cu–CO tip is additive [250].

A further examination of the ES behavior of the isolated CO molecule and the compound Cu_{20}–CO system confirms this. Fig. 3.12 shows the z-component of the electric field (E_z) of a 4 layer (111)–oriented Cu tip (Cu_{20} tip) functionalized with a CO molecule. In fig. 3.12(a), the fields along the axial symmetry direction are plotted for the isolated CO molecule, the isolated metal tip, the sum of the isolated fields, and the field of a Cu_{20}–CO tip. Along the symmetry line, the sum of the isolated fields is practically identical to the one of the compound Cu_{20}–CO tip. As discussed in sec. 3.4, the field of the metal tip can be replaced by that of a dipole. For distances relevant for AFM images with metal–CO tips ($z = 3 - 10$ Å from the O atom), we find, through a least-square fit along the axial line, that the field of the Cu tip can be substituted by a +0.7 D dipole centered 53 pm away from the outmost Cu atom. A 2D slice of the z-component of the fields of a Cu_{20}–CO tip and a 0.7 D dipole added to the field of a CO molecule are plotted in fig. 3.12(b)–(c). The comparison confirms the additivity of the molecule and metal tip contributions, showing that, in all three dimensions, the Cu–CO tip's E_z calculated with DFT shares the same quantitative and qualitative behavior as the 0.7 D + CO molecule's field.

A qualitative description of the metal–CO tip is helpful for interpreting AFM images. The electric field of the Cu–CO tip (fig. 3.12(b)–(c)) retains the shape of the CO's electric field (fig. 3.8) close to the apex. The electron cloud of the

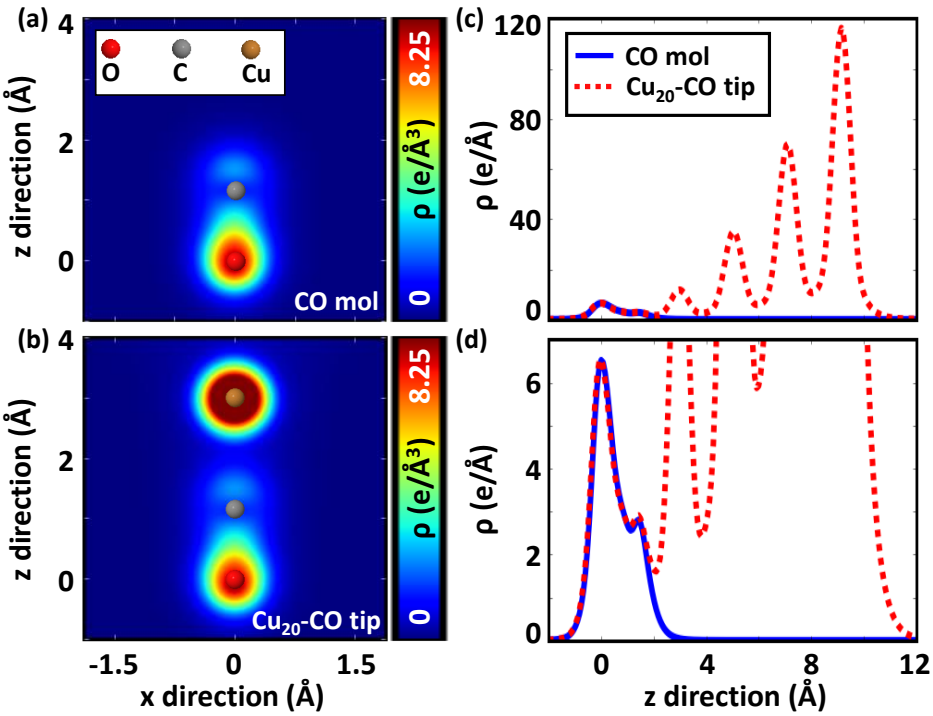

Figure 3.11: Charge density of (a) an isolated CO molecule and (b) a Cu_{20}–CO tip on a plane passing through the last Cu atom and the CO molecule. (c) Integrated charge density (xy–average) along the axial line of the CO molecule and (d) a zoom of (c). The Cu atom of the tip apex, the C atom, and the O atom are located at z=3 Å, z=1.15 Å, and z=0 Å respectively.

oxygen's lone pair creates a dome-shape electric field near the apex. The Cu tip reduces the strength and extent of the negative dome by surrounding it with a positive electric field.

Although these results are for an isolated metallic cluster, there are no qualitative changes when a slab is attached to the base of the cluster.

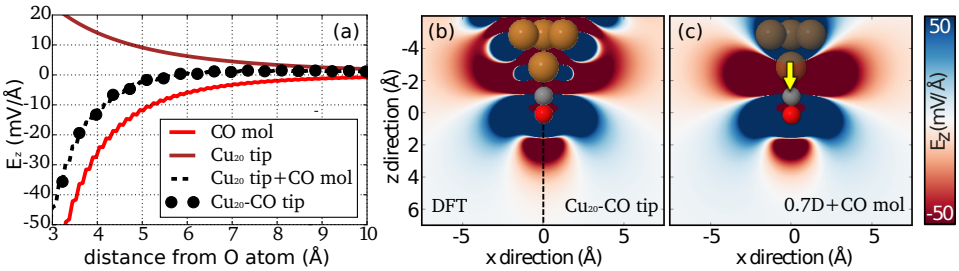

Figure 3.12: (a) The z-component of the electric field (E_z) along the axial symmetry line of a CO molecule (red line), a Cu_{20} tip (brown line), the addition of both fields (dashed black line), and the field from the compound Cu_{20}–CO tip (black markers). Full 3D field of (b) a Cu_{20}–CO tip and (c) a 0.7 D dipole and a CO molecule.

3.6 Validation of the E–field of metal–CO tips: Cl vacancy on NaCl

3.6.1 Experimental results

We proceed to discuss experimental NC–AFM images of a Cl vacancy on a NaCl bilayer on Cu(111). The Cl vacancy can be unambiguously identified by atomically resolved STM [243, 246] and AFM images [247], by Kelvin Probe Force Microscopy (KPFM) [60] and also by its characteristic features in STS [243]. In our case, images were gathered with a small amplitude AFM with a Cu–CO functionalized tip.

Fig. 3.13 shows the experimental AFM raw data of a Cl vacancy acquired with a CO tip as a function of tip–sample distance. The distance was varied by nearly 0.9 nm, and the tip height corresponding to the closest approach defined the reference height $z = 0$. From the data, four distinctly different distance regimes can be distinguished, each leading to specific contrast. For large tip heights ($z \sim 900 - 400$ pm) (figs. 3.13(a)–(c)), only the vacancy can be resolved as a faint and broad feature of less negative frequency shift. For $z \sim 400 - 200$ pm (figs. 3.13(d)–(f)), atomic corrugation on the ionic lattice gradually emerges, with the Cl^- (Na^+) lattice sites leading to less (more) negative frequency shift. The vacancy site remains the feature of least negative

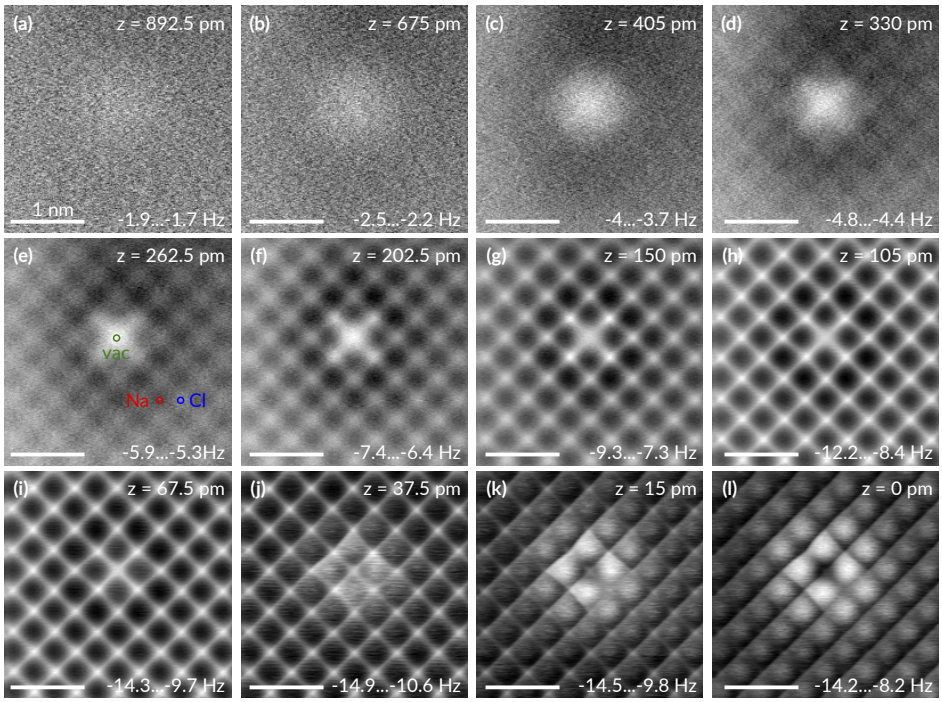

Figure 3.13: Experimental CH–AFM measurements of a Cl vacancy in bilayer NaCl on Cu(111) acquired with a CO tip. The tip height z, indicated in the top right, decreases from (a) to (l). $z = 0$ is defined as the distance at closest approach, corresponding to the data shown in (l). The frequency shift limits corresponding to black (more negative) and white are indicated in the bottom right of each panel. The positions of the vacancy site (vac, green), the Na site (Na, red), and the Cl site (Cl, blue) are indicated in panel (e). Scale bars correspond to 1 nm.

frequency shift but the contrast compared to the surrounding Cl sites decreases with tip approach until it disappears at $z \sim 200$ pm. For smaller tip–sample distances, sharp bright ridges arise (figs. 3.13(g)–(j)) connecting neighboring Cl sites and also the vacancy site with its four neighboring Cl sites. Finally, for tip heights below $z \sim 20$ pm, (figs. 3.13(k)–(l)), the atomic contrast reverses, both on the ionic lattice and the vacancy. The vacancy becomes the darkest site (most negative frequency shift) while the Na sites are now the brightest features

(least negative frequency shift), separated by a sharp, dark Cl grid.

3.6.2 Simulation results

The method described in sec. 3.2.3 was applied to a single Cl vacancy on a 6×6 surface unit cell (see fig. 3.5) using a slab composed of a NaCl(100) bilayer and 2 Cu(100) layers and a large vacuum region (total cell size 33.7 Å$\times 33.7$ Å$\times 49$ Å). We model the CO functionalized Cu metallic tip by using the full charge density of the CO molecule and a 1.5 D dipole to simulate the metallic tip (in sec. 3.6.3 we will explain the choice of the metallic tip dipole). Fig. 3.14 shows calculated images for a range of tip heights z_T –defined as the distance of the O atom of the tip to the topmost atomic NaCl layer– corresponding to those in fig. 3.13. We obtained excellent quantitative agreement with the experiment, reproducing the contrast at every site (vacancy, Na and Cl atoms close and far from the vacancy) and the contrast changes as a function of tip height. By comparison to the experiment, we can relate the experimental height scale z to the absolute tip–sample distances z_T with an offset of 300 pm: $z = z_T - 300$ pm.

Contrast changes with tip height arise from the variation of the relative weight of the SR, ES, and vdW contributions to the total tip–sample interaction. Fig. 3.15 illustrates the distance dependence of these contributions with frequency shift curves on the Na, Cl, and vacancy sites (marked in fig. 3.15(e)), and 2D force maps at two characteristic tip–surface distances. The ES force dominates the image contrast for tip heights z_T above 500 pm. Fig. 3.15(b) shows that the ES contribution to the Δf contrast (frequency shift differences among sites) remains larger than the SR one for tip heights larger than 450 pm. This change in the frequency shift contrast is responsible for the contrast change in the images observed at 500 pm in fig. 3.14, as the frequency shift is proportional to the derivative of forces. The ES interaction is responsible for the bright (less attractive) broad feature associated with the positively charged vacancy at large tip heights, and for the atomic contrast that emerges in the medium tip height regime ($z_T \sim 700 - 500$ pm). In this distance range, the positive Na sites show a larger negative frequency shift (i.e. a more attractive interaction) than the negative Cl sites, while the positive vacancy site remains the least attractive

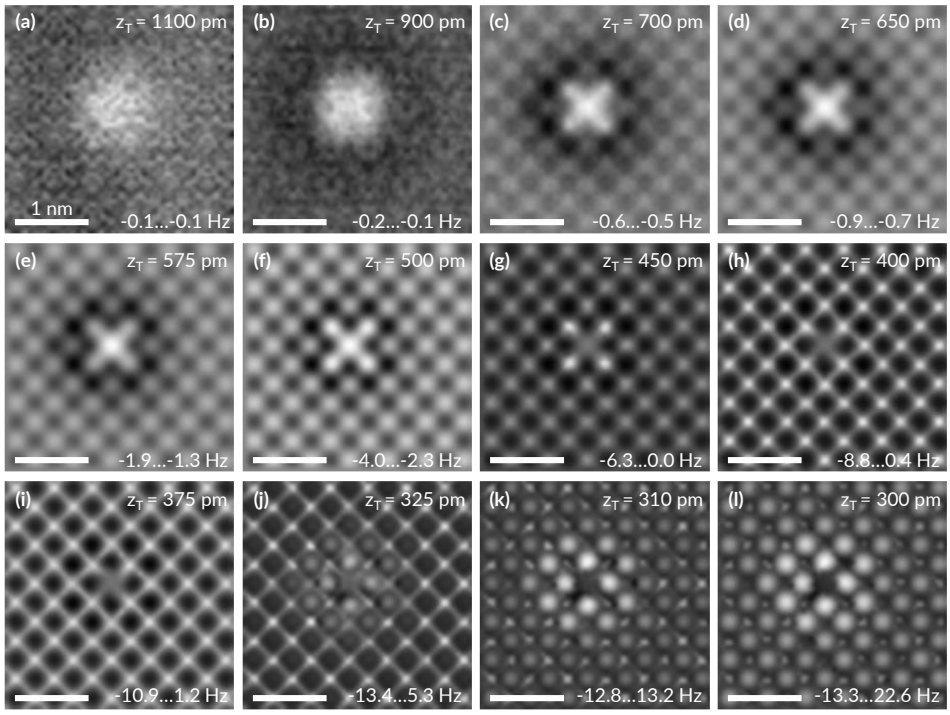

Figure 3.14: Theoretical AFM images of a Cl vacancy in bilayer NaCl on Cu(100) using a CO probe and a 1.5 D dipole simulating a Cu tip. The tip height z_T, indicated in the top right, decreases from (a) to (l). The frequency shift limits corresponding to black (more negative) and white are indicated in the bottom right of each panel. Scale bars correspond to 1 nm.

site (igs. 3.15(b) and (d)). Thus, the tip apparently exhibits the behavior of a negative dipole on Na/Cl, but that of a positive dipole on the vacancy site, highlighting the limitations of the common dipole approximation to describe the electric field created by the tip.

For small tip heights ($z_T < 500$ pm), the SR interaction becomes the most important contribution to the contrast due to the exponential growth of the Pauli repulsion above the Cl sites (fig. 3.15(b)). This is best shown in fig. 3.16 where 4 sets of force decomposed images as well as tip relaxation for probe-sample distances $z_T = 1000$ pm, 650 pm, 400 pm, 375 pm, and 300 pm are plotted. Forces are decomposed in terms of SR, ES, and vdW contributions.

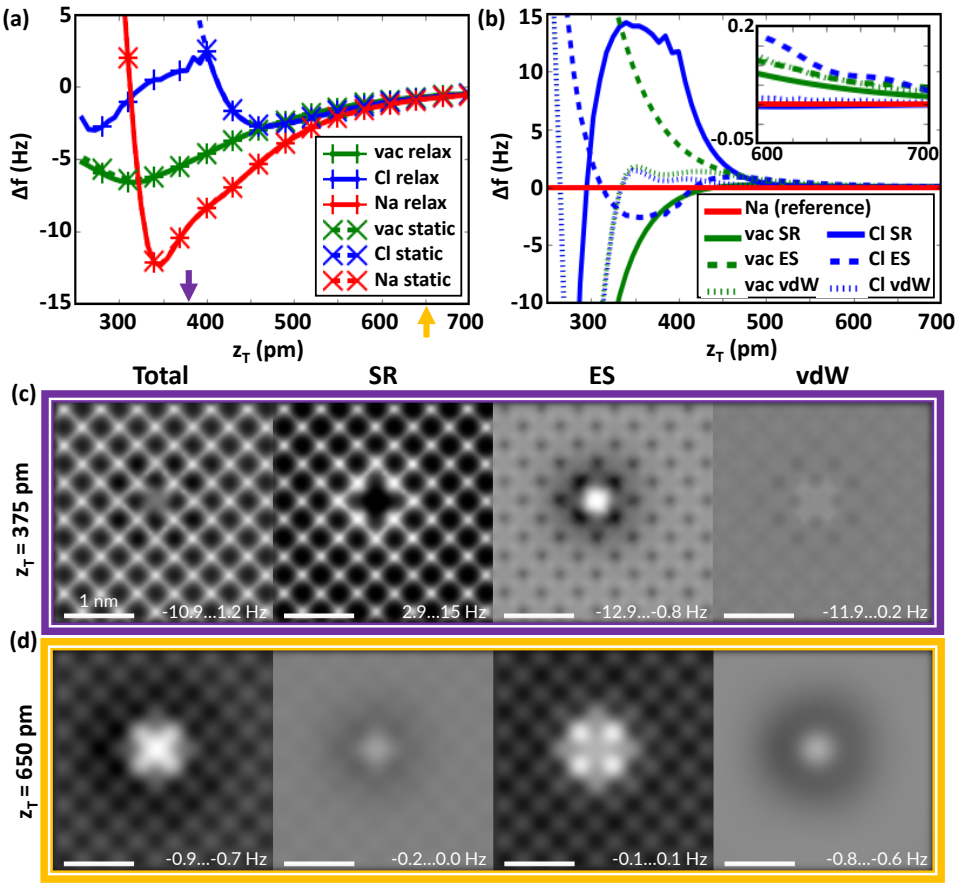

Figure 3.15: a) Total frequency shift with (solid) and without (dashed lines) relaxation of the CO probe for the vacancy (green), Cl (blue), and Na (red) sites. b) Frequency shift decomposed spectroscopy for the above sites in terms of the SR (solid), ES (dashed), and vdW (dotted lines) interaction. Δf decomposed images in terms of the above mentioned interactions for c) $z_T = 375$ pm and d) $z_T = 650$ pm. In order to highlight the influence of each contribution on the total frequency shift, the frequency shift limits are scaled to keep the frequency shift range in all contributions equal to the total frequency shift range.

Images in the bottom row illustrate the tilting of the CO probe. The lines show trajectories of the O atom when the tip is scanned along a rectangular grid. At $z_T \sim 400 - 375$ pm, the CO molecule starts to tilt to avoid the high repulsion over the Cl anions, as shown by the difference between the static and relaxed

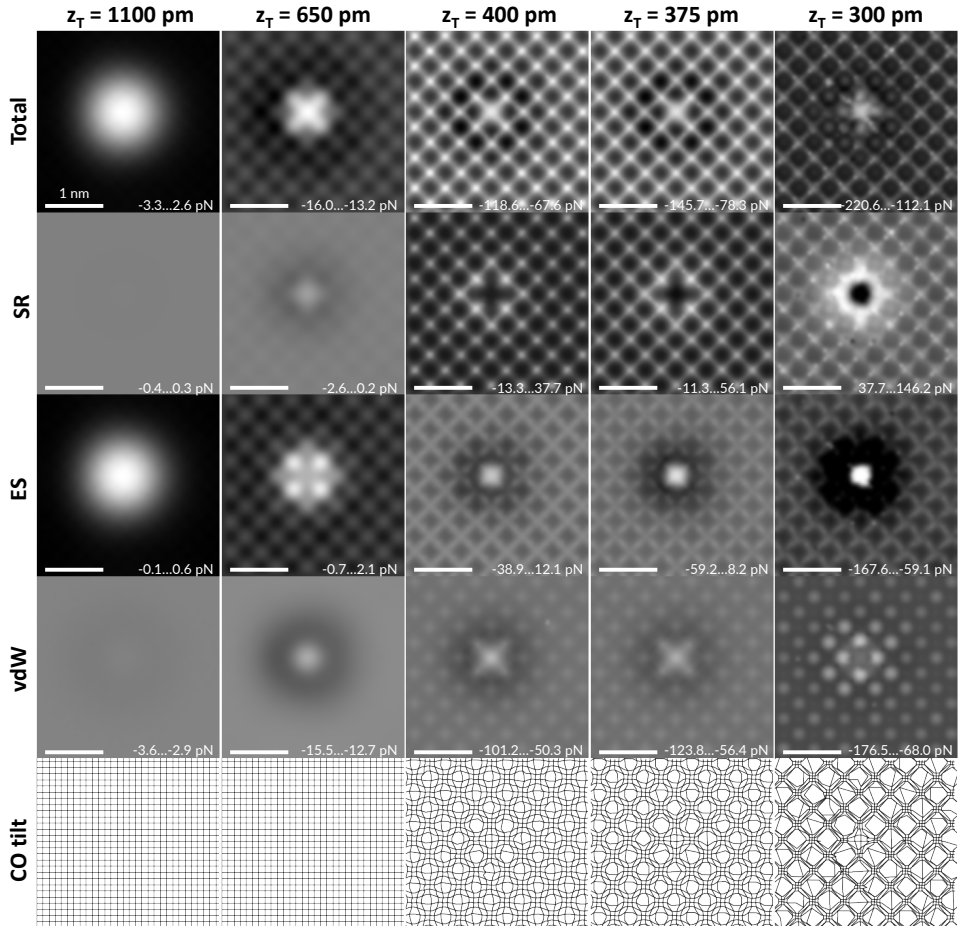

Figure 3.16: Total force and force decomposed images in terms of SR, ES, and vdW interactions contributions for z_T = 1000 pm, 650 pm, 400 pm, 375 pm, and 300 pm. In order to highlight the influence of each contribution on the total force, the gray scale in all of the images corresponds to the variation range of the total force and the numbers at the bottom right of each image indicate the minimum and maximum values of the interaction. The bottom row represents the CO tilt. The lines show trajectories of the O atom when the tip is scanned along a rectangular grid (only half of the grid points used to construct the images are shown). Notice that the probe relaxes toward the Na site (low electronic density) and is more pronounced as the tip height distance decreases.

curves in fig. 3.15(a), and the relaxation maps in fig. 3.16. Notice that, in this distance range, the Na/Cl contrast from the ES contribution is much smaller compared to the SR. However, on the vacancy site, due to the small electron density, the Pauli repulsion is negligible and the ES interaction remains dominant. Upon further approach, the CO probe increases its tilting toward the minima of the PES (fig. 3.16), and by doing so, the saddle line between two neighboring Cl ions (and the vacancy and its neighboring Cl ions) is sharpened [119, 160]. For the smallest tip heights explored ($z_T \sim$ 310–300 pm), the Na sites become brighter than the Cl sites (see fig. 3.14). This contrast inversion is explained by the change of the slope of the force on the Na sites as it reaches its minimum at $z_T \sim 310$ pm (see fig. 3.15(a)). At this tip height, the force still increases with decreasing tip height both on the Cl sites (due to the tip tilting towards the Na atoms) and on the vacancy (due to the small Pauli repulsion).

3.6.3 Determination of the dipole that describes the metal tip in the experiment

In sec. 3.4, we showed that replacing the Cu metal tip by a 0.7 D dipole is a good approximation for the E_z of Cu–CO tips calculated with DFT. However, for the Cl vacancy on the NaCl bilayer, such a small dipole underestimates the ES tip–sample interaction and does not reproduce the experimental contrast of the vacancy at large probe-sample distances, where it appears brighter than the surrounding Cl sites (see figs. 3.13(a)–(e)). This is true both for calculations performed with our model as well as for DFT force calculations of this surface probed by Cu–CO tips.

The choice of dipole size necessary to reproduce the experimental contrast is difficult. We have selected the smallest dipole needed to reproduce the contrast inversion near the vacancy around $z_T = 500$ pm (figs. 3.13(e)–(g)). While the vacancy is brighter than the adjacent Cl sites in fig. 3.13(e), they are imaged with similar frequency shift in fig. 3.13(f), and, finally, the Cl ions become brighter in fig. 3.13(g). In order to pin-point the desired dipole strength, a CH profile at $z_T = 500$ pm is computed in the vicinity of the vacancy and for different dipole sizes (fig. 3.17(a)). The difference in frequency shift between the Cl site and

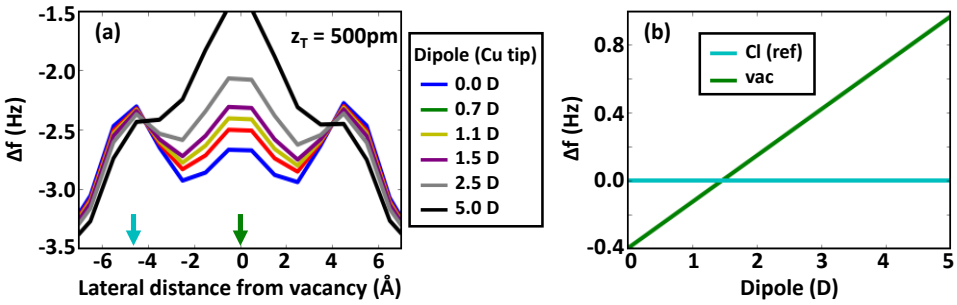

Figure 3.17: Constant-height profiles across the vacancy site using the CO probe and 0 D, 0.7 D, 1.1 D, 1.5 D, 2.5 D, and 5 D dipoles as a Cu tip. Profiles were calculated along the diagonal (following the X shape feature) at z_T = 500 pm. b) Difference in frequency shift between the vacancy site and Cl ions adjacent to vacancy. A 1.5 D dipole is roughly the minimum dipole size needed to image these two sites with equal frequency shift.

vacancy site as a function of dipole can be extracted from the CH simulation (fig. 3.17(b)). The model reproduces the experimental observation described above with a dipole of roughly 1.5 D, approximately twice the value calculated from DFT. Note that, as described previously, the dipole is centered 53 pm away from the metal tip apex (in the direction of the surface) because it provides the best fit to the ES potential. In order to reproduce the experimental contrast with a dipole placed at the tip apex, a ≈ 2.0 D dipole would be needed.

Admittedly, larger dipoles seem to reproduce better the experimental contrast for large probe-sample distances ($z_T > 700$ pm). This is illustrated in fig. 3.18 where AFM images for the far distance regime are simulated using different dipoles. It is not clear if this discrepancy between the calculated and the effective dipole moment, which is necessary to reproduce the experiments, reflects the limitations of a pure, perfectly ordered Cu tip to represent the real metal tip structure, an incorrect description of the charge density around the vacancy by the PBE [209] XC functional, or it arises from a failure in the description of other interactions.

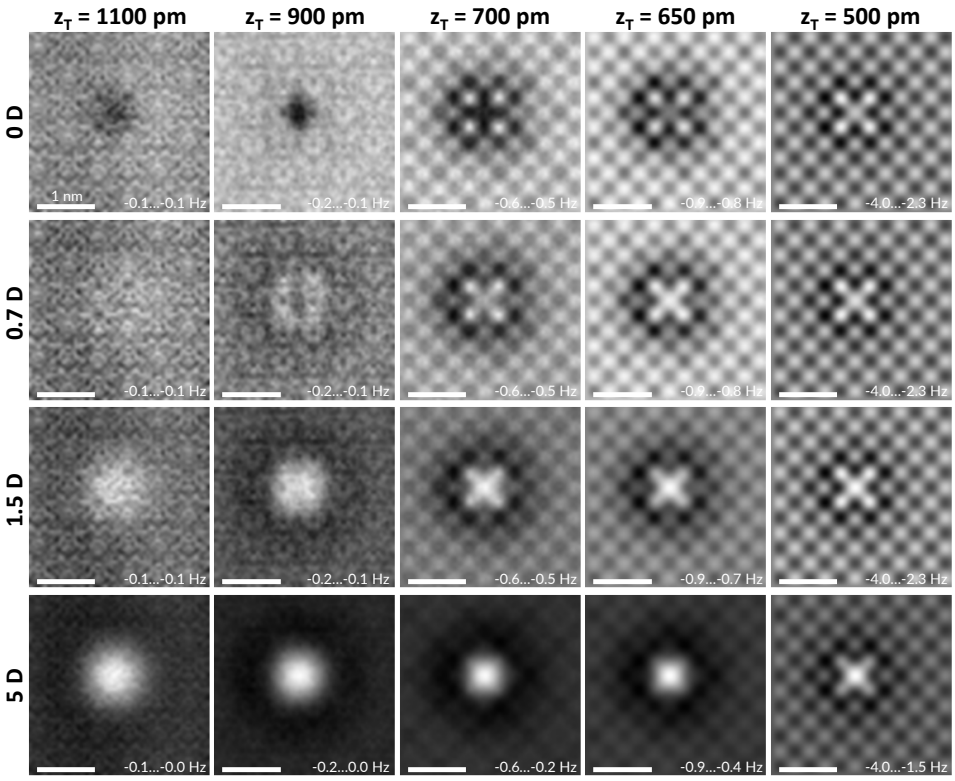

Figure 3.18: Theoretical AFM images of a Cl vacancy in bilayer NaCl on Cu(100) using a CO probe and dipoles of 0, 0.7, 1.5, and 5 D acting as a Cu tip. The probe-sample distance, z_T, decreases from 1100 to 500 pm. The frequency shift limits corresponding to black (more negative) and white are indicated in the bottom right of each panel. Scale bars correspond to 1 nm.

3.6.4 Interplay Between CO and Metallic Tip ES Interactions

We are now in the position to discuss how the interplay of the electric field created separately by the CO and the positive dipole replacing the metal tip explains the observed contrast for the large and medium tip height regime ($z_T > 500$ pm). In consistence with literature, our DFT calculations predict that the total charge distribution of the isolated CO molecule shows a small dipole of 0.12 D, with its positive pole at the oxygen. However, as discussed in sec. 3.3, the electric field of the molecule is quite complex and can only be replaced by

the one created by this small dipole for very large tip–sample distances. For the closer distances relevant for AFM imaging, the field is ruled by the local charge distribution. Ahead of the oxygen atom, the electric field is effectively produced by a localized negatively charged cloud in front of this atom neutralized by a positive charge in the nucleus. This charge distribution arises from the asymmetry in the electronic charge density induced by the oxygen lone pair. In the near field, the resulting electric field resembles the one created by a negative dipole placed at the oxygen atom. Thus, the combined ES field of the CO probe and the metal tip can be represented by two opposing dipoles.

The relevant question is, what role do these opposing dipoles play in the contrast formation? Fig. 3.19(a) shows the contribution to the ES interaction of the Cu metal (1.5 D dipole), CO probe, and the compound 1.5 D–CO tip on the vacancy (green), Cl (blue), and Na (red) sites. The greatest difference between the ES interactions of the CO probe and the compound 1.5 D–CO tip is obtained on the vacancy site (solid versus dashed lines). At far distances, the 1.5 D dipole that simulates the metallic tip only probes electrostatically extended sites such as the vacancy. Furthermore, as discussed previously, at close probe-sample distances, the SR interaction is the dominant contribution on the contrast formation. Thus, the dipole only contributes to the contrast of the vacancy site with respect to the Cl/Na sites. On the contrary, the very localized electric field of the CO probe is the one responsible for the atomic resolution of the NaCl lattice. These conclusions are clearly illustrated in figs.3.19(b)–(d) that show images of the ES interaction at $z_T = 650$ pm using the CO probe, a 1.5 D dipole, and the composite 1.5 D–CO probe.

Fig. 3.20 provides an explanation for this behavior in terms of the lateral extension, 650 pm away from the probe, of the E_z of a) the CO probe, and b) the Cu apex (1.5 D dipole). The electric field of the metal apex extends over several lattice positions while the CO's is localized to a single atomic position. Effectively, the metal apex averages the periodic Cl^-/Na^+ charges. However, near the vacancy, the metal apex is able to probe the extended vacancy's net positive charge.

In summary, for the uncompensated positive charge of the vacancy, both

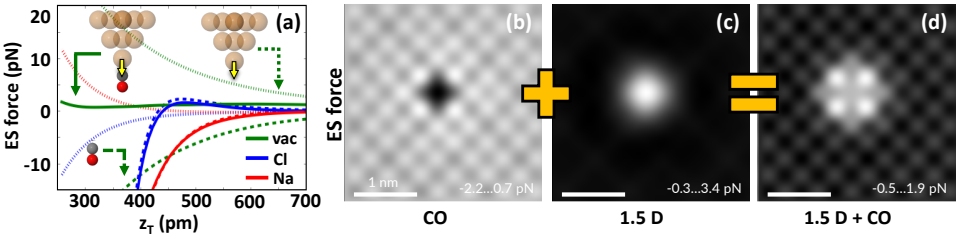

Figure 3.19: (a) ES interaction of the isolated CO probe (dashed), a 1.5 D dipole simulating the metallic tip (dotted), and the CO- 1.5 D probe (solid lines) for the vacancy (green), Cl (blue), and Na (red lines) sites. ES interaction image using (b) isolated CO probe, (c) a 1.5 D dipole acting as a Cu tip, and (d) the composite CO+1.5 D probe at $z_T = 650$ pm.

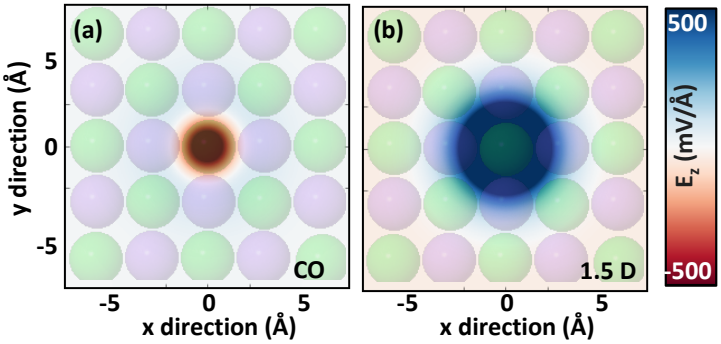

Figure 3.20: Lateral distribution of the E_z of a) the CO probe and b) the 1.5 D dipole (that replaces the Cu tip charge distribution) in the NaCl top surface plane. The composite CO+1.5 D probe is at $z_T = 650$ pm (as in fig. 3.19). The atomic positions of the Cl vacancy on NaCl surface are superimposed. The electric field of the metal tip in (a) extends over several lattice sites and effectively averages out the opposite contributions of Na^+ and Cl^- ions to the ES interactions. The field of the CO molecule in (b), confined to a single atomic position, is responsible for the atomic-scale lattice resolution.

dipoles contribute and compensate each other but the larger positive dipole dominates, leading to a repulsion above the vacancy site, already observable at large tip heights (fig.3.19). However, in the case of the atomic Na and Cl sites, the rather different spatial extension of the electric fields (see fig.3.20)

leads to a completely different scenario. The dipole coming from the metal apex cannot resolve those sites because its field spreads out significantly at the sample surface, effectively averaging their opposite contribution. On the contrary, the smaller but rather localized electric field created by the CO molecule is crucial for explaining the observed atomic resolution.

3.6.5 Can a Single Dipole Mimic a CO Molecule on a Tip?

The main messages that should be extracted from the previous analysis is that the ES behavior of the metal–CO tips is complex. The metallic tip produces a field that is attractive towards electrons and can be modeled by a positive dipole (partial positive charge at the apex). On the other hand, the CO molecule has a net positive dipole but this is only relevant in the very far field where the dipolar approximation reproduces the electric field. Close to the O, the electric field is localized and repulsive towards electrons. The question we address now is, could a dipole quantitatively reproduce the HR–AFM images obtained using the 3D ES potential of the CO molecule?

For tip–sample distance relevant for AFM ($z < 1100$ pm as seen in Fig 3.13 and fig. 3.15), the ES potential of the CO molecule is repulsive towards electrons. Thus we attempt to substitute the 3D potential of the CO molecule by the one produced by a negative dipole. For the distance range $z = 1100 - 650$ pm, we find that a dipole of -0.4 D quantitatively reproduces the AFM images calculated with the full 3D potential (see fig. 3.21 for the comparison). For smaller distances the ES field of the CO molecule stops having a behavior that can be modeled by a dipole over a large enough range of distances. In addition, even for a qualitative description of AFM images, tilting effects and inhomogeneous sample charge distributions invalidate a dipole substitution. For this reason, we strongly discourage modeling the CO molecule by a single dipole, and, instead, favor the use of the whole charge density of the CO molecule.

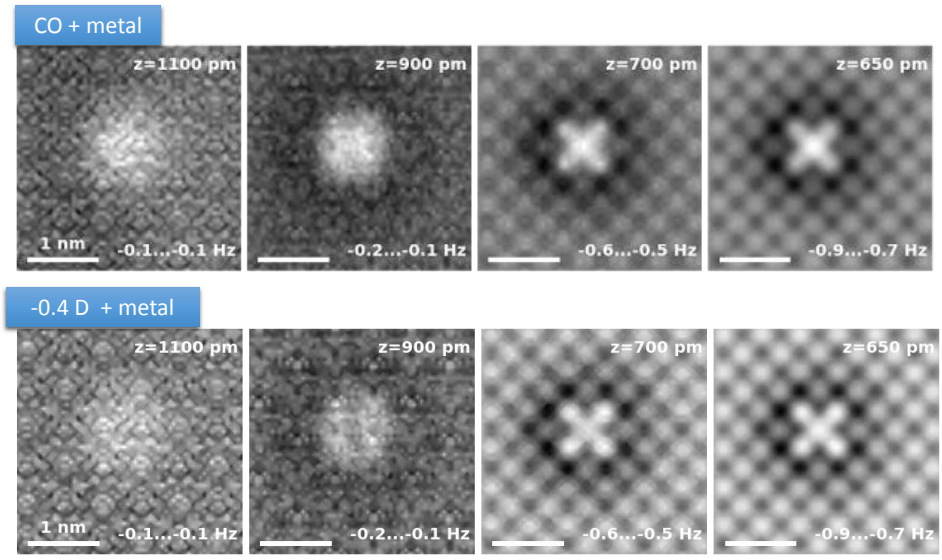

Figure 3.21: Theoretical AFM images of a Cl vacancy in bilayer NaCl on Cu(100) using a CO probe and a 1.5 D dipole simulating a Cu tip. In the top row, the full CO charge distribution is used to model the CO part of the ES interaction and in the bottom row, the CO is replaced by a -0.4 D dipole. The frequency shift limits corresponding to black (more negative) and white are indicated in the bottom right of each panel. Scale bars correspond to 1 nm.

3.7 AFM imaging of the CO molecule as an adsorbate

Carbon monoxide surface adsorption has been a central point in the study of surface science. It has been widely studied with ensemble averaging techniques [251], as well as scanning probe techniques. For the NC–AFM, it is an especially important problem due to the use of the CO molecule for tip functionalization [40].

We have already characterized the ES behavior of a metal–CO tip. The metallic tip acts as a positive dipole and, for distances relevant for AFM, the charge density of the CO is repulsive towards electrons. In principle, we would expect the CO adsorbed on a metal surface to display the same behavior, and, thus, the interpretation of NC–AFM images taken with a metallic tip to be straightforward. However, the NC–AFM studies of the surface adsorption of the

CO molecule found in the literature propose rather different interpretations. In most of the cases, the CO appears as an attractive feature [232, 241, 250, 252, 253], presumably due to the vdW interaction. Contrary to this, two studies have reported imaging the CO adsorption on Cu(111), NiO(001), and Mn/W(001) both in the attractive and repulsive regimes [64, 239]. In these studies, an attractive hump–like feature of 1 nm is observed for far tip–sample distances, while a repulsive donut-like feature appears at smaller distances.

There are two contradictory explanations for the contrast observed for the adsorbed CO in the repulsive regime using metallic tips. Schwarz *et al.* [239] propose a model in which the vdW interaction, modeled by a radially dependent attractive potential, competes with a repulsive dipole–dipole ES interaction (which has both radial and angular dependence). This interaction arises from two antiparallel dipoles: the net positive dipole of the adsorbed CO molecule (+0.3 D for CO/Cu(111)), and the positive dipole of metallic tips (+1.5 D for Cu tips) [64, 239]. By assuming a larger interaction radius for the vdW interaction as compared to the interaction radius of the dipole-dipole interaction, a repulsive donut-like regime can be obtained with the model at a tip–sample distance (as measured by the tip apex and O atom separation) of > 4.5 Å.

On a closer look, several issues arise with this model: (1) The contrast change is inverted. That is, the attractive hump–like feature is predicted for smaller tip–sample distances than the donut-like repulsive feature. (2) Both frequency shift and energy difference between the CO molecule and background substrate are more than an order of magnitude smaller than what is observed experimentally. (3) As we will see briefly, at $z > 4.5$ Å the ES potential of the adsorbed CO on metal surfaces is repulsive towards electrons. The tip–sample distances at which the repulsive feature occurs are much larger than what is observed experimentally. When the CO is adsorbed on the Mn/W(001), the repulsive feature is imaged ≈ 2 Å higher than the minimum frequency shift of the substrate background [239]. Using an adsorption distance for the CO molecule of 2 Å the relative distance between the tip and the O atom is ≈ 2 Å.

We propose an alternative explanation based on the SR repulsion due to the overlap of the tip and sample wave functions. We have carefully examined

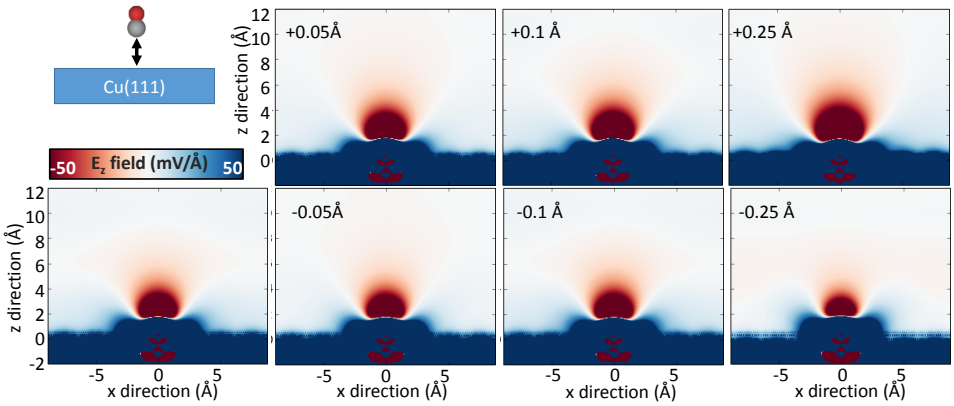

Figure 3.22: z-component of E–field of CO on Cu(111) for various adsorption distances. On the first row the CO molecule is placed at the equilibrium adsorption distance. In the subsequent rows the molecule is displaced vertically.

the ES behavior of the sample with DFT calculations (see appendix 3.2.2 for details). The first column of fig. 3.22 shows the electric field with the molecule adsorbed on a top site at the distance predicted by DFT. In line with what we have shown for the Cu–CO tips, close to the CO, the field resembles the field of the isolated CO molecule. Above the O atom, it is repulsive towards electrons, even past 10 Å. As in the case of the isolated molecule, the overall dipole of the system is positive and indeed, at very far distances, there would be a contrast inversion of the field. The dipole actually increases with respect to the isolated molecule, from +0.1 D to +0.3 D. The increment was obtained by calculating the change in the work function of the sample

$$\text{dipole} = \frac{\epsilon_0 \text{Area} \Delta W}{e}. \tag{3.6}$$

It is worth noting that the CO/metal system is challenging for DFT. Experimental evidence clearly shows that the CO molecule adsorbs onto a Cu substrate on a top site [254]. However, DFT favors, even with the most sophisticated XC functionals, sites with a higher coordination. This classic problem, common to many FCC metals, has been traced back to the limitations of DFT in the description of the subtle energy differences among the triple, double, and single bond configurations of the CO molecule. In the particular case of Cu, DFT

predicts the top site to be the stable adsorption configuration, but the energy difference between top and hollow adsorption sites is almost negligible.

Given the possible limitations of DFT, we have explored the robustness of the ES properties of the system by varying the adsorption distance of the molecule. The panels in fig. 3.22 display the electric field for different cases where the adsorption distance is varied in ± 0.05 Å increments. These results clearly show that there are no qualitative changes in the behavior of the electric field. Furthermore, the field is also robust against changes in the CO adsorption site (hollow and bridge).

From the above analysis, it is clear that the ES interaction between the CO/Cu(111) sample and a metallic tip is attractive for tip–sample distances below 10 Å. As discussed for the isolated CO molecule, there would be a contrast inversion for very large distances, but the resulting interaction is negligible and certainly not relevant to represent the experimental measurements. This leaves chemical repulsion as the only source for the repulsive features observed in the experiments. However, the repulsive features have only been observed in constant interaction maps, where the slopes of the frequency shift are always positive [239], and the Pauli repulsion led to very strong repulsive forces. Without ionic relaxations, the change of contrast between the hump–like attractive regime and the donut-like repulsive regime would occur at negative slopes. For this reason, ionic relaxation needs to be included in the explanation of the contrast formation.

In order to further understand the AFM contrast mechanism for the imaging of CO adsorbed on metallic surfaces with metallic tips, we have carried out DFT force vs distance calculations (see appendix 3.2.2 for details of the calculations). As a model system, we use CO adsorption on a Cu(111) substrate as probed with a Cr_{14} tip (3 layer pyramid carved from a Cr(110) surface) that mimics the tip used in the experiments [239]. Fig. 3.23(a) shows the force on top of a Cu atom (blue line) and the CO molecule in an upright position and without ionic relaxation (green line). The tip–sample distance (z_T) refers to the height between the tip apex and the O atom with the CO molecule in an upright position. The interaction on top of the CO molecule is attractive at large

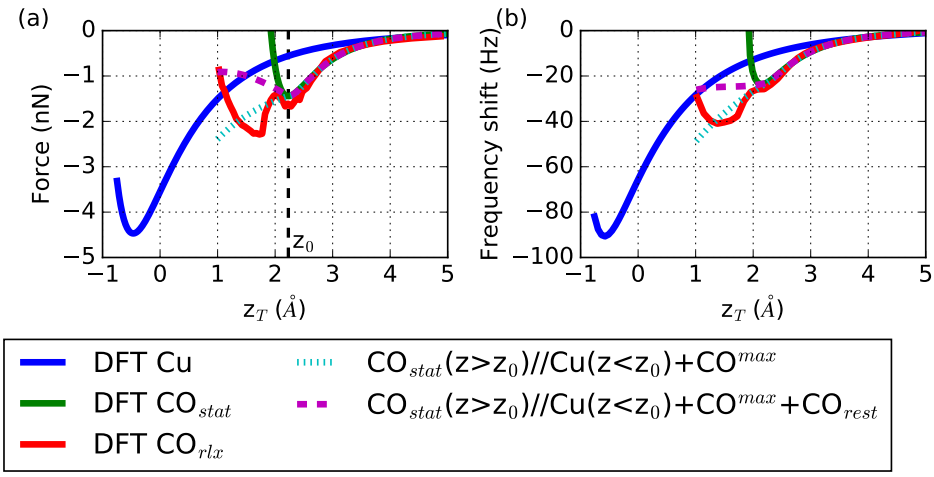

Figure 3.23: Theoretical (a) force and (b) frequency shift versus distance plots of the adsorbed CO on Cu(111) surface as probed by a Cr_{14} tip. DFT calculations of a top site of the Cu(111) (blue lines), the adsorbed CO molecule in an upright position without relaxation (green lines), and the adsorbed CO molecule with ionic relaxation (red markers). Simulated AFM spectroscopies with (purple dashed lines) and without (cyan dotted lines) a CO tilt restoring force. The tip–sample distance corresponds to the height between the metal apex atom and the O atom with the CO in an upright position.

tip–sample distances and due to Pauli interaction becomes repulsive at smaller heights, with the minimum force occurring at $z_T = z_0 = 2.2$ Å. The interaction on top of a Cu atom has the same behavior but with the minimum force occurring at $z_T = -1.5$ Å(or 1.5 Å with respect to the Cu substrate). The distance between the minimum forces roughly corresponds to the CO adsorption distance on the Cu substrate (3 Å from the O atom). Although the Cu site is overall more reactive (it has a minimum force of -4.4 nN compared to -1.4 nN for the CO site), the CO is more attractive for $z_T > 2.0$ Å. From this we can conclude that the change of contrast in AFM images occurs at most 2.5 Å from the maximum interaction (minimum force) measured at the background substrate. This is a key point that is supported by experimental findings [239] and yet not consistent with the dipole-dipole model described above.

A further corroboration is done by calculating the frequency shift. Fig. 3.23(b) shows the frequency shift calculated using the large amplitude oscillation approximation,

$$\Delta f = \frac{f_0}{kA^{3/2}} \frac{1}{\sqrt{2\pi}} \int_0^\infty \frac{F_{ts}[d+z']}{\sqrt{z'}} \mathrm{d}z', \tag{3.7}$$

with a typical experimental prefactor of the integral of -16.82 Hz/nN/Å$^{1/2}$. As in the force plot, the CO is more attractive (less negative frequency shift) for large tip–sample distances, and there is a contrast inversion at around 2 Å (this is approximately 2.5 Å from the minimum frequency shift of the substrate). Due to the exponential increment of the Pauli repulsion, the crossing between the CO and Cu frequency shift occurs after the CO's slope change (negative slope). As discussed before, in the experimental images the crossing is observed at positive slope frequency shifts. This can be accounted for by taking into account ionic relaxations. The CO, being fairly mobile on the substrate, has the ability to tilt or even hop between adsorption sites (top, hollow, bridge). This reduces the overlap of the molecule and apex wavefunctions and thus attenuates the repulsion.

The adsorption of the CO atom on a Cu(111) surface is not a trivial problem. As stated before, DFT does not predict a sufficiently large barrier between the adsorption of the CO on a top site versus hollow site with the commonly used XC functionals. This makes the interpretation of AFM calculations that include ionic relaxation somewhat problematic; nonetheless, they are instructive. Red lines on fig. 3.23(a) shows force versus distance DFT calculation on top of the CO molecule that include ionic relaxation. Up to the maximum interaction (z_0), the ionic relaxations are negligible and the forces are similar to the static ones. For smaller tip–sample distance, the CO molecule avoids the high repulsion caused by the proximity of the tip by two mechanisms. Close to z_0 the molecule starts to tilt and slightly increases the force, yet suppressing the exponential repulsion felt by the molecule fixed in the upright position. As the distance is further reduced, the molecule starts to shift to the hollow position causing a drop of force of 1 nN. Before the CO fully reaches the hollow position (the C atom remains closer to the original Cu atom than the neighboring ones), the CO starts to tilt again and the force increases non-exponentially. The shift towards

the hollow site is a reversible process (upon tip retraction the CO returns to the top position), which makes the described dynamics experimentally plausible. Alternatively, a larger top/hollow barrier prolongs the initial CO tilt regime.

In order to fix the limitations of DFT, we have introduced a simple model to account for a large top/hollow barrier that enforces the CO to tilt upon tip approach. It is based on two suppositions: (1) through the CO tilt, the tip retains the maximum interaction with the CO (experienced at z_0) and only gains interaction through the substrate. (2) The tilt carries a penalization cost proportional to the tip–sample distance. The resulting interaction,

$$F[z] = \Theta(z - z_0)\mathrm{CO}_{\mathrm{stat}}[z] + \Theta(z_0 - z)\left[\mathrm{Cu}[z] + \mathrm{CO}_{\mathrm{max}} - k_{\mathrm{rest}}(z - z_0)\right], \quad (3.8)$$

is plotted in fig. 3.23 as purple dashed lines (and cyan dotted lines without the restoring force). A spring constant of $k_{\mathrm{rest}} = -1.5$ nN/Å was used in order to simulate the positive–slope–frequency–shift–crossing closest to z_0 (see fig. 3.23(b)). The contrast inversion occurs at $z = 1$ Å, this is 1.5 Å away from the minimum frequency shift of the substrate. Also, 2 Å higher than the crossing ($z_T = 3$ Å), the contrast between the CO and the background is approximately 0.5 Å. This is also supported by experimental findings [239] and is inconsistent with the dipole-dipole model.

A final point of clarification. The above analysis was done on the model CO-Cu(111) system. Due to the large screening of metallic surfaces, we expect the analysis to be applicable to other metallic substrates. However, it may not apply to non-metallic substrates such as NiO [64], where ionic relaxations of the substrate and spin polarization play an important role in the chemisorption of the CO molecule and can induce relevant charge transfers resulting in a completely different ES potential of the sample.

3.8 Conclusions

This chapter has explored the electric field created by CO functionalized metal tips. Our analysis conclusively shows that this field cannot be described by a single dipole. It is necessary to take into account both the positive dipole that describes the electric field created by the metal tip and the negative charge

cloud strongly localized in front of the oxygen atom. We have incorporated this insight into a theoretical model that facilitates the efficient simulation of AFM measurements retaining a first-principles accuracy. Using this model, we have identified the contrast formation mechanisms for AFM images of localized ionic defects (Cl vacancies on a metal–supported NaCl bilayer) using CO–decorated metal tips. The ES interaction dominates the contrast at large and medium tip–sample distances (> 500 pm), while Pauli repulsion takes over at closer separations, where the CO probe tilts and highlights saddle lines as ridges. The opposite sign and different spatial extension of the associated electric fields explain the rich contrast observed. While both terms compete to determine the contrast of uncompensated, extended defects like the Cl vacancy, atomic–scale resolution of the ionic lattice arises mainly from the CO electric field as the more extended field created by the metal apex averages out the contribution coming from those periodic and rapidly varying charge distributions.

The insight gained from our analysis can be used to address the apparent contradiction in the interpretation of previous experiments involving CO molecules either as a tip on a metallic apex probing ionic surfaces [232] or as an adsorbate probed with a pure metallic tip [239]. Our results show that the ES field of the CO tip is crucial to describe the AFM contrast on the atomic scale. We prove that the simplified description of the tip as a single dipole to explain the ES interactions fails. We show that the contradictory assignment of the CO dipoles' direction in recent publications [232, 239] is related to this approximation and provide a consistent interpretation for the images of CO adsorbates in the repulsive regime in terms of the Pauli repulsion.

We believe that our methodology for the calculation of AFM images including the detailed local charge distributions of the tip and sample obtained from first-principles calculations is the right tool to address two key open issues in HR–AFM: the origin of the inter–molecular contrast observed in hydrogen-bonded and metal–coordinated systems, and the enhanced resolution in KPFM measurements with metal–CO tips.

4 HR–AFM images on H–bonded molecular layers with CO decorated metal tips

In the previous chapter we explored the interplay of the SR, ES, and vdW interactions on the contrast formation of surfaces as probed by CO tips. For this purpose, we developed a methodology for simulating interaction–decomposed images with DFT accuracy that uses a description of the ES interaction based on the charge density of the tip and the potential of the sample.

In this chapter, we turn our attention to molecules. Several methods have been used to create theoretical HR images of molecules, including integrated charge densities, simple pair–wise potentials, and simulated tip tilt, but they all have limitations. Here, we use a model system of hydrogen–bonded monolayer of triazine molecules to uncover the contrast mechanism on both the intra– and inter–molecular features observed in HR–AFM. We also address issues related to previous simulations methods that highlight the importance of an appropriate treatment of the tip tilt and the strong cancellation between the SR and ES interactions.

4.1 Introduction

The contrast mechanisms for CO decorated metallic tips in HR images of molecules are nontrivial. Images are usually taken at close tip–sample distance where Pauli repulsion is the dominant interaction and the tip senses high charge density areas. The mobility of the CO molecule or other atom/molecule functionalized tips enhances the PES saddle lines and reveals bond–like inter–molecular features in images [127, 164, 189]. Similarly, it reveals inter–molecular features

associated with H–bonds [123]. However, the origins of these features are less well understood. On polar or ionic surfaces or charged molecules, the electrostatics of the tip can play an important role in enhancing the contrast formation. In the previous chapter, we showed that the potential of the CO–metal tip can be represented by the sum of a dipole potential that takes into account the positive charge accumulation of the metallic tip at the tip apex and the electrostatic potential of the isolated CO molecule, which exhibits a negative charge accumulation at the O atom due to its lone pair. While the field of the isolated CO molecule is always important for the contrast formation, the positve dipole of the metallic tip is only relevant for spatially extended non–neutral areas. On ionic surfaces, both terms compete to determine the contrast of uncompensated, extended defects like the Cl vacancy, atomic–scale resolution of the ionic lattice arises mainly from the CO electric field as the more extended field created by the metal apex averages out the contribution coming from those periodic and rapidly varying charge distributions.

Lastly, on molecules, the vdW provides an overall attractive background with negligibly atomic scale fluctuations [169].

Theoretical models have helped to rationalize the imaging mechanisms of HR–AFM imaging of molecules. Most importantly, DFT analysis identified the SR interaction, mainly Pauli repulsion, as the dominant interaction responsible for the imaging of molecular structures at small tip–sample distances [40, 186] and the role of the tip tilt on the sharpening of inter–molecular features [119]. Though very accurate and versatile, DFT calculations are computationally too expensive to produce images on a routinely basis. Thus, simpler and more efficient models have been created for this task. Bellow we review two of them, the simulated tip tilt methods (sec. 4.1.1) and the probe–particle model (sec. 4.1.2). Taking into account the widespread use of these methods, we address in this chapter their validity, in an attempt to understand why they work, and the specifics of their limitations.

4.1.1 Simulated probe tilt from lateral forces

Simulations of NC–AFM images with functionalized tips can be computationally costly due to the large number of ionic minimization steps needed to account for the tip tilt. In a scan, the forces exerted onto the tip provoke displacements of the molecule probe. The displacements sometimes take place in the radial direction with respect to the attachment point of the tip and the probe molecule, that is, a compression/elongation of the attachment bond distance, structural changes of the molecule, or rotations. Guo *et al.* propose that, under certain conditions, the probe displacement can be accounted for in an easy fashion through interpolation of a static image [166, 188].

The method is predicated on four conditions. 1) During the scan, the metal apex–CO and the C–O bond lengths do not change. This is justified by the fact that typical CO tip–sample interactions are usually less than 100 pN, much weaker than the axial metal apex–CO bond or C–O chemical bond. 2) The lateral displacement of the oxygen atom is linearly proportional to the lateral force when the tilt angle is small. This implies that the metal–CO system acts as a torsional spring, which indeed is a good approximation [241]. Computationally, the condition can always be met if the metal tip–sample interaction is separated from the CO–sample interaction. If the separation is not possible, the condition can only be met if the tip is in the vicinity of the sample in a lateral sense [128]. Otherwise the slowly decaying vdW interaction between the whole tip and the sample reduces the correlation between the lateral force and the displacement of the CO molecule. 3) The tip–sample interaction is predominately determined by the position of the oxygen atom relative to the sample. The assumption is justified for small tip–sample distances where the rapidly decaying Pauli interaction dominates. 4) The vertical displacement of the O atom due to the rotation is small. The condition is met if the metal–CO length (pivot arm) is sufficiently large. For instance, in a CuCO tip, the pivot arm is 3.95 Å. For a typically small tilt angle of 10°, the resulting vertical displacement of the O atom is 0.06 Å, very small compared to the 3.89 Å lateral displacement.

With these ingredients in mind, the displaced position of the oxygen atom

can be approximated by the linear response to the lateral force,

$$R^{\mathrm{x(y)}}_{\mathrm{displaced}} = R^{\mathrm{x(y)}}_{0} + F^{\mathrm{x(y)}}_{\mathrm{lat}}/k_{\mathrm{lat}}, \tag{4.1}$$

where k_{lat} is the lateral spring constant of the metal–CO tip and $R^{\mathrm{x(y)}}_{0}$ the lateral position of the O atom with the CO in an upright position. Thus, by computing both vertical and lateral rigid tip–sample forces on a CH grid, the effect of the probe tilt can be accounted for by correlating $R^{\mathrm{x(y)}}_{0}$ to $F_z(R^{\mathrm{x(y)}}_{\mathrm{displaced}})$ through an interpolation.

The method has been used to simulate small amplitude NC–AFM images of different molecules as probed by a metal–CO tip. Guo *et al.* simulate images of a pentance molecule [188] (fig. 4.1(a)) and a) a planar ethylene molecule, b) two Xe atoms, c) two HF molecules, d) the π–conjugated 2,6–di–tert–butyl–4-nitrophenol (DBNP) molecule, e) two 8–hq molecules, and f) a BPPA tetramer [166]. The rigid tip–sample interactions were calculated with DFT on a rectangular grid with 0.2 Å spacing and the CO tilt simulated by cubic polynomial interpolation. Recently, Lee *et al.* also simulated images of an 8–hq dimer (fig. 4.1(b)), an HF dimer, and a DBTH molecule by computing static F_z maps with DFT on a 0.5 a.u., 0.4 a.u., and 0.5 a.u rectangular grid and correcting for the CO tilt via cubic interpolation [165].

The images obtained with this method qualitatively reproduce many aspects of the experimental images. However, their application range is limited. Specifically, the premise of small angle rotations fails at close tip–sample distances where most HR–AFM are taken. In such cases, the lateral displacement of the oxygen atom is no linearly proportional to the lateral forces and the vertical displacement of the oxygen atom may not be small. In this chapter we explore how not fulfilling this premise affects the contrast.

4.1.2 Probe–particle model

Although simulating the probe tilt with interpolation greatly reduces the computational cost of including ionic relaxations, calculating the 2D static image with DFT is still timely and, in very large systems, may not be possible. In what follows, we describe an alternative approach that enables to obtain crude images

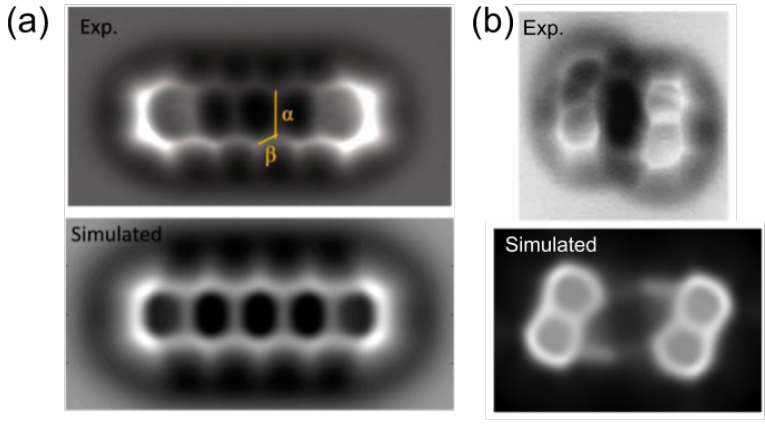

Figure 4.1: (a) Experimental AFM image of pentacene on Cu(111) [40] and simulated maps at z=3.7 Åwith k=0.5 N/m. (b) Experimental image of an 8–hq dimer [123] and simulated images at z=3.18 Å with k=0.4 N/m. Adapted with permission from [188] and [165].

without necessarily performing costly DFT calculations.

Typically, HR–AFM images are very rich in detail and have different contrast regimes depending on the tip–sample height. Furthermore, these experimental images are typically captured with molecular mobile tips where the dynamics of the tips is important for the contrast formation. Although *ab initio* approaches have been indispensable for the interpretation of SPM experimental data due to the computational cost, these techniques are not practical for simulating HR–AFM images. The tip flexibility requires that the calculations include ionic relaxations that make simulating even spectroscopies computationally expensive. This is the main motivation for the development of simple models based on pair–wise potentials to simulate HR–AFM images.

The probe–particle model refers to a method developed in 2014 by Hapala *et al.* [160] to simulate rapidly HR–AFM images with molecular functionalized tips. In the most basic form, it uses LJ potentials to compute the interactions between the tip apex, modeled as a single "probe–particle", and each atom in the sample. The probe–particle replaces the functionalized part of the tip, typically a CO molecule or a Xe moiety attached to the tip. In addition, the

interaction between the probe–particle and the rest of the tip is also modeled through classical potentials: A radial LJ potential to keep the probe–particle bonded to the tip and a lateral spring potential,

$$V = \frac{1}{2}k\Delta(x,y)^2,$$

to keep the probe in an upright position. This potential depends on the lateral $(\Delta x, y)$ displacement of the probe–particle with respect to the tip and not the rotational angle.

A similar method was developed independent by Hämäläinen *et al.* [189] to study graphene/Ir(111) moirés probed with a CO functionalized tip. In addition to the CO–graphene interaction, it also modeled, with LJ potentials, the interaction between the CO molecule and the Ir substrate and the interaction between the macroscopic tip and the graphene/Ir moiré.

There are several advantages of using LJ potentials to model the tip–sample interaction in HR–AFM with functionalized tips. First, the potential,

$$V = \frac{A}{r^{12}} - \frac{B}{r^6},$$

has a repulsive core and an attractive tail. This is an adequate description of the tip–sample interaction. The probe–particle is typically a closed–shell molecule and thus there are no significant bonding interactions. At short distances the interaction is mainly Pauli repulsion and at larger distances vdW attraction. Second, the potential only depends on the separation between the species and thus is computationally inexpensive. Lastly, the potentials are widely used in classical MM and MD simulations and thus there are a wide range of parameters available for most chemical elements.

The main contribution of these early pair–wise models was to help understand the role of the tip flexibility on the imaging mechanism of the CO tip. From early on, it was clear that the CO tilt was responsible for the molecular distortions typically observed in the HR–AFM molecular images [186]. On the one hand, these features are seen as artifacts, for instance the sharpening of the lines joining adjacent atoms (usually bonded atoms) [186] and increase of the lateral size of features arising from individual atoms [69, 241]. On the

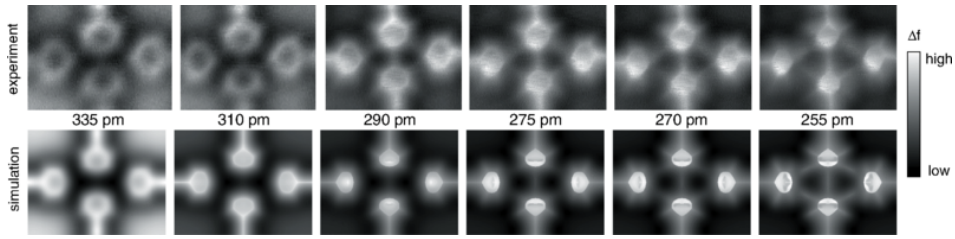

Figure 4.2: (top row) Experimental CH–AFM images with a CO tip taken at different heights on top of the BPPA tetrameter junction showing inter–molecular features at the lines joining N–N and C–H · · · N at close tip–sample distances. (bottom row) Simulated CH–AFM images with a flexible CO tip (k=0.6 N/m) using the probe–particle model. Reproduced with permission from [127].

other, when discriminating covalent bond orders, the detail deformed geometric structure bears crucial information [119].

These simple models based on pair–wise interactions are able to qualitatively reproduce the experimental images [121, 123, 127, 160, 189]. They explain the bond–like features in the images in terms of the critical behavior of the probe–particle deflection. In general, the tip tilt highlights saddle points of interaction potential between the probe–particle and the surface. Thus, images of molecule have sharp edges and thin inter– and intra–molecular bonds. However, as Hämäläinen *et al.* [127] pointed out, bond–like features can appear in the images in positions joining non–bonded atoms (see fig. 4.2).

4.1.3 Overview

In this chapter we unravel the contrast formation mechanisms of HR–AFM images of molecules with a method that goes beyond the accuracy of previous simulation methods, yet it produces images rapidly. This work is organized as follows: First, we briefly describe the method used to simulate images (sec. 4.2) and the system that it is applied to (sec. 4.3.1): a triazine Self–Assembled Monolayer (SAM) on graphene probed by a CO tip. Then, the DFT results obtained for this system and used to parametrize the model will be outlined (sec. 4.3.2). Subsequently, through static force-decomposed maps and frequency shift HR–AFM

images, we discuss the contrast mechanism of the molecular, intra-molecular and inter-molecular regions as a function of the tip–sample distance (sec. 4.3.3). This is of outmost importance for the interpretation of AFM experiments. Finally, the existence of different PES minima for the CO tilt will be discussed along with its influence on both theoretical and experimental imaging.

4.2 Methods

4.2.1 HR–AFM method on molecules

In the previous chapter we proposed a method to simulate interaction–decomposed HR–AFM images with DFT accuracy. The model separates the total tip–sample interaction into a vdW, ES, and SR contribution and accounts for penalty of a functionalized tip rotation (tilt). Given an initial tip position $\vec{R}_{\text{tip}}$, the coordinates of the probe are obtained by minimizing the potential

$$V(\vec{R}_{\text{tip}}, \theta, \varphi) = V_{\text{ES}} + V_{\text{SR}} + V_{\text{vdW}} + V_{\text{tilt}} \tag{4.2}$$

for the polar and azimuthal rotation angles (θ, φ) of the probe. The HR–AFM energy, force and frequency shift images at a given tip height are obtained by determining the probe positions that minimize Eq. (4.2) on a 2D grid, and evaluating the corresponding total energy, its gradient, and the second–order derivative with respect to the z–direction [5] respectively.

In contrast to the method described in the previous chapter, here we neglect the ES contribution coming from the metallic part of the tip (the apex that the CO is attached to). Such contribution is important in surfaces with large spacial variations of charges (for instance, ionic surfaces with defects). Consequently, the electrostatic interaction is calculated from

$$V_{ES} = \int \rho^{\text{probe}}(\vec{r}, \vec{R}_{\text{tip}}, \theta, \varphi)\phi^{\text{sample}}(\vec{r})\mathrm{d}\vec{r}^3, \tag{4.3}$$

where ρ^{probe} is the charge density of the probe and ϕ^{sample} the ES potential of the sample.

The SR interaction, which incorporates mainly Pauli repulsion but also charge redistribution effects, is fitted to a sum of pair–wise Morse potentials. The fit

is done on the SR component of system specific tip–sample DFT energy vs. distance calculations without ionic relaxations. The contribution is isolated by subtracting the ES interaction, computed as with Eq. (4.3), from the Kohn-Sham (KS) energy (the DFT energy without vdW interaction)

$$V_{\mathrm{SR}} = E_{\mathrm{KS}} - V_{\mathrm{ES}}. \tag{4.4}$$

For the NaCl surface examined in the previous chapter, two sets of parameters were used to describe the Morse potential: one for the Cl atoms and one for the Na atoms. For the triazine molecules studied in this chapter, using one set of parameters for each atomic species was not enough to reproduce the complex contrast behavior obtained from the DFT tip–sample interaction curves. An extra set of parameters of a "ghost atom" placed in the center of the molecules was required to parametrize the SR interaction. This will be discussed in detail in sec. 4.3.2.

4.2.2 Computational details

All DFT calculations were carried with the PAW method as implemented in VASP [255] using a $7\times7\times1$ Monkhorst-Pack grid for the Brillouin zone integration, a 600 eV plane-wave cutoff, a 10^{-6} eV accuracy electronic self–consistency loop and the PBE XC functional [209] supplemented by vdW DFT–D3 [223]. The ES potential of the sample and charge density of the probe used in eq. (4.3) were calculated on a uniform 3D mesh of $\lambda \approx 0.075$ Å spacing with the dipole correction applied to the z–direction to eliminate spurious interactions among the repeated unit cells.

Geometrical positions of the SAM were obtained through DFT ionic relaxation of all triazine atoms of a SAM on a (3×3) graphene supercell of $6.53 \times 6.53 \times 43.4$ Å^3 using the conjugate gradient algorithm until the residual force on each atom was less than $F_{\mathrm{min}} = 0.01$ eV/Å. The unit cell $(3\times3)_{\mathrm{graphene}}$ optimizes the binding energy of the molecule to the graphene. The calculated adsorption distance was 3.33 Å and the binding energy per molecule 405 meV. The molecules are adsorbed with negligible corrugation and form a triangular array with a 6.53 Å separation between molecules (fig. 4.3(b)). The SAM

induces a small rotation of the preferred adsorption sites of the isolated triazines on the graphene: the C atoms of the triazine on top of the graphene's C atoms. Triazine has been experimentally synthesized on a graphene/Pt(111) substrate [256], which is a weakly interacting grapehen on metal with a tiny corrugation (chapter 2).

All HR–AFM images computed from eq. (4.2) were calculated on a 2D mesh with $\lambda = 0.1$ Å spacing. Gradients with respect to the rotation angles, computed analytically, were used to converge more readily the probe rotation. The probe position was relaxed using the Broyden-Fletcher-Goldfarb-Shanno (BFGS) algorithm until the generalized gradients were less than 10^{-4} au.

4.3 Results and discussions

4.3.1 Sample characterization

Here, we apply the method described above to simulate HR–AFM images of a triazine SAM on graphene probed by a CO tip. Each triazine is an aromatic six–member ring molecule with alternating C–H and N atoms (fig. 4.3(a)). They bind into a triangular lattice SAM via C–H $\cdots$ N hydrogen bonds (H–bonds)and are physisorbed onto the graphene (fig. 4.3(b)). Although triazines can be grown on other substrates [257, 258], graphene, with its very low reactivity, promotes the formation of well–ordered layers with no chemical coupling to the SAM [220, 259]. Thus, this 2D system is ideal to study the contrast formation of the AFM with functionalized tips: the SAM is flat and thus removes corrugation effects. In addition, it presents 3 types of chemical species, and it has both covalent intra–molecular coupling as well as inter–molecular coupling through H–bonds.

Figs. 4.3(c)–(d) show the charge density and the z–component of the ES field of the traizine SAM/graphene at a plane $z = 3$ Å from the surface. The charge density has a triangular shape coming from the dominant N lone pairs (see $\rho(\vec{r}, E = E_{\text{HOMO}})$ on fig. 4.3(a)). These also dictate the form of the z–component of the ES field. It is attractive towards electrons inside the molecule and repulsive outside, with the repulsive centers created by the lone pairs of the

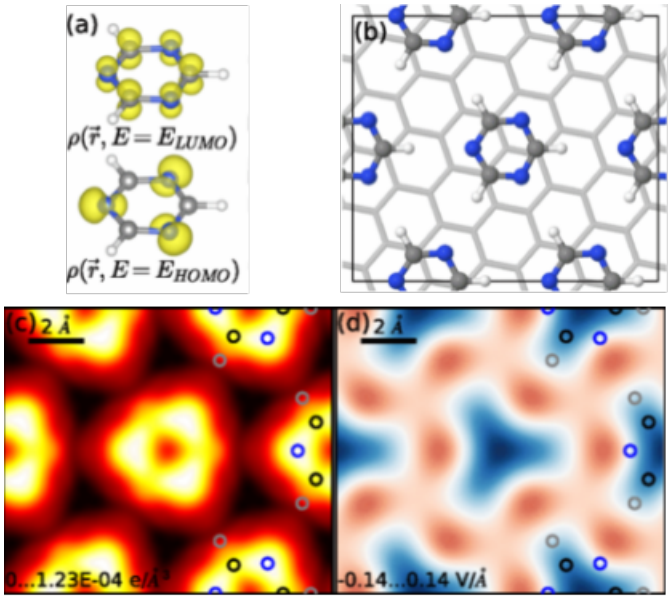

Figure 4.3: Triazine molecules on graphene. (a) Projected charge density of the isolated triazines at the HOMO and LUMO energies. (b) SAM adsorbed on a $(3 \times 3)_{\text{graphene}}$ unit cell. (c) Total charge density and (d) z-component of ES field of the SAM at a height of 3 Å. (Blue, positive and red, negative).

N atoms. Although the charge density of the SAM is very similar to the one of the isolated triazine molecules, there are faint inter-molecular features present in the charge density far from the plane of the molecule. Its origin is not related to a charge transfer with the substrate or charge redistribution of the SAM (both of which are negligible [1]), but to the overlap of the C–H$\cdots$N electronic densities of neighboring triazine molecules.

4.3.2 Force spectroscopy

In order to simulate HR–AFM images with the method described in sec. 4.2.1, the SR Morse parameters are first fitted to DFT calculations. To this end,

[1] The maximum charge transfer with the substrate is 1.4×10^{-6} e/Å^3 and in the inter-molecular region 2.0×10^{-7} e/Å^3. The maximum charge transfer due to the presence of neighboring triazine molecules is 1.25×10^{-4} e/Å^3 and in the inter-molecular region 6.5×10^{-6} e/Å^3

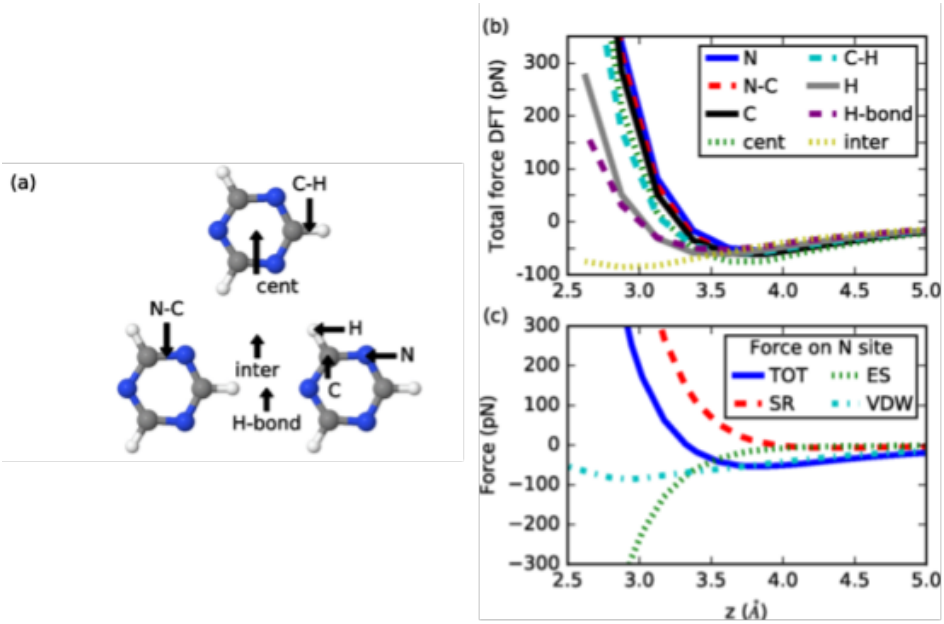

Figure 4.4: DFT force vs. distance calculations of a triazine SAM/graphene probed by a CO molecule. (a) Scheme of sites. (b) DFT results of all the sites. (c) Total (TOT) force and ES, vdW and SR force contributions on the N site.

DFT+vdW force vs. distance calculations keeping the CO molecule fixed are performed on the CO tip – triazine SAM/graphene sample system. The tip is placed on 8 sites of the SAM (fig. 4.4(a)): above N, C and H atoms, in between bonded atoms of the triazine C–H, N–C and C–C, in the center of the molecule (cent), and in 2 inter-molecular regions (H-bond and inter). As the tip approaches the sample, the total force is first attractive and then repulsive (see fig. 4.4(b)). The N site exerts the highest repulsion for tip–sample distances $z < 3.6$ Å and comparable to other high-density C, C–C and C–N sites. Although the center of the molecule does not have high electron density, it is the fourth most repulsive site. The C–H site yields very similar forces to the center site, and the H and H-bond sites are less repulsive. Finally, the inter–molecular region with least electronic density (inter site) yields the weakest force; it is the only site still attractive at $z = 2.5$ Å. Each of these tip–sample interactions can be decomposed into ES, vdW, and SR components. Fig. 4.5(c) shows the

decomposition on the N site. Due to the overlap between the CO and triazine wave functions, the SR force (mostly originated from Pauli repulsion) grows exponentially as the tip–sample distance decreases. Likewise, due to the overlap of electronic densities, a similar rate of decay (growth in magnitude) occurs in the ES force. This results in a strong cancellation between these two, with the SR dominating at small tip–sample distances ($z < 3.2$ Å). Nevertheless, for $z > 4.0$ Å the vdW is the dominant interaction. It is also worth noting that it is the only interaction that is affected by the presence of the graphene substrate. That is, for all other interactions, the CO tip - triazine SAM/graphene and the CO tip – triazine SAM are equivalent. This is in accordance with the large decay in the magnitude of the SR and ES forces with increased tip–sample distance.

From the DFT force versus distance calculations, the SR interaction is extracted using eq. (4.4) (markers in fig. 4.5(a)) and fitted to pair–wise Morse potentials between a Morse center placed at the tip apex (O atom) and centers placed in the sample's plane (lines in fig. 4.5(a)). Admittedly, the large growth of the SR force complicates the modelling of the interaction through pair–wise potentials. The strong cancellation between the SR and ES force requires a high-precision parametrization. We find that using 3 species of Morse centers, one for each distinct atomic species (N, C, H), and placing the centers at the atomic positions of the triazine SAM, is not enough to reproduce the rich contrast of fig. 4.4(b). This can be appreciated in fig. 4.5(c) where the total DFT force (markers) and the model's (lines) are plotted. The problem is solved by augmenting the variational freedom of the fit by adding a ghost Morse species to the center of the hexagons of the triazines. This improves the precision of the fit and provides an excellent agreement between the DFT and the model's results for the full range of tip–sample distance (see fig. 4.5(b)). Possibly, the need for a ghost species comes from the lack of directionality of the Morse potential that may be important when modeling aromatic molecules. Namely, they have σ and π bonds that make the directionality of the charge density relevant. Note that no Morse centers are placed in the plane of the graphene. As stated before, for this system, the substrate does not play any role in the SR interaction.

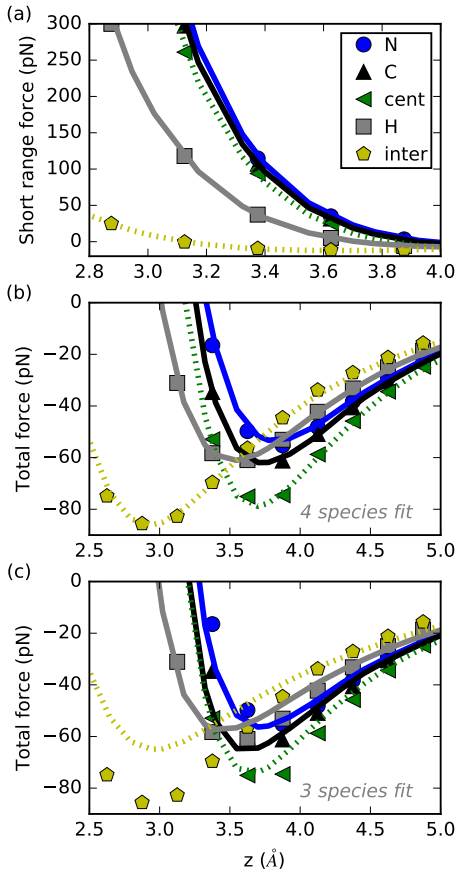

Figure 4.5: Parametrization of the AFM simulation model using 4-species (N, C, H, and cent) and 3-species (N, C, and H). The markers are the DFT input data and the lines the results of the models. (a) Parametrization of the SR force using the 4-species model. (b) Total force obtained with the 4-species model and (c) 3-species model.

4.3.3 HR–AFM images

After achieving an excellent fit to the DFT calculations, interaction-decomposed images without tip relaxation are simulated. These are key to understand the contrast mechanism of the CO tip. Fig. 4.6 shows the static maps (without probe relaxation) for 5 tip–sample distances from $z = 2.87$ Å to $z = 3.93$ Å. In order to highlight the contributions, the gray scale in each plot is fixed by

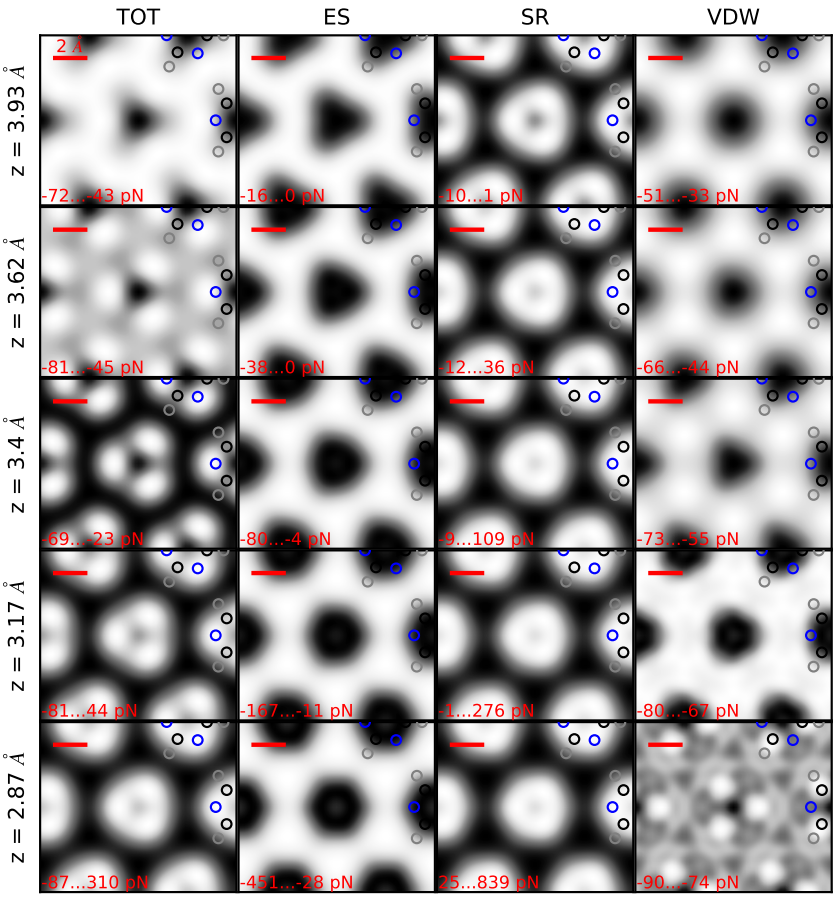

Figure 4.6: Static force decomposed AFM images of a triazine SAM/graphene probed by a CO tip. From left to right the total (TOT), ES, vdW, and SR force maps for 5 tip heights (top to bottom). Scale bars correspond to 2 Å. The gray scales correspond to the minimum (dark) and maximum (bright) value of the interaction shown in the bottom left corner of each image.

the maximum and minimum value of the interaction. For large tip–sample distances ($z > 3.6$ Å), the attractive vdW and ES interactions dominate and make the inside region of the molecule the most attractive feature of the image. The ES maps have a triangular shape at the molecules with the vertices at the C atom positions. In contrast, the SR is repulsive and partially cancels the ES contribution. In these maps, the molecule is the most repulsive part

and images also have triangular features but with vertices around the N atoms. The net interaction has dark (attractive) features at the triazine positions with a triangular shape given by the remnant ES and vdW interactions. As the tip–sample distance decreases, the SR–ES cancellation leans in the direction of the repulsive SR interaction. On the other hand, the vdW contrast becomes negligible (see contrast range values in fig. 4.6). This leads to a change in contrast of the total force with bright (repulsive) features around the N atoms of the molecules. At very small tip–sample distances, $z < 2.9$ Å, very faint intermolecular features appear both in the total force and SR contribution. These can already be appreciated in the charge density of the SAM (see fig. 4.3(c)) and originate from the spatial overlap of the C–H $\cdots$ N outermost electrons of adjacent triazine molecules [165, 166].

It has been proposed that the contrast in AFM images may be explained exclusively from sample related properties, such as the electronic density or the associated electric field [112, 162, 166, 181, 186, 190, 260]. However, in our calculations, for all tip–sample distances, the ES force does not exactly resemble the z-component of the ES field of the SAM. For large distances, $z > 3.6$ Å, it has attractive triangular features with vertices at the C–Hs of the triazines. As the distance decreases, the features become more hexagonal and follow the perimeter of the molecule. The effect reflects the non-localized nature of the CO molecule's charge distribution. That is, the ES interaction is a 3D average of the ES potential of the sample weighted by the CO non-spherical charge distributions. Similarly, the SR contribution does not exactly resemble the charge density of the SAM. For large distances, $z > 3.6$ Å, it also has repulsive triangular features but with vertices at the N atoms. Even though the N atoms have more localized charge density than the C atoms, the SR repulsive feature also merge into hexagons as the tip sample distance decreases. This also indicates that the interaction resembles not just a z-average of the charge density of the outermost electrons of the sample [129, 166] but a 3D average. It also explains why the centers of the molecule have high repulsion even though the electronic density is low. Surprisingly, when both SR and ES contributions are joined, the 3D averaging effect seems to be reduced. At large tip–sample

distances, $z > 3.6$ Å, the total force appears more like the z-component of the ES field (fig. 4.3(c)) than the ES interaction map. Similarly, at small tip sample distances ($z < 3.2$ Å), the total force resemblance to the charge density of the SAM (fig. 4.3(d)) is greater than the SR resemblance to the charge density.

The SR–ES strong cancellation also explains why point-like methods to simulate HR–AFM images reproduce qualitatively (or even quantitatively) the experimental images or the more accurate DFT simulations. In these methods [160, 189], the averaging effects of the tip are not explicitly included. Nevertheless, as a result of the cancellation, the PES can be fitted to a polynomial (R^{-n}) potential, i.e. LJ. Also, the induced effect of the sample's charge distribution differences can be incorporated with a point–like approach to the ES contribution [164].

With the insight gained by understanding the origin of the tip–sample interaction, we are now in a position to discuss the effect of the tip tilt [40, 119, 160, 186] on the HR–AFM images, the underlying interaction that controls it, and its effect on the imaging of inter-molecular features [123]. Fig. 4.7 shows the total force, frequency shift and relaxation maps of the probe. Due to attraction coming from the ES and vdW interactions in the center of the molecules, there is a slight tilt of the CO tip towards the molecules ~ 0.3 Å at $z = 3.7$ Å. However, for large tip–sample distances, $z > 3.6$ Å, the total force is barely perturbed by the tip, and resembles the z-component of the ES field. At intermediate tip–sample distances, $z < 3.6$ Å, the relaxation induced by high electronic density sites, i.e. C, N and covalent bonds, defines the contour of the molecule [40, 119] and results in a sharpening of the triangular stripes seen in the static maps. The characteristic triangular shape displayed by the triazine is due to the large electronic density of the N atoms compared to the C–H groups, even far from the molecule (fig. 4.3(c)). Notice that the behaviour of the N atoms in the triazine differs from what has been observed in large molecules with several six-member rings and containing only very few N atoms [130, 171]. In that case, the electron density coming from the C atoms decays more slowly than the N's, resulting in weaker repulsion at the N atoms compared to the C atoms.

The relaxation, which is shown more explicitly in fig. 4.8, is significant for

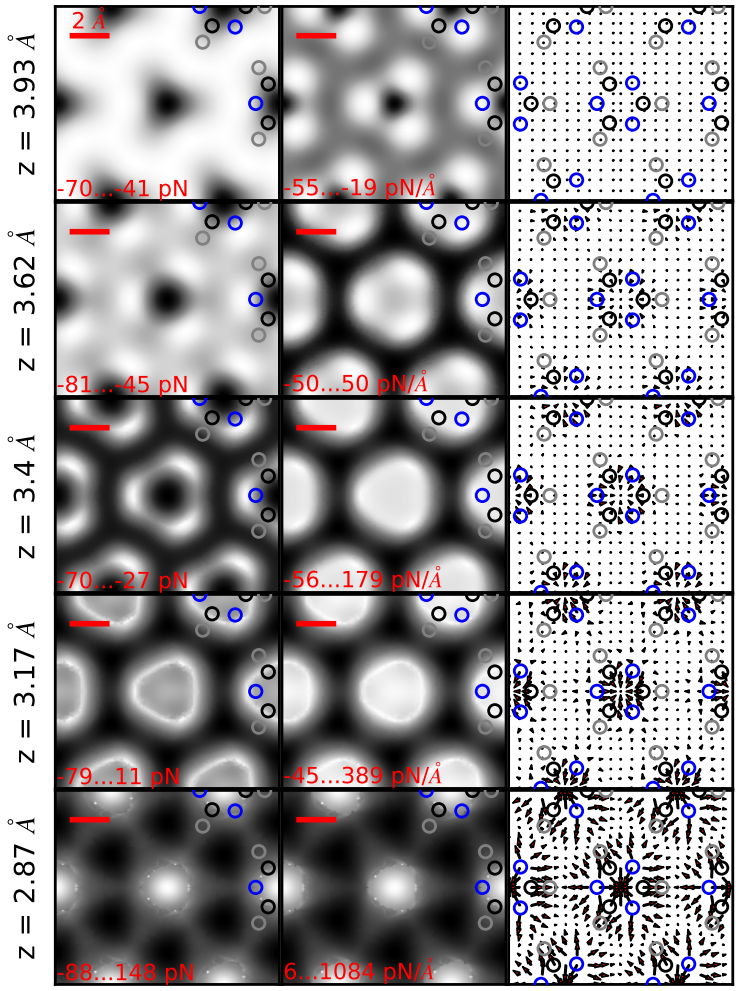

Figure 4.7: Simulated AFM images of a triazine SAM/graphene probed by a CO tip. The first column is the total force, the second the reduced frequency shift (-dF/dz), and the third arrows showing the lateral relaxation of the CO probe. Scale bars correspond to 2 Å.

intermediate to small tip–sample distances ($z < 3.6$ Å), where the SR repulsion overpowers the other interactions. Due to increased electronic density, the relaxation is dominated by the N atoms. Consequently, the CO starts tilting near the N site at larger tip–sample distances compared to other sites. Also, outside of the molecules, the CO tilts away from the N atoms and towards the

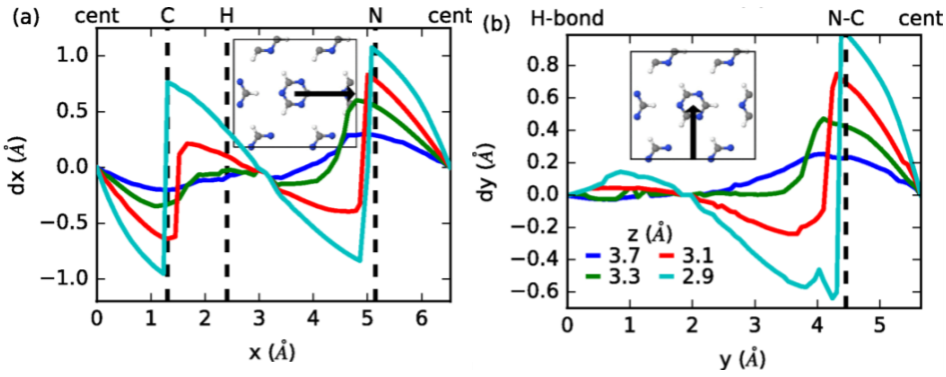

Figure 4.8: Lateral tilt distance of the CO probe along two profiles of a triazine SAM/graphene and for 4 tip heights. (a) A profile along the x-direction from the center of a triazine molecule to the center of a neighboring molecule and passing through C, H and N atoms, and (b) a profile along the y-direction from an H-bond region to the center of a triazine molecule and passing through a N-C bond.

neighbourhood of the C–H groups. Finally, we consider the effect of the vdW interaction on the CO tilt. For an isolated molecule, the vdW attraction causes a tilt towards the molecule [119]. However, in the SAM, the lateral attractive vdW interaction in the middle of the inter-molecular space, which results from the contribution of all the neighboring molecules, cancels out and has a very minor effect on the CO tilt.

At small tip–sample separations, $z < 3.2$ Å, the CO tilt enhances the ripples connecting the triazine molecules in the H-bond directions [123, 160]. Although they are weakly apparent in the charge density and static maps, the ripples are augmented at this distance range (see fig. 4.7). In this case, the relaxation is dominated by the slowly decaying charge density of the N atoms. It softens the high repulsion areas induced by the molecules, that is, the intra-molecular areas, and renders visible the inter-molecular features [165, 166]. Notice that these are not shaped as linear stripes (sharpening of the saddle lines), but instead have a faint triangular shape. This is produced by the particular relaxation pattern around the C–H area created primarily by the two neighbouring N atoms. This discussion shows that the appearance of the ripples is linked with the PES. Forces

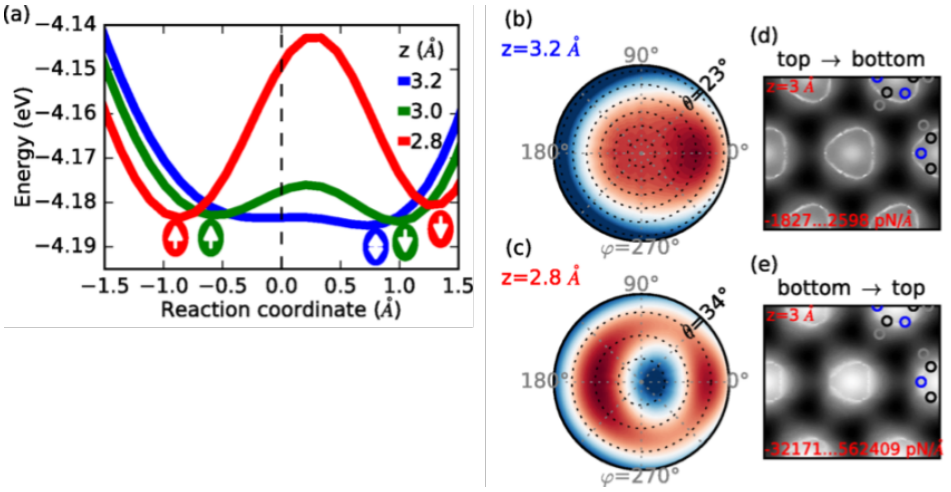

Figure 4.9: Energy landscape of CO probe on triazine SAM/graphene. (a) Energy profile along the reaction coordinate of the CO movement with the probe placed 1 Å away from an N atom in the direction of the H-bond. (b)–(c) Energy maps with respect to the polar angle (θ) and the azimuthal angle (φ) on the same tip position as (a). Simulated AFM images at $z = 3$ Å with (d) top-to-bottom and (e) bottom-to-top relaxation.

are very weak at the inter-molecular region (∼100 pN) and we do not expect the associated ionic relaxation (not considered in our calculations) to change significantly the structure and symmetry of the PES, and, thus, the appearance of the ripples.

As explained before, for large tip–sample distances ($z > 3.6$ Å) the CO tilt direction is dictated by the vdW and ES interactions. These always attract the probe towards the molecule. Conversely, as the distance decreases, the SR interaction creates a barrier that pushes the probe away from the molecule. The change of regime suggests that the relaxation PES of the probe is complex. Indeed, here we point out the existence of different PES minima of the CO tip at both sides of the triangular contour of the molecules. For instance, at a tip lateral distance of 0.95 Å from the N atom in the direction of the H-bond, the relaxation PES has two minima for a range of tip heights. These are shown in fig. 4.9(a) where the tip–sample energy as a function of the reaction coordinate, defined

as the CO's lateral displacement along the minimum energy path obtained by varying the probe tilt angle, is plotted for three different tip heights. The zero of the reaction coordinate corresponds to the CO in an upright position and the positive values correspond to displacements towards the N atom. The full PES for two tip–sample distances are shown in fig. 4.9(b)–(c). The PES at $z = 2.8$ Å and $z = 3.0$ Å have two minima, and in contrast, the PES at $z = 3.2$ Å has only one. This is explained by the growth of the SR barrier around the molecule as the tip–sample distance decreases (see fig. 4.6), which produces an even-degree polynomial relaxation PES with two turning points. This may have important consequences for HR–AFM image simulations, that is, different images may be obtained depending on the energy minimization procedure, e.g. local vs. global minimum search or initial conditions. For instance, in the present case, if maps are calculated from top to bottom, that is, the rotation angles obtained from the minimization of a higher tip distance are used as initial conditions, the probe would always relax towards the molecule. On the other hand, if maps are calculated from bottom to top, or if a global minimization algorithm is used, at small tip heights the probe would relax away from the molecule. As shown in fig. 4.9(d)–(e), this would lead to different HR–AFM images.

The trapping of the probe on a PES minimum should also be factored into the interpretation of experimental images where the experimental settings, e.g. temperature, scan mode, etc., may cause alterations in the measurements of bond lengths and bond orders. This could be especially important in systems with large ES interaction, for instance in polar or ionic samples, or with charged functionalized tips, e.g. a Xe metallic tip.

4.4 Conclusions

We have proposed a model to rapidly simulate interaction-decomposed HR–AFM images with DFT accuracy. The model is parametrized through DFT calculations and decomposes the total tip–sample interactions into SR, vdW and ES contributions. The latter takes into account the charge distribution of both the tip and the sample. We have used the method to study the imaging of a triazine SAM by a CO tip. We have shown that the ES interaction maps a 3D

average of the sample's z-component of the ES field, while the SR interaction maps a 3D average of the sample's charge distribution. The strong cancellation between the SR and ES contribution in the final, total interaction results in (1) a reduction of the 3D averaging effects and (2) a less pronounced repulsive total interaction at small tip–sample distances (compared to Pauli's). For large tip heights, the resulting total interaction resembles the z-component of the ES field of the sample. In contrast, for small tip heights it resembles the charge distribution. The strong cancellation also explains why simple pair–wise point-like models qualitatively reproduce the HR images.

Strikingly, HR–AFM images of the triazine present a strong asymmetry between the C and N atoms, with the latter being more repulsive at small tip heights. The tilt of the CO tip highlights the triangular contour of the N atoms and, at very small tip heights, inter-molecular features (H-bonds). These stripes, due to relaxation towards the C–H groups induced by repulsion from the neighboring N atoms, have a triangular shape. We attribute their appearance to (1) the overlap of the electronic densities of the C–H and N atoms involved in the H-bond, and (2) their enhancement upon the tip tilt to a lowering of the overall contrast.

We have also examined the 3D PES of the CO tip in the SAM and point to the existence of two minima at the contour of the triazine. This may have observable consequences, both theoretical and experimental, on the distortion of the image, and the comparison of images obtained via different scan modes.

5 Charge density based description for the SR interaction: contrast formation of intra– and inter–molecular features in HR–AFM images

In the previous chapter we explored the contrast formation of images of molecules with a method that describes the ES interaction based on the charge density of the tip and electric potential of the sample, and the SR in terms of pair–wise Morse potentials. Although the method produces images that reproduce many features that appear in experimental images, there are several issues with the method. First, the SR interaction requires a large number of parameters for the fitting. This is not only computationally costly, but also obscures the interpretation of the results. Second, due to a strong cancellation with the ES interaction, the SR interaction needs to be modeled accurately. The fact that both interactions are treated through such different approaches impedes the strong cancellation and result in images with rounder edges compared to experimental images. Third, details that come directly from the charge density of the sample, for instance bond–order discrimination, cannot be simulated without using a very large number of parameters to fit the SR interaction.

Here, we develop a new method, with few parameters, that puts on equal footing the SR and the ES interaction by describing the SR in terms of the overlap of the charge densities of both the tip and the sample. With this, we investigate intra– and inter–molecular features observed in AFM images that are closely related to subtle effects in the charge density of the sample. First we demonstrate that not only structural similar molecules with different stoichiometry provide qualitatively different AFM images, but that the chemical en-

vironment (i.e., bonding structure) is also important. Second, we pinpoint the Pauli repulsion as the underlying mechanism responsible for the discrimination of covelant bond orders with CO tips. Lastly, the probing of weak intra–molecular bonds associated with H–bonds is investigated.

5.1 Introduction

Previously, we explored general features of the intra– and inter–molecular contrast of HR–AFM images with CO probes with a focus on 1) the effect that the tip tilt has on these features, 2) the existence of multiple minima in the PES, and 3) the strong cancellation between the SR and ES interaction. In this chapter, we address finer features in the images which are closely related to subtle effects in the charge density of the sample. For this, we develop a method that has a direct input from the charge density of the sample on the SR interaction. It is closely related to a methodology developed by Moll *et al.* [190] (see sec. 5.1.1) to describe the Pauli repulsion between a rigid CO tip and the sample in terms of the charge density of the sample using a two parameter fit from DFT tip–sample interaction curves. This is not the only method that incorporates 3D grid data properties of the sample to simulate images. In the previous chapter, we reviewed the most basic form of the popular probe–particle model which uses LJ potentials along with the associated CO tilt restoring potential to produce HR images of molecules. An improved version of the probe–particle model, on top of the LJ potentials, incorporates a description of the ES interaction in terms of the electric potential of the sample and an effective point charge for the tip (sec. 5.1.2). This addition allows reproducing subtle inter–molecular effects like bond–order discrimination, though the interpretation is obscured.

5.1.1 Moll's Pauli approximation

In this section we will briefly describe a method developed by Moll *et al.* [190] to create HR–AFM images based on the Pauli repulsion. We start by defining, in a non-rigorously way, the Pauli repulsion. It stems from the Pauli exclusion principle which states that no two electrons may occupy the same quantum

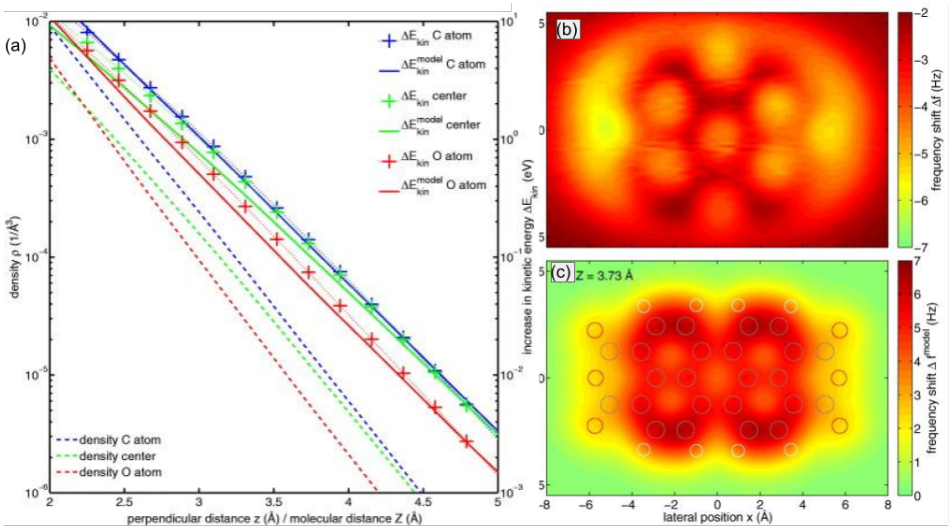

Figure 5.1: Top row: the charge density of a perylene-tetracarboxylic-dianhydride (PTCDA) molecule at a perpendicular distance (a) z = 2.46 Å and (b) z = 3.73 Å. Middle row: the increase in kinetic energy ΔE_{kin} of a PTCDA and a CO at a molecular distance (c) z = 2.46 Å and (d) z = 3.72 Å. Bottom row: the increase in kinetic energy $\Delta E_{\text{kin}}^{\text{model}}$ from the simple model for a PTCDA and a CO molecule at a molecular distance (e) z = 2.46 Å and (f) z = 3.72 Å. Reproduced with permission from [190].

state simultaneously. When two electrons of the same spin state intersect in space, their wavefunctions must become orthogonal. This translates into an increase in the number of nodes of the wavefunctions around the shared regions of space. In other words, their orthogonalized wavefunctions take on larger slopes to keep their overlap null. The increase in slope causes an increase in kinetic energy, which reflects the Pauli repulsion. It is important to note that the Pauli repulsion is not a force in the classical sense. Yet, it is useful to define interaction terms that reflect the effects of the Pauli repulsion. In this section two terms are used for this: 1) E_{Pauli} is defined as the energy difference between orthogonalized and non-orthogonalized wavefunctions as computed by DFT; 2) ΔE_{kin} is defined as the kinetic energy difference between orthogonalized and non-orthogonalized wavefunctions.

From the first experiments of the pentacene molecule [40], it was apparent, by the presence of CO tilting effects, that the observed intra–molecular contrast stemmed from the Pauli repulsion. Indeed, Moll *et al.* [186] demonstrated that E_{Pauli} qualitatively resembles the DFT interaction maps and the experimental Δf images. In the same article, the authors also reached an important conclusion – the interaction maps calculated from the non-orthogonal wavefunctions compare well to the fully self-consistent interaction energy. This indicates that the molecules are inert and exhibit no binding interaction. These conclusion suggested using just the charge density of the sample [162, 166, 188] to explain experimental images. However, as we concluded with the work developed in the last chapter, the approximation only works due to the strong cancellation of the ES and SR interactions.

The conclusion of ref. [186] also prompted Moll *et al.* [190] to create a method to simulate the images with only one DFT calculations (à la TH [204] in STM). The logic behind this was that, instead of approximating the HR–AFM images to E_{Pauli}, they would be approximated to a modeled version of the change in kinetic energy: $\Delta E_{\text{kin}}^{\text{model}}$. In order to justify the method, the authors calculated the increase in kinetic energy of two H atoms. From the unperturbed wavefunctions of the atoms, the Gram-Schmidt normalization is applied and the expectation value of the kinetic energy operator computed. The resulting energy has an exponential term equal to the charge densities of the atoms multiplied by polynomial terms of the distance and nuclear charges. At large distances, the exponential term dominates. For a system of two atoms with different nuclear charges, the increase in kinetic energy has a more complicated form. However, for large distances the relationship holds and the exponential term dominates. From this result, the authors propose a simple power law for the increase in kinetic energy:

$$\Delta E_{\text{kin}}^{\text{model}}(R) = A\rho_{\text{sample}}(R)^B \tag{5.1}$$

where ρ_{sample} is the charge density of the sample and A and B are probe dependent parameters. These parameters are fitted to the increase in kinetic energy versus distance as calculated from DFT for the distance range 2-5 Å. For an isolated O atom acting as a tip and isolated atoms acting as a probe A varies

between 934 and 1494 eV and the B parameter between 0.77 and 0.79.

The method was tested on a model system of a PTCDA molecule as probed by a CO molecule [190]. The parameters were fitted to DFT increase in kinetic energy curves over a C atom of the PTCDA and resulted in A=692 eV and B=0.78 (comparable to the values obtained for the O tip). Fig. 5.1(a) shows the comparison of the change in kinetic energy as calculated by the eq. 5.1 ($\Delta E_{\text{kin}}^{\text{model}}$) and by DFT ($\Delta E_{\text{kin}}$) above a corner O atom, a center C atom and on the center of the molecule. The method reproduces well the fitted C site but underestimates the O and center sites. By computing eq.5.1 on a 2D grid, interaction maps are obtained, and in a very similar fashion, the associated Δf maps. These maps have features that compare well with the experimental images of the PTCDA (fig. 5.1(b)–(c)). However, the biggest flaw of the method is that the Δf values don't resemble, even in sign, the experimental ones.

The method was also used by Wang *et al.*[162] to study the influence of the BPPA tetrameter adsorption onto a substrate on the N–N inter–molecular features observed in the images [127].

5.1.2 Probe-particle model with ES interaction

In order to capture effects related to the electronegativity of atoms in a molecule (imaged with STMH (STMH)), Hapala et al. [164] expanded their probe–particle model to include electrostatic effects in the calculation of the tip–sample interaction. Specifically, on top of the LJ potential, it computes the interaction as the overlap between the charge density of the probe–particle (ρ_{PP}) and the Hartree potential of the surface v_{S}^{H}. Although the actual charge density of the probe can be used to calculate the interaction, in practice, the probe–particle was modeled with a point charge Q_{PP}. The resulting interaction is thus:

$$V_{\text{ES}} = v_{\text{S}}^{\text{H}}(\vec{R}_{\text{PP}})Q_{\text{PP}}.$$

With this new ingredient, more subtle feature observed in the images can be addressed. Particularly, how changing the specifics of the mobile probe affects the images. For instances, the cobalt-phthalocyanine [164] PTCDA [39, 61] and BPBA [63] has been imaged with Xe and CO tips and interfacial water [155]

with Cl and CO tips. In all these cases, the difference in ES interaction resulting from changing the charge of the probe seems to play an important role in the contrast. From this, it has been suggested that by comparing images obtained from tips with different effective charges, the ES potential of the sample can be discerned [62]. A combined experimental and theoretical approach with this method also shed some light onto the influence of the charge of the probe on chemical recognition of molecules suggesting that neutral probes result in $z_{\text{min}}(x, y)$ and $\Delta f_{\text{min}}(x, y)$ maps that have more distinctive characteristics [144].

Despite the advantages of including a separate ES interaction on top of the LJ potentials on the probe–particle model, the results obtained with this method can be misleading. In the original work of bond order discrimination, the authors argued that different apparent bond lengths in the C_{60} molecule were a reflection of how different amounts of charge density (depending on the bond order) affected the tilt of the CO molecule [119]. This relationship obviously cannot be captured by a simple pair–wise model that calculates the interaction between the probe–particle and the atomic species. The Pauli interaction, including effectively in the LJ potential, does not account for the increased charge density in the C–C bonds. However, by including the ES interaction as described above, the probe–particle model is able to reproduce qualitatively the effect [61] (fig. 5.2). Although the authors do not rule out the role of extra Pauli repulsion due to the enhanced electron density at the bonds, they highlight that the ES interaction is probably the important factor leading to the enhanced discrimination of the bond order in CO functionalized tips.

5.1.3 Overview

Inspired by Moll's approximation of the Pauli repulsion (sec. 5.1.1) and the probe–particle model (sec. 5.1.2), in this chapter we develop a new method to simulate HR–AFM that puts on equal footing the SR and ES interaction. The chapter is organized as follows: In sec. 5.2.1 the new method is described along with the computational details (sec. 5.2.2) of the calculations. The use of the method is illustrated using the pyridine molecule which is a 6–membered

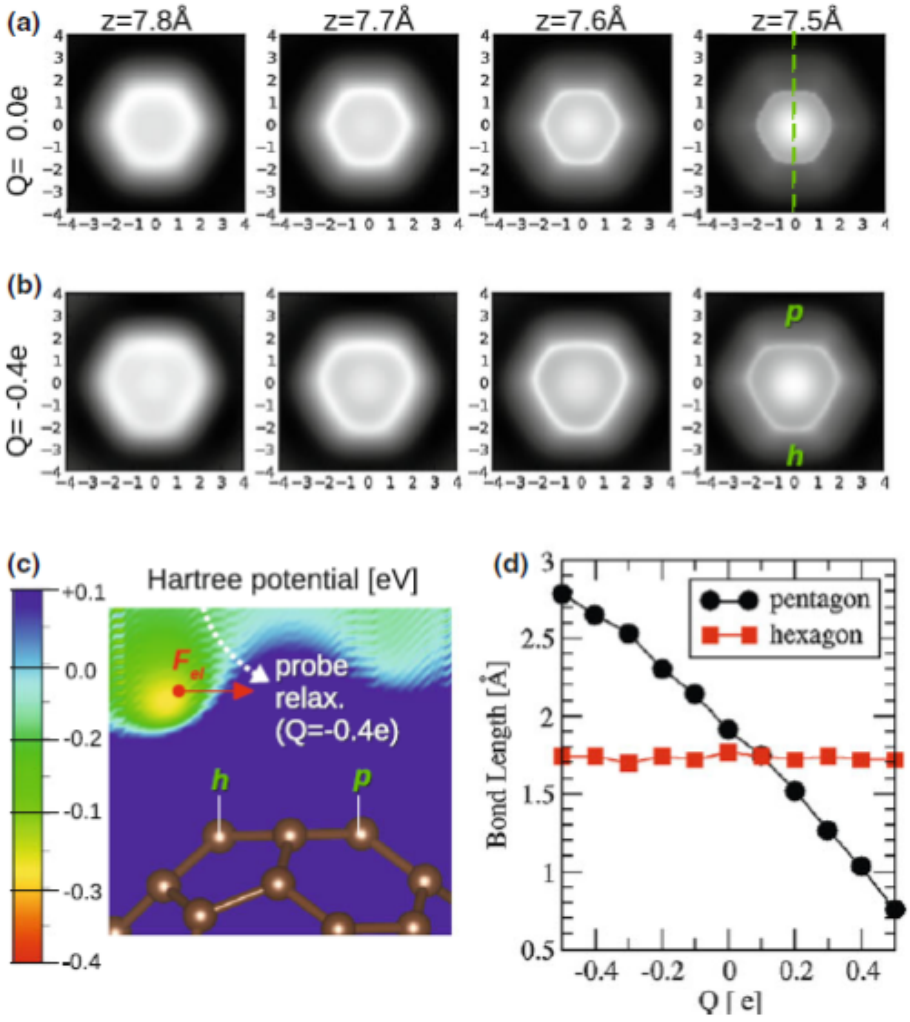

Figure 5.2: Calculated AFM images of C_{60} molecule using functionalized tip (a) without (Q = 0.0e) and (b) with (Q = -0.4e) the ES interaction acting between the particle probe and C_{60} molecule. (c) Cut-plane of Hartree potential through the centers of a C_{60} hexagonal face showing different distribution over h-bond and p-bond. Dashed white line depicts schematically relaxation of the probe particle due to the presence of the electrostatic force. (d) Bond length dependence of h-bond and p-bond on the effective charge on the probing particle Reproduced with permission from [61].

rings with one N heteroatom (sec. 5.3.1). The rest of the N heterocyclic 6–membered rings are studied in sec. 5.3.2. The results help identify how the local environment of the atoms manifest themselves as subtle distinctive features in the images. In sec. 5.3.3 the complex Breitfussin molecule is used to test capabilities of the model to treat non–planar molecules with a large number of chemical species. The C_{60} molecule (sec. 5.3.4) and 8–hq dimer (sec. 5.3.5) are used to address important questions concerning the sensing of intra– and inter–molecular features with the AFM. Finally, the 6–memebered rings are revisited in sec. 5.3.6 to address the possibility of the model of using universal parameters.

5.2 Method

5.2.1 HR–AFM image simulation method

Here we develop a method to simulate HR–AFM interaction-decomposed images with DFT accuracy that is rapid, has few parameters, and explicitly takes into account the ES potential of the sample (ϕ^{sample}) and the charge density of both the sample (ρ^{sample}) and the probe (ρ^{probe}). The tip–sample interaction is decomposed into an ES, vdW, and SR components and the mobility of the probe is accounted for through a restoring harmonic potential. For a given tip's initial position $\vec{R}_{\text{tip}}$, the probe's relaxed coordinate is obtained by minimized the potential

$$V(\vec{R}_{\text{tip}}, \theta, \varphi) = V_{\text{ES}} + V_{\text{SR}} + V_{\text{vdW}} + V_{\text{tilt}} \tag{5.2}$$

with respect to the tilt polar θ and azimuth ψ angles. A 2D energy map is obtained by evaluating the above potential on a grid. Force maps are calculated from the first derivative with respect to the z direction of eq. 5.2 and, in the small oscillation regime, frequency shift maps from the second derivative [5]. The ES, vdW and tip tilt potentials are calculated with the same functional form as our previous model (described in the previous two chapters). The ES interaction is computed from the overlap of ϕ^{sample} and ρ^{sample} as

$$V_{ES} = \int \rho^{\text{probe}}(\vec{r}, \vec{R}_{\text{tip}}, \theta, \varphi)\phi^{\text{sample}}(\vec{r})\mathrm{d}\vec{r}^3. \tag{5.3}$$

The vdW interaction is obtained using Grimme's DFT–D3 approach [223] and the probe's tilt energetic penalty V_{tilt} through a restoring potential. For the CO tip with polar symmetry, it has the form of a torsion spring

$$V_{\text{tilt}} = \frac{1}{2}\kappa\theta^2. \tag{5.4}$$

A spring constant $\kappa = 0.01$ Ha/rad^2 seems best to reproduce experimental results [160, 164, 189].

The new ingredient of the method is the way the SR interaction is obtained. We noticed in the previous chapters that, with the separation of the interaction given in eq. 5.2, the SR contribution is basically originated by the Pauli repulsion in the experimental-relevant distance range. Furthermore, it is partially canceled out by the ES part. Thus, adapting the idea given in [190], here we improve the pair–wise approach used in previous chapter by calculating the SR from a function of the overlap of ρ^{probe} and ρ^{sample} as

$$V_{SR} = V_0 \int \left(\rho^{\text{probe}}(\vec{r}, \vec{R}_{\text{tip}}, \theta, \varphi)\rho^{\text{sample}}(\vec{r})\right)^{\alpha} \mathrm{d}\vec{r}^3. \tag{5.5}$$

Thus, both the ES and SR contribution take into account the details of the charge distribution of both sample and tip. Moreover, in contrast to pair–wise models that require a large number of parameters, this approach only has two non-species dependent parameters (V_0 and α). These are fitted with input data coming from DFT force curves of the most relevant sites of the sample. Furthermore, as we discuss in sec. 5.3.6, for a CO tip the variation of the coefficients from sample to sample is very small. Thus, with little loss of accuracy, a set of universal parameters can be used in the model eliminating the need of the system specific fit.

This description of the SR component is realistic and offers insight into the nature of the interaction between a closed-shell tip and the sample. For the tip–sample distance range most relevant in HR–AFM with CO probes, where Pauli interaction dominates over bonding interactions, the quality of the fit on all the molecules studied in this article is outstanding. This suggests that the Pauli repulsion between two molecules can be, in a classical sense, described by the overlap of their electronic densities. Notwithstanding, this functional form of

the SR interaction is purely repulsive and, at larger distances, cannot reproduce a tip–sample interaction with an attractive SR potential well.

The main input data of the model are ρ^{sample}, ρ^{probe} and ϕ^{sample} used by eq. (5.5) and eq. (5.3). These are extracted on a 3D grid from separate *ab initio* calculations of the sample and the probe. For the latter, the probe is kept in an upright position at $\vec{R}_{\text{tip}} = \vec{0}$. For an arbitrary position $\vec{R}_{\text{tip}}$ and rotation (θ, φ) of the probe, the SR and ES interactions are computed by interpolating ρ^{probe}.

5.2.2 Computational details

First principles calculations

All the DFT calculations were carried out with the PAW method as implemented in VASP [255] with a 600 eV plane–wave cutoff, a 10^{-6} eV accuracy electronic self-consistency loop and the PBE XC functional [209] supplemented by vdW DFT–D3 [223]. A $3 \times 3 \times 1$ Monkhorst-Pack grid was used for the Brillouin zone integration. The dipole correction was applied to the z-direction in order to eliminate ES spurious interactions among the repeated unit cells. This is especially important when calculating the electrostatic potential of the sample.

Before calculating DFT tip–sample interaction curves, the geometrical positions of the molecules were obtained through DFT ionic relaxation using the conjugate gradient algorithm and a $F_{\text{min}} = 0.01$ eV/Å cutoff for the residual forces. The Breitfussin A (bfA) molecule examined in sec. 5.3.3 was relaxed on a 4-layer Cu(111) slab on a (14.51, 12.62, 18) Å cell. The rest of the molecules were relaxed without a substrate.

An isolated CO molecule was used as a model tip. In a CO-metallic tip, the metallic cluster is separated >3 Å from the molecule and does not contribute towards the SR interaction contrast. By the same token, the metallic cluster provide negligible atomic contrast from the vdW and ES interactions on sample that do not have large spatial separation between atomic sites. In particular, a metallic tip generates an electric field with a large spatial extension that averages out the ES contributions of charges that vary at the atomic scale (see chapter 3).

For the tip–sample interaction calculations the substrate was eliminated and

the molecules were frozen to their relaxed positions (on top of the substrate). In HR–AFM imaging with CO tips, the substrate only add a small vdW background that does not change the overall contrast.

In order to reduce the spurious effects coming from interaction with image cells, a large vacuum is used on all the calculations. The N heteroatom six–membered rings examined in secs. 5.3.1, 5.3.2 and 5.3.6 were placed on a (13.06, 11.31, 18) Å cell, the C_{60} molecule studied in sec. 5.3.4 was placed on a (10.57, 11.57, 25) Å cell, and the 8–hq dimer studied in sec. 5.3.5 was placed on a (19.43, 16.82, 18) Å cell.

AFM simulations with the model

The charge density and the electrostatic potential of the tip and the sample were extracted on a uniform 3D mesh of $\lambda \approx 0.075$ Å spacing from separate VASP [255] calculations. The force vs. distance as well as the images simulated with the method used the same cell size and probe (isolated CO molecule) as the DFT calculations (see sec. 5.2.2). For the simulation of maps with CO tilt, the probe position was relaxed using the Broyden-Fletcher-Goldfarb-Shanno (BFGS) algorithm until the generalized gradients were less than 5×10^{-3} eV/Å.

5.3 Results and discussions

5.3.1 Illustration of how the method works: Pyridine molecule

Here, we illustrate the use of the method by simulating images of a pyridine molecule as probed by a CO tip. A pyridine is a benzene ring in which an N atom substitutes a C–H group (see inset of fig. 5.3(a)). First, force curves are calculated with DFT on the most important sites of the molecule: the atoms, the bonds (halfway between bonded atoms) and the center of the ring. The force vs. distance plot for the N atom is shown in fig. 5.3(a) (solid blue line). It has a small attractive regime at large tip–sample distances (z>3.5 Å) and a sharp repulsive one at smaller distances.

The next step is to decompose the total interaction into its ES, vdW and SR components. The first two, as described in sec. 5.2, are obtained from

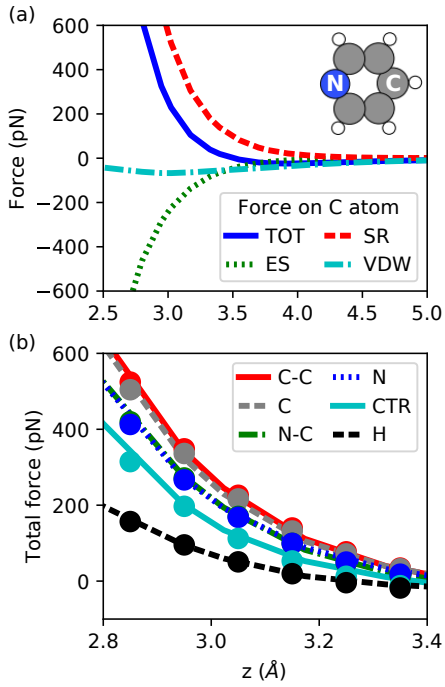

Figure 5.3: AFM spectroscopy of a pyridine molecule with a CO tip. (a) Force decomposition on the C atom opposite to the N atom. (b) Total force as calculated with DFT (lines) and the model (markers) for 6 sites. The C–C site is the midpoint between the C atom opposite to the N and a neighboring C atom. CTR is the center of the molecule. The fit, with a 7.5 pN RMSE, is outstandingly precise.

eq. 5.3 and from a stand–alone DFT–D3 [223] calculation. The SR component is isolated by subtracting the ES and vdW from the total interaction. The decomposed forces, plotted in fig. 5.3(a), help explain the different interaction regimes. At large distances, the attraction sensed by the tip mainly comes from the vdW interaction and, to a lesser extent, from the ES interaction. At short distances, a strong cancellation between the SR and ES interactions leads to a sharp increase of repulsion as the tip–sample distance decreases. As was argued in the previous chapter, this cancellation explains why simple pairwise models to simulate HR–AFM images work qualitatively well.

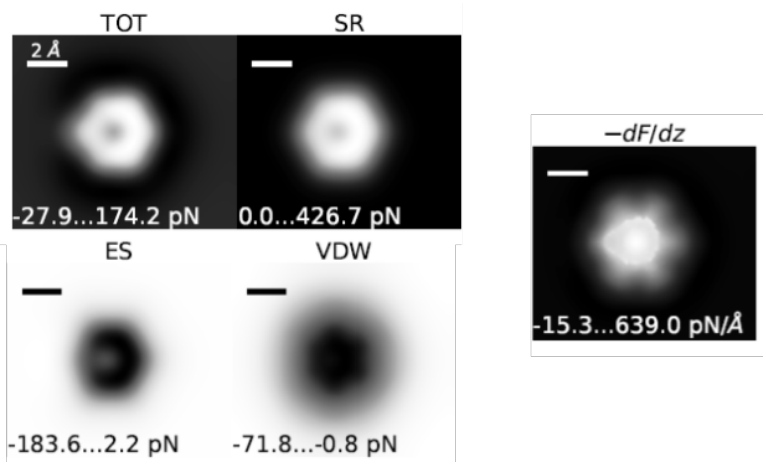

Figure 5.4: HR–AFM images of the pyridine molecule calculated with the model. From left to right: static total, short-range, electrostatic and van der Waals forces and the total force gradient (proportional to the frequency shift) with tip relaxation.

The total force of all the sites used to parametrize the SR interactions are shown in fig. 5.3(b) as solid lines. The C–C bond and the C atom are the most repulsive sites of the molecule, followed by the N–C bond and the N atoms. The least repulsive site is the H atom followed by the center of the molecule. For each force spectroscopy, the SR interaction is isolated as described above. These data points are used to fit V_0 and α of eq. 5.5 by minimizing the RMSE. Fig. 5.3(b) shows the comparison of the forces as obtained with the model (markers) and DFT (lines) using the minimized parameters $V_0 = 13.365$ eV and $\alpha = 1.07$. For these tip–sample distances, the model agrees well with the DFT calculations yielding a RMSE of 7.5 pN. Note that the exponential factor of eq. 5.5 (α) is only slightly larger than one. In other words, the functional form of the SR interaction is almost the pure overlap of the electronic charge densities.

Having obtained a proper fit, AFM maps of the molecule are simulated by calculating the interaction on a 2D grid. Taking advantage of the capability of the model to decompose the forces, the interaction maps are plotted in fig. 5.4 with rigid CO tip (static map) along with the force gradient with a flexible tip (relaxed map) for z=3.1 Å. In the small amplitude limit, the force gradient is

proportional to the frequency shift [5]. The strong cancellation between the SR and ES maps with the addition of a weak vdW attraction results in a static force map that has an asymmetrical hexagonal shape (the atomic geometry has the N atom and C–H groups arranged in a hexagon), with a dark hollow center and a dark hallow around the molecule. The hollow shape in the total force map is a direct consequence of the SR interaction. This contribution is very local and thus, it is stronger when the tip is placed on top of a single atom compared to the center of the molecule. In contrast, the vdW interaction, which has a larger range, provokes the center to be slightly darker. It also exclusively explains the dark hallow around the molecule [40].

As in the force curves, the force maps also clearly show that the C sites are more repulsive than the N site. The ES force on the N atoms is less attractive than on the C atoms, and the vdW is fully symmetric, which leaves the SR as the sole responsible interaction for the N atom to be less repulsive than the C atom. However, the N atom has more valence electrons than the C atoms. Thus, naively, we would expect greater repulsion on the N site compared to the C sites. In sec. 5.3.2 this will be explained in terms of the decay of the charge densities associated with the local environment of the atomic species.

The asymmetry of the hexagonal shape of the total interaction map is not limited to the difference in force between the C and N atoms, but also to the locations of their respective maxima, with the N atom having a slightly more extended vertex than the C–H groups. The flexibility of the CO tip enhances this effect in the frequency shift image by sharpening the saddle lines of the static maps. The effect will be explained in sec. 5.3.2 in terms of the lateral extension of the lone-pair of the N atom. Although these asymmetries are typically observed in experimental images [144, 148, 149, 171], pair–wise models, which tend to produce more rounded shapes, have a hard time reproducing them.

5.3.2 Can the AFM images be predicted simply in terms of the stoichiometry?: 6–membered rings

Insight into the imaging mechanisms of the closed-shell probes can be gained by comparing the pyridine molecule with the rest of the N atom 6–membered

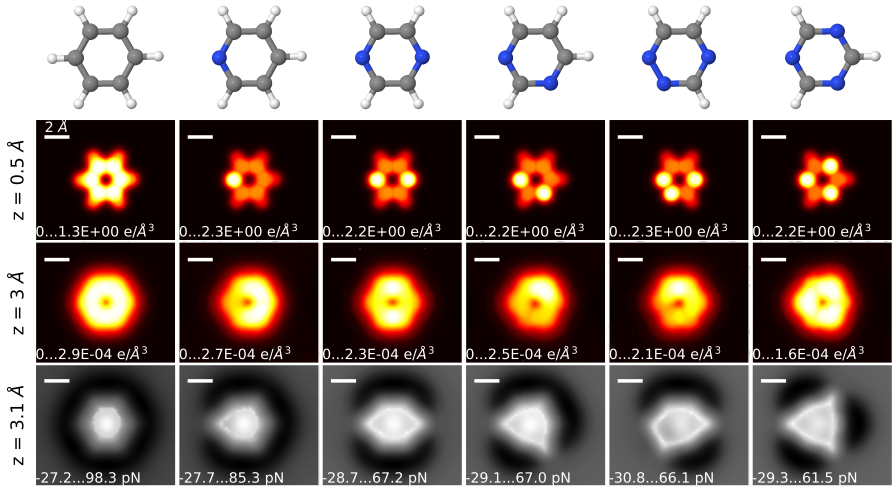

Figure 5.5: Six-membered rings with N heteroatoms. From left to right: benzene, pyridine, pyrazine, pyrimidine, 1,2,4–triazine and an s–triazine. From top to bottom: schematic representation of molecules, charge density 0.5 Å and 3 Å from the plane of the molecules and total force maps z=3.1 Å.

heterocyclic compounds [261] (and the benzene molecule). Although we simulated all the molecules in this group, for simplification and because the results for the rest of the molecules in the group are similar, we only show results for 5 molecules: benzene which has no heteroatoms, pyrazine which has one N heteroatom, pyrazine and pyrimidine both with two N heteroatoms, and 1,2,4-triazine and 1,3,5-triazine (hereafter s–triazine) both with three heteroatoms. The first row of fig. 5.5 displays a schematic representation of the molecules. On all the rings, the optimized system-specific parameters (V_0 and α) have similar values (see table 5.1). The AFM force maps (with tip relaxation) simulated with the model are shown in the last row of fig. 5.5. They have a rich behavior that can be correlated with the charge density of the molecule at different planes (see the second row of fig. 5.5 for ρ^{sample} at a plane 0.5 Å above the molecule and the third row of fig. 5.5 for ρ^{sample} at a plane 3 Å above the molecule).

The counterintuitive asymmetry in the force maps of the pyridine molecule described in the previous section can be easily explained by examining the charge

molecule	V_0 (eV)	α
Benzene	14.484	1.08
Pyridine	13.365	1.07
Pyrazine	13.534	1.07
Pyrimidine	13.549	1.07
1,2,4-Triazine	13.725	1.07
s-Triazine	15.221	1.08
Universal Parameters	13.928	1.073
bfA	12.413	1.07
C_{60}	13.491	1.07
8–hq	22.012	1.12

Table 5.1: Parameters used by eq. 5.5 to compute the SR interaction.

density of the molecule. The N atom, having more valence electron than the C atoms, have a larger charge density close to the plane of the molecule. However, the charge density of the N atom has a faster decay with the distance than the one of the C atoms, resulting in less charge density at the z=3 Å plane. At this plane, the charge density (third row in fig. 5.5) accumulates in the C–C bonds because the energetically favorable π orbitals of these bonds decay slower and have greater extension than that of the N–C (and N-N bonds). This explains why the N atom exerts a less repulsive force to the tip than the C atom. The overlap of the CO's wave function and the molecule is greater when the tip is on top of a C atom or C–C bonds.

The charge density behavior described above is the similar for all 6–membered rings with N heteroatoms with an extreme case occurring in the s–triazine. This molecule lacks C–C bonds, and thus there is no charge accumulation near the C atoms. Even at the far z=3 Å plane, the charge densities of the N atoms remain larger (decay slower) than the ones of the C atoms. This result suggests that the charge density is related with the molecular orbitals, determined not only by the chemical species but also by the molecular structure. In other words, not only structurally similar molecules with different stoichiometry provide qualitatively

different AFM images [144], but that the chemical environment (i.e., bond structure) is also important. This is most evident in the pyrimidine molecule which has three C atoms with C–C bonds and one C atom without. The latter has the least charge density (even compared to the N atom) and exerts the weakest repulsive force.

As with the pyridine, the rest of the N heteroatom 6–membered rings' AFM images have sharper vertices around the N atom as compared to the C–H groups. The asymmetries can be traced back to the charge density of the molecules. Far from the plane of the molecule (z=3 Å), the charge density overflows laterally the N atoms more than the C–H groups. This is in turn reflected on the SR interaction but not on the ES interaction. The strong cancellation leaves a PES whose saddle lines connect past the N atoms and deform the hexagon symmetry of the molecules. The tip tilt, which highlights the saddle lines of the PES, highlights the asymmetry of the charge density around the N atoms.

All the features described above are highly dependent on subtle effects of the charge density and thus are hard to capture with pair–wise models. First, contrary to experiments [127, 144, 148, 149, 171], pure pair–wise model tend to produce round vertices. Second, it would require more sets of parameters than species of atoms. In order to accommodate the difference between C atoms with and without C–C bonds different C species would need to be defined. Additionally, the subtle effects in the difference of the extensions of the vertices between the N and C atoms, which is independent of the relative magnitude of force at the atomic site, would require a large number of ghost species and a complex parametrization procedure.

5.3.3 Can the model deal with very different chemical species?: Breitfussin molecule

In the previous sections we examined several planar hexagonal rings composed of N and C–H groups. On these systems, DFT calculations of the tip sample interactions are reproduced well by the model using SR parameters that are very similar. The question arises, is the model valid for more complex atomic geometries and a large number of chemical species? To this end we examine

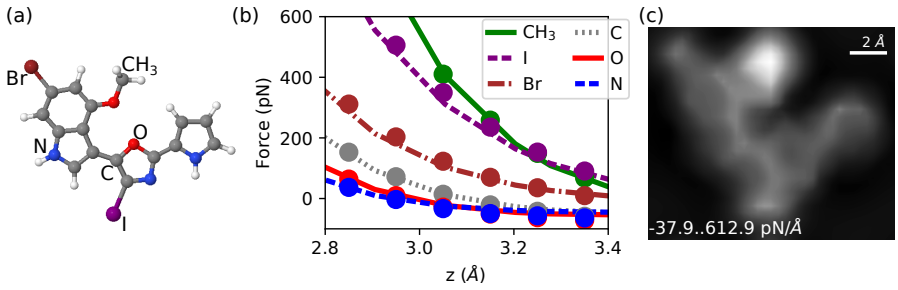

Figure 5.6: Simulated images of a bfA molecule which has 6 distinct atomic species. (a) Schematic representation of the molecule. (b) Total force as calculated from DFT (lines) and the model (markers) on 6 sites. (c) Force gradient (proportional to the frequency shift) image simulated with the model at z=3.1 Å showing a striking resemblance with experimental images reported in [117].

the bfA molecule (see fig. 5.6(a)), a halogenated natural product discovered it the Arctic hydrozoan Thuiaria breitfussi and characterized with the assistance of AFM experiments [117]. With 6 different chemical species, including halogens and electronegative atoms, the molecule has a polar charge distribution and is ideal to test the capabilities of the model. In addition, the molecule has a non-planar geometry upon the adsorption on the substrate, especially the CH_3 group that intrinsically has a non-planar form.

Prior to the calculations, the atomic positions of the molecule were obtained by relaxing the molecule on top of a Cu(111) slab. DFT calculations for the tip–sample interaction on all the atomic positions, the bonds, and the centers of the rings were used to parametrize the model. Fig. 5.6(b) shows a comparison between the model (markers) and DFT calculations (lines) for a subset of these sites. The minimized parameters $V_0 = 12.413$ eV and $\alpha = 1.07$ are very close to the parameters used in the previous sections and reproduce well DFT results (with a RMSE=24.8 pN). The simulated frequency shift of the molecule (see fig. 5.6(c)) is strikingly similar to images obtained experimentally on a Cu(111) substrate [117], showing the CH_3 as the brightest feature, a faint silhouette of the rings and an elongated oval around the I atom. However, because the the molecule is kept frozen in the simulations, the repulsion of the CH_3 group is overestimated and it reduces the overall contrast on the rest of the features.

In addition, the calculations corroborate that the bright feature in the lower right part of the experimental image (and absent in the calculations) is an experimental artifact [117].

These results show that the model is capable of dealing with different chemical species and atomic geometries with no need to account for them explicitly in the formulation of the model. Whereas a pair–wise model based on Morse potentials would need at least 18 parameters (3 $\times$ the number of species) to determine the tip–sample interaction, this model only needs 2, independent of the number of species. Furthermore, the parameters that are used in this complex molecule are fairly similar to the parameters used in the previous sections for simpler molecules containing only N and C–H groups (see table 5.1 for a comparison). This opens the door to the possibility of using universal parameters on all the molecules and thus eliminating the need for the costly SR fitting. This will be explored in sec. 5.3.6.

5.3.4 Capturing differences in bond order: C_{60} molecule

The capability to distinguish subtle effects associated with the order of covalent bonds is an important goal for the NC–AFM. Experimental studies suggest that, using closed-probe shell probes, the AFM is capable of distinguishing the order of C–C covalent bonds [54, 119]. pair–wise models whose parametrization depend on the atomic species of the sample and probe cannot reproduce experimental features that are intrinsic to the accumulation of charge in the bond. Thus, these models must either introduce artificial ghost species in the parametrization, for instance at the bonds, or artificially increase the ES interaction [61] in order to incorporate bond-order discrimination into the model.

Our method, which does not use a pair–wise description for the SR interaction, is able to pick up these effects directly as a collective property of the charge density. We calculated this on the C_{60}, a molecule with twenty hexagons and twelve pentagons with C atoms on each vertex (see fig. 5.7(a)). The structural asymmetry of the C arrangement induces alternating single C–C bonds at the links between two hexagons (h) and double C–C bonds at the links between hexagons and pentagons (p). The motivation of studying this system is two fold.

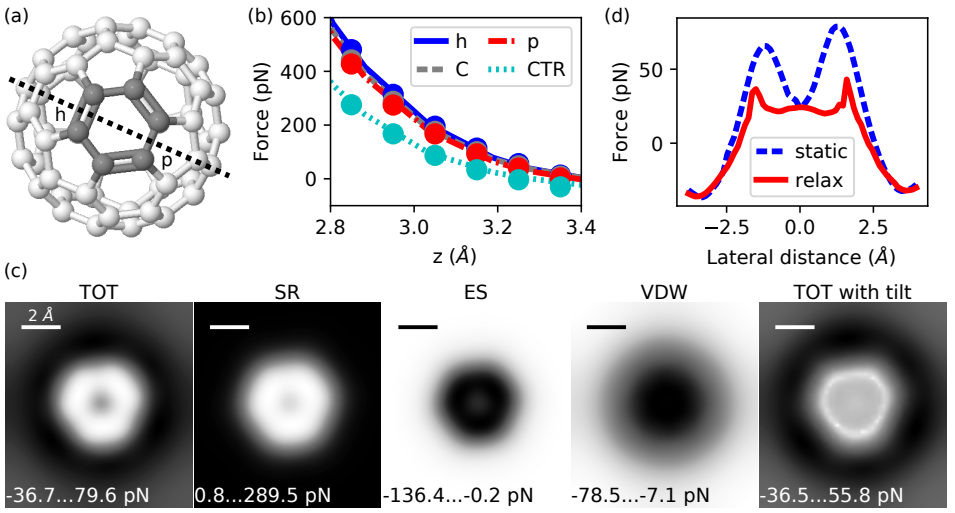

Figure 5.7: Simulated images of a C_{60} molecule which has distinct bond orders. (a) Schematic representation of the molecule with the hexagon facing upwards. (b) Total force calculated with DFT (lines) and the model (markers) for 4 sites. The h sites is for the bond fusing two hexagons and the p site is for the bond fusing a pentagon and a hexagon; the h bond has a larger bond order then the p bond. CTR is the center of the hexagon. (d) Force profiles along the line passing through the p and h bonds with the CO tip fixed in the upright position (dashed blue line) and allowed to relax (solid red line). (c) Force maps for z=3.1 Å. From left to right: static total, short-range, electrostatic and van der Waals and the total force with a flexible tip. With the model, bond order discrimination obtained with a CO tip is attributed to the short-range interaction.

First, to test whether the model developed in this chapter is able to distinguish between bond orders without explicitly accounting for them in the parametrization (as a different functional form of the SR interaction) or without artificially increasing the ES contribution. Second, to pinpoint the underlying interaction that makes the AFM capable of probing such subtle effects.

DFT force curves on a C atom, a single bond (p), a double bond (h), and the center of the hexagon (CTR) were used to parametrize the model. Fig. 5.7(b) shows a comparison between the model (markers) and DFT calculations (lines).

The minimized parameters $V_0 = 13.491$ eV and $\alpha = 1.07$ are again very close to the parameters used in the previous sections and reproduce well the DFT results (with a RMSE=6.6 pN). Already from the force spectroscopy, it is apparent that the double bond exerts a greater repulsion on the probe than both the C atom and the single bond. The least repulsive site is the center of the hexagon. From the force maps at z=3.1 Å shown on fig. 5.7(c) it is evident that the high repulsion of the h site is distributed along the whole bond (line joining the C atoms) and that the image has a triangular shape with vertices on the h sites. Although there is a strong cancellation between the SR and ES interaction, the former is clearly responsible for the shape of the static map. The difference between the SR forces at the h and p sites breaks the hexagonal symmetry of the atomic geometry. The relaxation of the CO probe highlights the saddle lines in the PES and shortens the distance of the double bond compared to the single bond [119] (see last column in fig. 5.7(c)). Although the tilt slightly saturates the total force along the bonds, the force on the the h site remains larger than on the p site. This can be seen in fig. 5.7(d) where a profile at z=3.1 Å going from the p to the h site is plotted with the CO probe is kept fixed (static) and allowed to tilt (relax).

These results are consistent with the experimental findings that a CO probe is able to discriminate bond orders on the C_{60} molecule [119]. It also unambiguously determines that the SR interaction, through the charge density of the sample, is the underlying interaction responsible for discrimination. Finally, it shows that our method is able to model subtle collective effects coming from the charge density.

5.3.5 Imaging H–bonds: 8–hq

There is an ongoing discussion in the SPM literature with respect to the imaging of H–bonds [66, 123, 127, 162, 163, 165, 166]. In AFM, inter–molecular features associated with weak bonds have been observed with CO tips [123, 132, 146, 155, 160] and other molecular tips [66, 161]. The imaging of the features might be, as we have seen with the bond-order discrimination, a direct observation of the bonds, i.e., charge redistribution effects, or an artifact that results from the

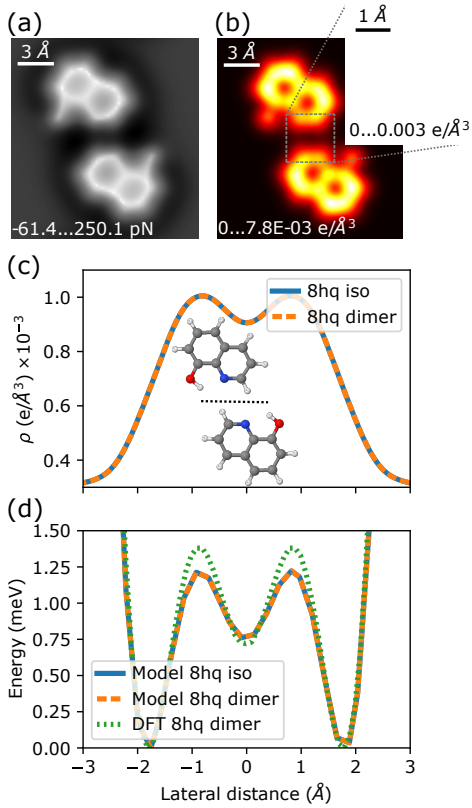

Figure 5.8: Simulated images of an 8–hq dimer. (a) Force map at z=3.1 Å. (b) Charge density at a plane 3.1 Å above the molecule. (c) Charge density profile in the inter–molecular region for two isolated molecules and the dimer. (d) Energy profile along the inter–molecular region for two isolated molecules (solid blue line) and the dimer (dashed orange line) as calculated with the model and obtained from DFT calculations (dotted green line). The inter–molecular contrast of the AFM images is due to the overlap of the wavefunctions of N and C–H sites with no apparent enhancement due to the formation of H–bonds.

enhancement of the PES due to the mobility of the probe Here we show that charge redistribution effects in such H–bonded systems are minuscule and not detectable by AFM. Rather, their imaging is made possible by the PES formed by the overlap of the wave functions of the atoms that constitute the H–bond.

In the previous section we showed that our model is able to reproduce sub-

tle experimental intra–molecular features associated with the bond orders of molecules and that arise as collective effects in areas with high charge density. The SR description used in this chapter describes well DFT tip–sample interactions at close distances, where the overlap between the charge density of the sample and the tip is large. Thus, it is not trivial whether such description can pick up subtle effects coming from low density regions such as weak inter–molecular bonds. However, we will demonstrate that, by giving greater weight in the fitting to the inter–molecular region, our method is indeed able to model these regions and to reproduce the DFT tip–sample interactions. Furthermore, in addition to studying the 8–hq dimer, our method allows us to study a fictitious system with two 8–hq molecules in the atomic configuration of the dimer, but without their H–bonds In contrast to standard DFT, our model uses static charge distributions and thus, we can create an artificial sample from the charge distribution of the two isolated 8–hq molecules. This allows us to quantify the charge redistribution that occurs upon the formation of an H–bond and, by isolating its effect on the contrast formation, to explain the origin of the inter–molecular features observed in HR–AFM images.

The 8–hq is a simple organic molecule derived from a heterocycle quinoline and an OH group. Two 8–hq molecules, or an 8–hq dimer, bind via H–bonds. In order to simulate the dimer with our model we first fit with special care of the inter–molecular regions the two parameters that determine the SR interaction. These regions have small charge density and thus the overlap of eq. 5.5 is small Thus, in the fitting, more weight is given to the inter–molecular region, by only using sites adjacent to the H–bonds: the atoms around the H–bonds (O, N, C, and two H atoms) and their corresponding covalent bonds, an H–bond site (mid point between the N atom of one molecule and the corresponding H atom of the other molecule), and the mid point between the two H–bonds. This provokes the SR parameters (V_0 and α) to deviate slightly from the ones used in the rest of the molecules studied in this chapter (see table 5.1). Notwithstanding, the model describes well DFT force curves and energy line profiles on the inter–molecular region with little loss of precision on the molecular regions (RMSE 9.5 pN). Fig. 5.8(d) shows a comparison between DFT results (dotted green

line) and the model's results (dashed orange line) for a line profile of the 8–hq dimer transverse to the H–bonds.

We simulate the 8–hq dimer with our model (see fig. 5.8(a)) and observe the silhouette of the two rings and OH group of each molecule as well as the two weak inter–molecular features associated with the H–bonds. These are much fainter than the lines highlighted by the CO tilt across the covalently bonded atoms. The results are consistent with experimental images presented in the literature [123].

In order to explain the origin of the inter–molecular features observed in the experiments, we first calculate the charge density of the sample. Fig 5.8(b) presents a slice of the charge density at a plane z=3.1 Å above the dimer. The inset shows a zoom in the inter–molecular region. A clear union in the charge density of the molecules can be observed in the line joining the molecules through the H–bonds. The question is whether this is due to the charge redistribution that occurred in the formation of the H–bonds or it is simply the overlap of the charge density of the isolated molecules. Fig 5.8(c) shows a profile of the charge density across the transverse of the H–bonds for the dimer (dashed orange line) and the sum of the charge densities of the isolated molecules (solid blue line). Clearly, any charge redistribution that occurred in the formation of the dimer ($\delta\rho$) is not apparent in this scale.

To further discard the thesis of direct H–bond observation in HR–AFM, we compared images obtained with the model of the 8–hq dimer and a fictitious system where the charge density of the two molecules was obtained from isolated DFT calculations and then added together. There was no apparent difference between the images. This is evident in fig. 5.8(d) where a line profile of the energy across the transverse of the H–bonds for the dimer (dashed orange line) and the fictitious isolated molecules (solid blue line) is presented. Again, there is no apparent effect that originates directly from the H–bonds. Such a comparison rules out effects of minuscule charge redistribution ($\delta\rho$) that arise in the formation of the H–bond and not observed in the scale of fig. 5.8(c). Note that at a plane closer to the molecule $\delta\rho$ increases significantly, however, these regions are not probed by the AFM. Thus, the decay of the charge density of the

isolated molecules in the inter–molecular regions [165] that produce the PES of the probe is responsible for the inter–molecular features observed in these regions.

5.3.6 Universal parameters

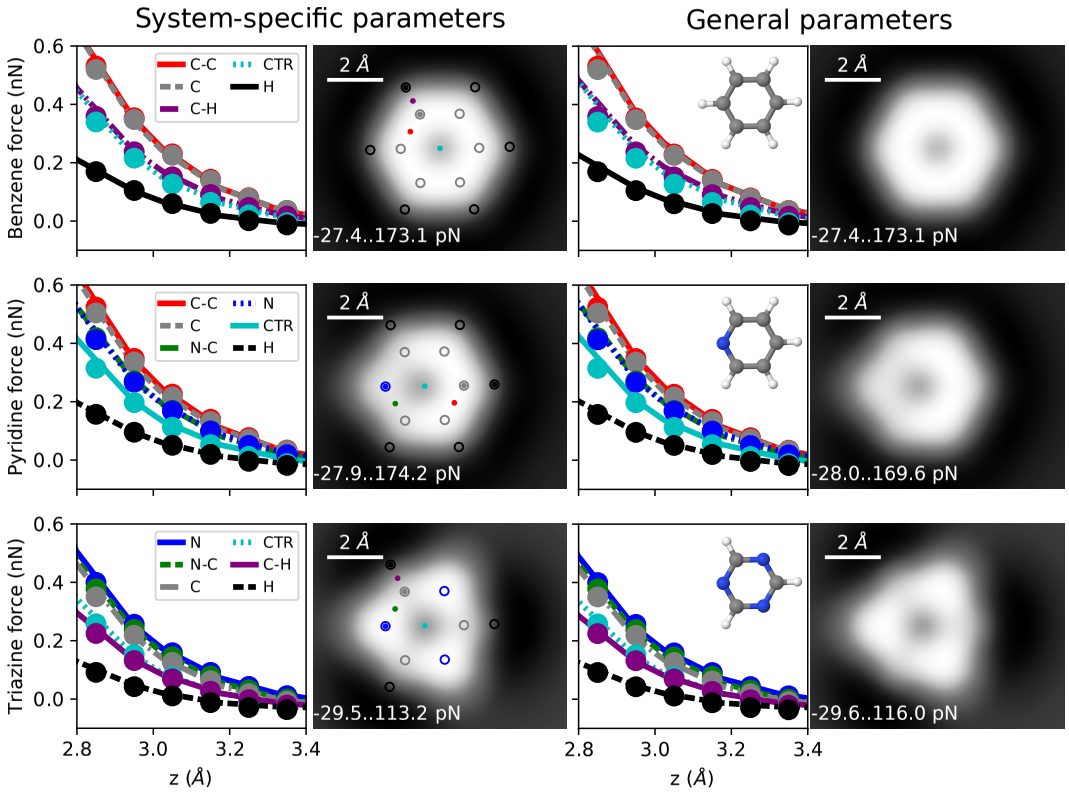

Figure 5.9: Comparison of simulations performed with system-specific parameters and general parameters. The force maps are calculated at z=3.1 Å. For the six-membered rings with N heteroatoms, the results are quantitatively similar: the average RMSE increases by 65%.

For all the systems studied so far, the V_0 and α parameters used by the SR interaction and fitted from DFT calculations were very similar. The question becomes, can universal parameters be used to simulated images at least for obtaining qualitative results? This is twofold important. From a practical point of view, the avoidance of fitting the parameters with DFT calculations saves time. For a given tip ρ^{tip} only needs to be calculated once and the model would only require ρ^{sample} and ϕ^{sample} of the isolated sample. This is the equivalent of the TH approach used to simulate STM images where ρ^{sample} is the only required *ab initio* input for a calculation. Additionally, the use of universal parameters for the SR interaction gives insight into the underlying interaction and their manifestation in the classical sense. To this end, we revisit the N heteroatom 6–membered rings and simulate images of the molecules using universal parameters $V_0 = 13.928$ eV and $\alpha = 1.072$ obtained by averaging the SR parameters of all the molecules studied in sec. 5.3.2.

Fig. 5.9 shows a comparison of static force vs. distance plots and static force maps simulated using system-specific parameters and universal parameters. The figure shows simulations for the benzene, pyridine and s–triazine molecules and, as with the system-specific parameter simulations, the force curves obtained from the universal parameters agree quantitatively with the DFT calculations of the tip–sample interaction. The average of the RMSE of all 6–membered rings increases from 7.3 pN using the system-specific parameters to 12.0 pN using the universal parameters. Likewise, there are no appreciable difference between the static force maps obtained from the two sets of parameters. This points to an universality of the model to simulate AFM images and the description of the SR interaction between the sample and closed-shell probes.

5.4 Conclusions

We developed a model to simulate HR–AFM images with DFT accuracy that only depended on charge density and electrostatic potential of the tip and the sample in their isolated configurations. The mobility of a flexible probe is taken into account in the simulation of interaction maps by including a penalization spring potential and by rotating the charge density of the probe. It decomposes

the interaction into an ES, vdW and SR contribution with the last having no pair–wise parametrization. Rather, the SR component is calculated from the overlap of the charge densities of the tip and the sample with a functional form that only has two parameters, independent of the number of species in the systems and the complexity of the bonding topology. These parameters are fitted to system specific DFT tip–sample interactions on the most relevant sites of the sample. However, the parameters are so similar that by averaging several systems, they can be made universal. This eliminates the costly work of performing system specific DFT force curves.

The use of the model is illustrated on the pyrazine molecule whose results reaffirm the importance of the strong cancellation between the SR and ES interactions that was uncovered in the previous chapter. We simulate 4 additional systems that are very important in the literature and, with them, not only test the capabilities of the model, but also offer new insight into the underlying interactions of the NC–AFM.

We perform simulations of 6–membered rings with N heteroatoms and obtain maps that are qualitatively consistent with experimental images presented in the literature. In these molecules we analyze how the local environment of the C atoms and the slow decay of the wave function of the N atoms due to its lone-pair affects the charge density of the molecule and, in turn, the simulated AFM images. Thus proving that, not only structural similar molecules with different stoichiometry provide qualitatively different AFM images [144], but that the chemical environment (i.e., bonding structure) is also important.

The capabilities of the model to handle a molecule with a large number of chemical species and a non-planar geometry is tested with the complex bfA molecule. In this halogenated natural product the model reproduces well DFT tip–sample interactions and provides AFM frequency shift maps that are qualitatively similar to experimental ones [117]. In contrast to pair–wise methods whose number of parameters scale with the number of species, in this case at least 6, the current method successfully simulates the molecule with only 2 parameters, independent of the number of chemical species.

The model is also able to pickup subtle intra–molecular features associated

with the covalent bond orders in molecules. On the C_{60} molecule, the asymmetry of a given hexagon phase is broken by the neighboring atoms giving rise to alternating single and double bonds. Our AFM simulations on this system not only reproduce qualitatively experimental images [119] but also pinpoints the SR as the underlying interaction responsible for the discrimination. The model pickups up these subtle collective effects directly from the charge density of the sample.

With a small modification of the SR parameters, inter–molecular features associated with weak bonds also appear in our simulations. Simulations of an H–bonded 8–hq dimer are in agreement with DFT tip–sample interactions as well as experimental images [123]. We settle the controversy present in the literature on the underlying mechanisms that is responsible for the imaging of these features by quantifying as minuscule the effects of charge redistribution that occurs upon the formation of the H–bond. This leaves the overlap of the wave functions of the atoms that constitute the H–bond as the source of repulsion that generates a PES whose saddle lines are highlighted by the mobility of the probe and, in turn, lead to the appearance of the inter–molecular features in NC–AFM images.

6 General conclusions

The NC–AFM is an indispensable tool in nanocience to study surfaces and molecules at the atomic scale. However, the interpretation of the images is complicated and the underlying mechanism to form the contrast hard to discern. In close collaboration with experimental teams from universities and research centers, and with the aid of cutting–edge theoretical methodology developed in this work, we tackle important open questions in the literature related to the contrast mechanisms of the NC–AFM.

In this work we developed three different methods to explain the contrast formation in AFM images. In their own way, these methods overcome the practical limitations of DFT, the golden standard approach in surface science, in their application to large systems, but retaining its accuracy. The multiscale model developed in chapter 2 made it possible to simulate macroscopic areas of deformations ($\sim 10^9$ atoms). While standard DFT is capable of simulating ~ 1000 atoms, the high accuracy parameters required to describe the subtle topographic variations of the moiré with ionic relaxations would require vast computational resources for this limited number of atoms. The methods developed in chapters 3-5 to simulate HR–AFM images with CO tips helped overcome a different barrier related to the speed of the calculations. Our methods are 2–3 orders of magnitude quicker than DFT, yet they retain DFT accuracy. This makes feasible the creation of theoretical images that include tip relaxation on a routinely basis.

In chapter 2 we studied the low corrugated G/Pt(111) surface as a model system for weakly coupled 2D materials. We showed that large amplitude cantilver based NC–AFM experiments not only achieve atomic resolution in the topogra-

phy and dissipation images, but resolve the moiré pattern induced by the G–Pt interaction. To explain this, we developed a novel multiscale model, based on DFT calculations, where the energy cost of both global and local deformations of the graphene layer competes with short–range chemical and long–range van der Waals interactions. We showed that the dissipation is due to the adhesion of graphene to the apex upon tip retraction which induces deformations on large–scale areas of graphene. We demonstrate that the AFM is able to measure the mechanical properties of individual atoms and that atom–by–atom stiffness differences are responsible for the moiré pattern observed both in the attractive and repulsive regimes. Therefore, our results open a new route to explore the local mechanical properties of low–dimensional weakly coupled systems.

In chapter 3 we carried out a comprehensive study of the electric field of CO terminated tips and its influence on the contrast formation of high–resolution images of surfaces. We combined small amplitude NC–AFM images of Cl vacancies in a NaCl(100) bilayer along with a theoretical method developed to simulate interaction decomposed high–resolution images with an accurate description of the electrostatic interaction. Our main conclusion is that the electrostatic field of the CO–metal tip can be represented by the sum of a dipole field that takes into account the positive charge accumulation at the metal apex due to the Smoluchowski effect, and the electrostatic field of an isolated CO molecule, that exhibits negative charge accumulation in front of the oxygen atom due to its lone pair. The interplay of these fields, with an opposite sign in the near–field and rather different spatial extension, explains the contrast evolution observed in the experiments and reconcile apparently contradictory claims in the literature about the nature of the electrostatic field of CO tips. This insight also has important implications for the understanding of the enhanced contrast in several SPM techniques that use CO probes.

In chapter 4 we studied the contrast formation of images of molecules with CO functionalized tips. Using a triazine self–assembled monolayer (SAM) on graphene as a model system, we showed that when probed with closed–shell probes, there is a strong cancellation between the short–range and electrostatic contributions, with the former dominating at close tip–sample distances and the

latter being more relevant at large distances. The strong cancellation reduces 3D averaging effects on each interaction and explains why the total interaction resembles the charge density at small tip–sample distances and the z–component of the electric field at large distances. It also explains why simple pair–wise point–like models qualitatively reproduce the contrast observed in the experiments. We also demonstrated the existence of different minima in the 3D potential energy landscape of the mobile tip in the SAM.

In chapter 5 we extended the study of molecules by developing a simulation method that put on equal footing the electrostatic and short–range interactions and removing complex parametrization procedures. The method displays AFM images, as the Tersoff–Hamann method does for STM. This was done by modeling the short–range interaction as the overlap of the charge densities of the tip and sample. This treatment of the short–range interaction allowed us to deal with several problems pertaining to the subtle effects of the charge density of the sample. With a set of N heteroatoms six–membered rings we proved that, not only structural similar molecules with different stoichiometry provide qualitatively different AFM images, but that the bonding structure is also important. With this method we address in a unique way the effect of the charge redistribution that occurs upon the formation of H–bonds in 8-hq dimers on the appearance of intra–molecular features. The method is also able to reproduce bond–order discrimination experimental results on the C_{60} molecule directly from the charge density of the sample via the short–range interaction. Finally, the capabilities of the method to handle a molecule with a large number of chemical species and a non–planar geometry was tested by simulating images of the complex Breitfussin A molecule. This powerful method opens the door to performing rapid and accurate simulations for molecular identification where subtle features in the images are used to differentiate similar molecules.

In summary, this work presents a comprehensive study on the contrast formations of NC–AFM images that capture details that go beyond atomic resolution. In particular, we studied the mechanism for atomic–scale dissipation in weakly coupled 2D materials and the precision limits of the AFM to capture tiny topographic variations of the sample and to probe locally their mechanical properties.

We also studied the interplay between the short–range, electrostatic, and van der Waals interactions, on the contrast formation of high–resolution images captured with functionalized tips. With this, we uncovered the mechanisms for the formation of intra– and inter–molecular features.

Conclusiones generales

El NC–AFM es una herramienta indispensable en la nanociencia para estudiar superficies y moléculas a escala atómica. Sin embargo, la interpretación de las imágenes es complicada y el mecanismo subyacente de la formación del contraste difícil de discernir. En estrecha colaboración con equipos experimentales de universidades y centros de investigación, y con la ayuda de la metodología teórica de vanguardia desarrollada en este trabajo, abordamos importantes problemas abiertas en la literatura relacionada con los mecanismos de contraste del NC–AFM.

En este trabajo desarrollamos tres métodos diferentes para explicar la formación de contraste en imágenes AFM. A su manera, estos métodos superan las barreras de Teoría del Funcional de la Densidad (DFT), que es la herramienta estándar utilizado en la ciencia de superficies. En este trabajo desarrollamos tres métodos diferentes para explicar la formación de contraste en imágenes AFM. A su manera, estos métodos superan las limitaciones prácticas de DFT, el estándar de referencia en la ciencia de la superficie, en su aplicación a sistemas grandes, pero conservando su precisión. El modelo multiescala desarrollado en el capítulo 2 hizo posible simular áreas macroscópicas de deformaciones ($\sim 10^9$ atoms). Mientras que el DFT estándar es capaz de simular ~ 1000 átomos, los parámetros de alta precisión requeridos para describir las sutiles variaciones topográficas del moiré con relajaciones iónicas requerirían demaciados recursos computacionales para simular este número limitado de atoms. Los métodos desarrollados en los capítulos 3-5 para simular imágenes HR-AFM con puntas de CO ayudaron a superar una barrera diferente relacionada con la velocidad de los cálculos. Nuestros métodos son de 2 a 3 órdenes de magnitud más rápidos

que DFT, pero conservan la precisión DFT. Esto hace factible la creación de imágenes teóricas que incluyen la relajación de la punta de manera rutinaria.

En el capítulo 2 estudiamos la superficie de baja corrugado G/Pt(111) como un sistema modelo para materiales 2D débilmente acoplados. Mostramos que los experimentos NC–AFM basados en micropalancas de amplitud grande no solo logran una resolución atómica en la topografía y las imágenes de disipación, sino que también resuelven el patrón de moiré inducido por la interacción G-Pt. Para explicar esto, desarrollamos un nuevo modelo multiescala, basado en cálculos DFT, donde el costo energético de las deformaciones globales y locales de la capa de grafeno compite con las interacciones químicas de corto alcance y de van der Waals de largo alcance. Mostramos que la disipación se debe a la adhesión del grafeno al vértice de la punta tras la retracción de esta, lo que induce deformaciones en las áreas de grafeno a gran escala. Demostramos que el AFM es capaz de medir las propiedades mecánicas de los átomos individuales y que las diferencias de rigidez átomo–por–átomo son responsables del patrón moiré observado tanto en los regímenes atractivo como repulsivo. Por lo tanto, nuestros resultados abren una nueva ruta para explorar las propiedades mecánicas locales de los sistemas débilmente acoplados de baja dimensión.

En el capítulo 3 llevamos a cabo un estudio exhaustivo del campo eléctrico de las puntas terminadas en CO y su influencia en la formación del contraste de imágenes de alta resolución de superficies. Combinamos imágenes de NC–AFM de baja amplitud de vacantes de Cl en una bicapa de NaCl(100) junto con un método teórico desarrollado para simular imágenes de alta resolución con una descripción precisa de la interacción electrostática. Nuestra principal conclusión es que el campo electrostático de la punta CO–metal se puede representar por la suma de un campo dipolo que tiene en cuenta la acumulación de carga positiva en el ápice del metal debido al efecto Smoluchowski, y el campo electrostático de un la molécula de CO aislada, que exhibe acumulación de carga negativa en frente del átomo de oxígeno debido a su par solitario. La competición de estos campos, con un signo opuesto en el campo cercano y una extensión espacial bastante diferente, explica la evolución del contraste observada en los experimentos y reconcilia afirmaciones aparentemente contradictorias en la literatura sobre la

naturaleza del campo electrostático de las puntas de CO. Esta idea también tiene implicaciones importantes para la comprensión del contraste en varias técnicas de SPM que usan sondas de CO.

En el capítulo 4 estudiamos la formación del contraste de imágenes de moléculas con puntas funcionalizadas con CO. Usando una monocapa autoensamblada de triacina (SAM) en grafeno como sistema modelo, demostramos que cuando se escanea con sondas de niveles cerrados, hay una fuerte cancelación entre las contribuciones de corto alcance y electrostáticas, con el primero dominando a distancia cercanas y el segundo a lejanas. La fuerte cancelación reduce los efectos de promedio de 3D en cada interacción y explica por qué la interacción total se asemeja a la densidad de carga a distancias cercanas y a la componente z del campo eléctrico a distancias lejanas. También explica por qué los modelos sencillos de interacciones a pares reproducen cualitativamente el contraste observado en los experimentos. También demostramos la existencia de diferentes mínimos en la superficie de energía potencial 3D de la punta móvil en la SAM.

En el capítulo 5 ampliamos el estudio de las moléculas mediante el desarrollo de un método de simulación que da igual énfasis a las interacciones electrostáticas y de corto alcance y elimina los complejos procedimientos de parametrización. El método muestra imágenes AFM, como lo hace el método Tersoff-Hamann para STM. Esto se hizo modelando la interacción de corto alcance como la superposición de las densidades de carga de la punta y la muestra. Este tratamiento de la interacción de corto alcance nos permitió tratar varios problemas relacionados con los efectos sutiles de la densidad de carga de la muestra. Con un conjunto de heteroátomos de nitrógeno de seis miembros, demostramos que no solo las moléculas estructurales similares con diferente estequiometría proporcionan imágenes de AFM cualitativamente diferentes, sino que la estructura de enlaces también es importante. Con este método abordamos de una manera única el efecto de la redistribución de carga que se produce en la formación de enlaces H en dímeros de 8-hq sobre la aparición de rasgos intra–moleculares. El método también puede reproducir resultados experimentales de diferenciación de orden de enlace covalentes en la molécula C_{60} y que están relacionados directamente con la densidad de carga de la muestra a través de la interacción

de corto alcance. Finalmente, las capacidades del método para manejar una molécula con un gran número de especies químicas y una geometría no plana se probaron simulando imágenes de la molécula Breitfussin A. Este poderoso método abre la puerta a la realización de simulaciones rápidas y precisas para la identificación molecular, donde las características sutiles de las imágenes se utilizan para diferenciar moléculas similares.

En resumen, este trabajo presenta un estudio exhaustivo sobre la formación de contraste de las imágenes de NC–AFM que capturan detalles que van más allá de la resolución atómica. En particular, estudiamos el mecanismo para la disipación a escala atómica en materiales 2D débilmente acoplados y los límites de precisión del AFM para capturar pequeñas variaciones topográficas de la muestra y para explorar localmente sus propiedades mecánicas. También estudiamos la competición entre las interacciones de corto alcance, electrostáticas y de van der Waals, sobre la formación de contraste de imágenes de alta resolución capturadas con puntas funcionalizadas. Con esto, identificamos los mecanismos para la formación de rasgos intra– e inter–moleculares.

List of publications by author

Publications related to this thesis

- M Ellner, P Pou, R Perez, "The Electrostatic Field of CO Functionalized Metal Tips," in Kelvin Probe Force Microscopy, edited by Sadewasser S., Glatzel T. (Springer, Cham, 2018) pp. 465-497.
- M Ellner, P Pou, R Pérez, "Atomic force microscopy contrast with CO functionalized tips in hydrogen-bonded molecular layers: Does the real tip charge distribution play a role?", Phys. Rev. B **96**, 075418 (2017).
- B. de la Torre, M. Ellner, P. Pou, N. Nicoara, R. Pérez, and J. M. Gómez-Rodríguez, "Atomic-Scale Variations of the Mechanical Response of 2D Materials Detected by Noncontact Atomic Force Microscopy", Phys. Rev. Lett. **116**, 245502 (2016).
- Michael Ellner, Niko Pavliček, Pablo Pou, Bruno Schuler, Nikolaj Moll, Gerhard Meyer, Leo Gross, Rubén Pérez, "The Electric Field of CO Tips and Its Relevance for Atomic Force Microscopy", Nano letters, **16**, 1974 (2016).
- M Ellner, P Pou, R Pérez, "High resolution atomic force microscopy images studied with a charge density based method: molecular identification, bond order and apparent intermolecular features", submitted for publication.

Publications not related to this thesis

- M Ellner, N Bolívar, B Berche, E Medina, "Charge-and spin-polarized currents in mesoscopic rings with Rashba spin-orbit interactions coupled to an electron reservoir", Phys. Rev. B **90**, 085305 (2014).

- Iván Sánchez, Claudia Colonnello, Michael Ellner, Bruno Guerrero, "Improved model for the U-tube granular instability II: Inclusion of the grain size dependency", submitted for publication.

Bibliography

[1] G. Binnig, H. Rohrer, C. Gerber, and E. Weibel, Phys. Rev. Lett. **49**, 57 (1982).

[2] G. Binnig, "Atomic force microscope and method for imaging surfaces with atomic resolution," (1985).

[3] G. Binnig, C. F. Quate, and C. Gerber, Phys. Rev. Lett. **56**, 930 (1986).

[4] E. Meyer, Prog. Surf. Sci. **41**, 3 (1992).

[5] R. García and R. Pérez, Surf. Sci. Rep. **47**, 197 (2002).

[6] F. J. Giessibl, Rev. Mod. Phys. **75**, 949 (2003), arXiv:0305119 [cond-mat] .

[7] B. Bhushan and O. Marti, "Scanning Probe Microscopy — Principle of Operation, Instrumentation and Probes," in *Springer Handb. Nanotechnol.*, edited by B. Bhushan (Springer Berlin Heidelberg, Berlin, Heidelberg, 2017) pp. 725–768.

[8] G. Binnig and D. P. E. Smith, Rev. Sci. Instrum. **57**, 1688 (1986).

[9] T. Göddenhenrich, H. Lemke, U. Hartmann, and C. Heiden, J. Vac. Sci. Technol. A Vacuum, Surfaces, Film. **8**, 383 (1990).

[10] T. Albrecht, P. Grütter, D. Rugar, and D. Smith, Ultramicroscopy **42-44**, 1638 (1992).

[11] R. Erlandsson, G. M. McClelland, C. M. Mate, and S. Chiang, J. Vac. Sci. Technol. A Vacuum, Surfaces, Film. **6**, 266 (1988).

[12] D. Rugar, H. J. Mamin, and P. Guethner, Appl. Phys. Lett. **55**, 2588 (1989).

[13] C. Schönenberger and S. F. Alvarado, Rev. Sci. Instrum. **60**, 3131 (1989).

[14] D. Sarid, L. S. Bell, D. Iams, and V. Weissenberger, Opt. Lett. **13**, 1057 (1988).

[15] G. Meyer and N. M. Amer, Appl. Phys. Lett. **53**, 1045 (1988).

[16] W. A. Hofer, A. S. Foster, and A. L. Shluger, Rev. Mod. Phys. **75**, 1287 (2003).

[17] S. Morita, F. Giessibl, E. Meyer, and R. Wiesendanger, eds., *Noncontact Atomic Force Microscopy*, Vol. 3 (Springer-Verlag Berlin Heidelberg, 2015).

[18] O. Marti, B. Drake, and P. K. Hansma, Appl. Phys. Lett. **51**, 484 (1987).

[19] F. J. Giessibl, Phys. Rev. B **56**, 16010 (1997).

[20] D. Klinov and S. Magonov, Appl. Phys. Lett. **84**, 2697 (2004).

[21] K. Voïtchovsky, J. J. Kuna, S. A. Contera, E. Tosatti, and F. Stellacci, Nat. Nanotechnol. **5**, 401 (2010).

[22] T. R. Albrecht, P. Grütter, D. Horne, and D. Rugar, J. Appl. Phys. **69**, 668 (1991), arXiv:arXiv:1011.1669v3 .

[23] S. P. Jarvis, Int. J. Mol. Sci. **16**, 19936 (2015).

[24] C. C. C. Moreno, O. Stetsovych, T. K. Shimizu, O. Custance, and Ó. Custance, Nano Lett. **15**, 2257 (2015).

[25] M. Abe, Y. Sugimoto, O. Custance, and S. Morita, Appl. Phys. Lett. **87**, 173503 (2005).

[26] M. Z. Baykara and U. D. Schwarz, "3D Force Field Spectroscopy," in *Noncontact At. Force Microsc. Vol. 3*, edited by S. Morita, F. J. Giessibl,

E. Meyer, and R. Wiesendanger (Springer International Publishing, Cham, 2015) pp. 9–28.

[27] F. J. Giessibl, F. Pielmeier, T. Eguchi, T. An, and Y. Hasegawa, Phys. Rev. B **84**, 125409 (2011).

[28] F. J. Giessibl, Science **267**, 68 (1995).

[29] S.-i. Kitamura and M. Iwatsuki, Jpn. J. Appl. Phys. **34**, L145 (1995).

[30] P. Guthner, J. Vac. Sci. Technol. B Microelectron. Nanom. Struct. **14**, 2428 (1996).

[31] S. Kitamura and M. Iwatsuki, Jpn. J. Appl. Phys. **35**, L668 (1996).

[32] R. Lüthi, E. Meyer, M. Bammerlin, A. Baratoff, T. Lehmann, L. Howald, C. Gerber, and H.-J. Güntherodt, Zeitschrift für Phys. B Condens. Matter **100**, 165 (1996).

[33] W. Allers, A. Schwarz, U. D. Schwarz, and R. Wiesendanger, Rev. Sci. Instrum. **69**, 221 (1998).

[34] K.-i. Fukui, H. Onishi, and Y. Iwasawa, Phys. Rev. Lett. **79**, 4202 (1997).

[35] Y. Sugawara, M. Ohta, H. Ueyama, and S. Morita, Science **270**, 1646 (1995).

[36] F. J. Giessibl, H. Bielefeldt, S. Hembacher, and J. Mannhart, Appl. Surf. Sci. **140**, 352 (1999).

[37] F. J. Giessibl, Appl. Phys. Lett. **73**, 3956 (1998).

[38] U. Gysin, S. Rast, P. Ruff, E. Meyer, D. W. Lee, P. Vettiger, and C. Gerber, Phys. Rev. B **69**, 045403 (2004).

[39] K. Iwata, S. Yamazaki, P. Mutombo, P. Hapala, M. Ondráček, P. Jelínek, and Y. Sugimoto, Nat. Commun. **6**, 7766 (2015).

[40] L. Gross, F. Mohn, N. Moll, P. Liljeroth, and G. Meyer, Science **325**, 1110 (2009).

[41] G. Binnig, C. Gerber, E. Stoll, T. R. Albrecht, and C. F. Quate, Eur. Lett. **3**, 1281 (1987).

[42] M. D. Kirk, T. R. Albrecht, and C. F. Quate, Rev. Sci. Instrum. **59**, 833 (1988).

[43] G. Meyer and N. M. Amer, Appl. Phys. Lett. **56**, 2100 (1990).

[44] F. J. Giessibl, J. Vac. Sci. Technol. B Microelectron. Nanom. Struct. **9**, 984 (1991).

[45] M. Morgenstern, A. Schwarz, and U. D. Schwarz, "Low-Temperature Scanning Probe Microscopy," in *Springer Handb. Nanotechnol.*, edited by B. Bhushan (Springer Berlin Heidelberg, Berlin, Heidelberg, 2010) pp. 663–709.

[46] M. Z. Baykara, M. Morgenstern, A. Schwarz, and U. D. Schwarz, "Low-Temperature Scanning Probe Microscopy," in *Springer Handb. Nanotechnol.*, edited by B. Bhushan (Springer Berlin Heidelberg, Berlin, Heidelberg, 2017) pp. 769–808.

[47] L. Bartels, G. Meyer, and K.-H. Rieder, Appl. Phys. Lett. **71**, 213 (1997).

[48] D. M. Eigler and E. K. Schweizer, Nature **344**, 524 (1990).

[49] L. Bartels, G. Meyer, and K.-H. Rieder, Phys. Rev. Lett. **79**, 697 (1997).

[50] S.-i. Ishi, Y. Ohno, and B. Viswanathan, Surf. Sci. **161**, 349 (1985).

[51] G. Meyer, L. Bartels, and K.-H. Rieder, Superlattices Microstruct. **25**, 463 (1999).

[52] L. Bartels, G. Meyer, K.-H. Rieder, D. Velic, E. Knoesel, A. Hotzel, M. Wolf, and G. Ertl, Phys. Rev. Lett. **80**, 2004 (1998).

[53] L. Gross, N. Moll, F. Mohn, A. Curioni, G. Meyer, F. Hanke, and M. Persson, Phys. Rev. Lett. **107**, 086101 (2011).

[54] H. Mönig, D. R. Hermoso, O. Díaz Arado, M. Todorović, A. Timmer, S. Schüer, G. Langewisch, R. Pérez, and H. Fuchs, ACS Nano **10**, 1201 (2016).

[55] H. Mönig, S. Amirjalayer, A. Timmer, Z. Hu, L. Liu, O. Díaz Arado, M. Cnudde, C. A. Strassert, W. Ji, M. Rohlfing, and H. Fuchs, Nature Nanotechnology (2018), 10.1038/s41565-018-0104-4.

[56] M. Z. Baykara, M. Todorović, H. Mönig, T. C. Schwendemann, Ö. Ünverdi, L. Rodrigo, E. I. Altman, R. Pérez, and U. D. Schwarz, Phys. Rev. B **87**, 155414 (2013).

[57] J. D. Teeter, P. S. Costa, P. Zahl, T. H. Vo, M. Shekhirev, W. Xu, X. C. Zeng, A. Enders, and A. Sinitskii, Nanoscale **9**, 18835 (2017).

[58] F. Mohn, B. Schuler, L. Gross, and G. Meyer, Appl. Phys. Lett. **102**, 73109 (2013).

[59] B. Schuler, W. Liu, A. Tkatchenko, N. Moll, G. Meyer, A. Mistry, D. Fox, and L. Gross, Phys. Rev. Lett. **111**, 106103 (2013).

[60] L. Gross, B. Schuler, F. Mohn, N. Moll, N. Pavliček, W. Steurer, I. Scivetti, K. Kotsis, M. Persson, and G. Meyer, Phys. Rev. B **90**, 155455 (2014), arXiv:1408.7053 .

[61] P. Hapala, M. Ondráček, O. Stetsovych, M. Švec, and P. Jelínek, "Simultaneous nc-AFM/STM Measurements with Atomic Resolution," in *Noncontact At. Force Microsc. Vol. 3*, edited by S. Morita, F. J. Giessibl, E. Meyer, and R. Wiesendanger (Springer International Publishing, Cham, 2015) pp. 29–49.

[62] P. Hapala, M. Švec, O. Stetsovych, N. J. van der Heijden, M. Ondráček, J. van der Lit, P. Mutombo, I. Swart, and P. Jelínek, Nat. Commun. **7**, 11560 (2016).

[63] J. Van Der Lit, F. Di Cicco, P. Hapala, P. Jelínek, and I. Swart, Phys. Rev. Lett. **116**, 2 (2016).

[64] D. Z. Gao, J. Grenz, M. B. Watkins, F. F. Canova, A. Schwarz, R. Wiesendanger, A. L. Shluger, G. Street, L. Wc, U. Kingdom, A. Physics, F. Federici Canova, A. Schwarz, R. Wiesendanger, and A. L. Shluger, ACS Nano **8**, 5339 (2014).

[65] S. Kawai, A. Sadeghi, X. Feng, P. Lifen, R. Pawlak, T. Glatzel, A. Willand, A. Orita, J. Otera, S. Goedecker, and E. Meyer, ACS Nano **7**, 9098 (2013).

[66] A. M. Sweetman, S. P. Jarvis, H. Sang, I. Lekkas, P. Rahe, Y. Wang, J. Wang, N. R. Champness, L. Kantorovich, and P. Moriarty, Nat. Commun. **5**, 3931 (2014).

[67] A. Sweetman, S. P. Jarvis, P. Rahe, N. R. Champness, L. Kantorovich, and P. Moriarty, Phys. Rev. B **90**, 1 (2014).

[68] C. Chiutu, A. M. Sweetman, A. J. Lakin, A. Stannard, S. Jarvis, L. Kantorovich, J. L. Dunn, and P. Moriarty, Phys. Rev. Lett. **108**, 268302 (2012).

[69] J. Welker, A. J. Weymouth, and F. J. Giessibl, ACS Nano **7**, 7377 (2013).

[70] L. N. Kantorovich and T. Trevethan, Phys. Rev. Lett. **93**, 1 (2004).

[71] N. Oyabu, P. Pou, Y. Sugimoto, P. Jelínek, M. Abe, S. Morita, R. Pérez, and Ó. Custance, Phys. Rev. Lett. **96**, 1 (2006).

[72] M. Gauthier, L. Kantorovich, and M. Tsukada (Springer, Berlin, Heidelberg, 2002) pp. 371–394.

[73] W. Denk and D. W. Pohl, Appl. Phys. Lett. **59**, 2171 (1991).

[74] T. D. Stowe, T. W. Kenny, D. J. Thomson, and D. Rugar, Appl. Phys. Lett. **75**, 2785 (1999).

[75] R. LÜTHI, E. MEYER, M. BAMMERLIN, A. BARATOFF, L. HOWALD, C. H. GERBER, and H.-J. GÜNTHERODT, Surf. Rev. Lett. **04**, 1025 (1997).

[76] R. Bennewitz, A. S. Foster, L. N. Kantorovich, M. Bammerlin, C. Loppacher, S. Schär, M. Guggisberg, E. Meyer, and A. L. Shluger, Phys. Rev. B **62**, 2074 (2000).

[77] S. Hembacher, F. J. Giessibl, J. Mannhart, and C. F. Quate, Phys. Rev. Lett. **94**, 56101 (2005).

[78] M. Gauthier and M. Tsukada, Phys. Rev. B **60**, 11716 (1999).

[79] C. Loppacher, M. Bammerlin, M. Guggisberg, S. Schär, R. Bennewitz, A. Baratoff, E. Meyer, and H. J. Güntherodt, Phys. Rev. B - Condens. Matter Mater. Phys. **62**, 16944 (2000).

[80] S. A. Ghasemi, S. Goedecker, A. Baratoff, T. Lenosky, E. Meyer, and H. J. Hug, Phys. Rev. Lett. **100**, 236106 (2008).

[81] G. H. Vineyard, Journal of Physics and Chemistry of Solids **3**, 121 (1957).

[82] W. Allers, A. Schwarz, U. Schwarz, and R. Wiesendanger, Appl. Surf. Sci. **140**, 247 (1999).

[83] H. Hölscher, A. Schwarz, W. Allers, U. D. Schwarz, and R. Wiesendanger, Phys. Rev. B **61**, 12678 (2000).

[84] S. Hembacher, F. J. Giessibl, J. Mannhart, and C. F. Quate, Proc. Natl. Acad. Sci. **100**, 12539 (2003).

[85] S. Kawai and H. Kawakatsu, Phys. Rev. B **79**, 115440 (2009).

[86] S. Kawai, T. Glatzel, S. Koch, B. Such, A. Baratoff, and E. Meyer, Phys. Rev. B **81**, 085420 (2010).

[87] M. Ashino, A. Schwarz, T. Behnke, and R. Wiesendanger, Phys. Rev. Lett. **93**, 136101 (2004).

[88] M. P. Boneschanscher, J. Van Der Lit, Z. Sun, I. Swart, P. Liljeroth, and D. Vanmaekelbergh, ACS Nano **6**, 10216 (2012).

[89] J. van der Lit, M. P. Boneschanscher, D. Vanmaekelbergh, M. Ijäs, A. Uppstu, M. Ervasti, A. Harju, P. Liljeroth, and I. Swart, Nat. Commun. **4**, 2023 (2013).

[90] M. Ondráček, P. Pou, V. Rozsíval, C. González, P. Jelínek, and R. Pérez, Phys. Rev. Lett. **106**, 176101 (2011).

[91] J. Wintterlin and M.-L. Bocquet, Surf. Sci. **603**, 1841 (2009).

[92] S. Bae, H. Kim, Y. Lee, X. Xu, J.-S. Park, Y. Zheng, J. Balakrishnan, T. Lei, H. Ri Kim, Y. I. Song, Y.-J. Kim, K. S. Kim, B. Özyilmaz, J.-H. Ahn, B. H. Hong, and S. Iijima, Nat. Nanotechnol. **5**, 574 (2010).

[93] B. Wang, M. Caffio, C. Bromley, H. Früchtl, and R. Schaub, ACS Nano **4**, 5773 (2010).

[94] A. Martin-Recio, C. Romero-Muniz, A. J. Martinez-Galera, P. Pou, R. Perez, and J. M. Gomez-Rodriguez, Nanoscale **7**, 11300 (2015).

[95] B. B. Miranda, S. Barja, M. Garnica, M. Minniti, A. Politano, J. M. Rodriguez-García, J. J. Hinarejos, D. Farías, A. L. V. de Parga, and Rodolfo, New J. Phys. **12**, 93018 (2010).

[96] I. Pletikosi\ifmmode \acutec\else ć\fi, M. Kralj, P. Pervan, R. Brako, J. Coraux, A. T. N'Diaye, C. Busse, and T. Michely, Phys. Rev. Lett. **102**, 56808 (2009).

[97] M. M. Ugeda, D. Fernández-Torre, I. Brihuega, P. Pou, A. J. Mart\'\inez-Galera, R. Pérez, and J. M. Gómez-Rodr\'\iguez, Phys. Rev. Lett. **107**, 116803 (2011).

[98] A. H. Castro Neto, N. M. R. Peres, K. S. Novoselov, and A. K. Geim, Rev. Mod. Phys. **81**, 109 (2009), arXiv:0709.1163 .

[99] S. K. Hämäläinen, M. P. Boneschanscher, P. H. Jacobse, I. Swart, K. Pussi, W. Moritz, J. Lahtinen, P. Liljeroth, and J. Sainio, Phys. Rev. B **88**, 201406 (2013).

[100] F. Jean, T. Zhou, N. Blanc, R. Felici, J. Coraux, and G. Renaud, Phys. Rev. B **91**, 245424 (2015).

[101] M. Enachescu, D. Schleef, D. F. Ogletree, and M. Salmeron, Phys. Rev. B **60**, 16913 (1999).

[102] S. Koch, D. Stradi, E. Gnecco, S. Barja, S. Kawai, C. Díaz, M. Alcamí, F. Martín, A. L. Vázquez de Parga, R. Miranda, T. Glatzel, and E. Meyer, ACS Nano **7**, 2927 (2013).

[103] E. N. Voloshina, Y. S. Dedkov, S. Torbrügge, A. Thissen, and M. Fonin, Appl. Phys. Lett. **100**, 241606 (2012).

[104] E. N. Voloshina, E. Fertitta, A. Garhofer, F. Mittendorfer, M. Fonin, A. Thissen, and Y. S. Dedkov, Sci. Rep. **3**, 1072 (2013).

[105] U. Landman, W. D. Luedtke, N. A. Burnham, and R. J. Colton, Science **248**, 454 LP (1990).

[106] R. Garcia and E. T. Herruzo, Nat. Nanotechnol. **7**, 217 (2012).

[107] T. Herden, M. Ternes, and K. Kern, Nano Lett. **14**, 3623 (2014).

[108] S. Morita, R. Wiesendanger, and E. Meyer, eds., *Noncontact Atomic Force Microscopy*, Vol. 1 (Springer-Verlag Berlin Heidelberg, 2002).

[109] S. Morita, F. Giessibl, and R. Wiesendanger, eds., *Noncontact Atomic Force Microscopy*, Vol. 2 (Springer-Verlag Berlin Heidelberg, 2009).

[110] J. Repp, G. Meyer, S. M. Stojkovi\ifmmode \acutec\else ć\fi, A. Gourdon, and C. Joachim, Phys. Rev. Lett. **94**, 26803 (2005).

[111] L. Gross, F. Mohn, N. Moll, G. Meyer, R. Ebel, W. M. Abdel-Mageed, and M. Jaspars, Nat Chem **2**, 821 (2010).

[112] M. Emmrich, F. Huber, F. Pielmeier, J. Welker, T. Hofmann, M. Schneiderbauer, D. Meuer, S. Polesya, S. Mankovsky, D. Ködderitzsch, H. Ebert, and F. J. Giessibl, Science **348**, 308 (2015).

[113] B. Schuler, G. Meyer, D. Peña, O. C. Mullins, and L. Gross, J. Am. Chem. Soc. **137**, 9870 (2015).

[114] F. Mohn, J. Repp, L. Gross, G. Meyer, M. S. Dyer, and M. Persson, Phys. Rev. Lett. **105**, 266102 (2010).

[115] O. Guillermet, S. Gauthier, C. Joachim, P. de Mendoza, T. Lauterbach, and A. Echavarren, Chem. Phys. Lett. **511**, 482 (2011).

[116] F. Mohn, L. Gross, N. Moll, and G. Meyer, Nat Nano **7**, 227 (2012).

[117] K. Ø. Hanssen, B. Schuler, A. J. Williams, T. B. Demissie, E. Hansen, J. H. Andersen, J. Svenson, K. Blinov, M. Repisky, F. Mohn, G. Meyer, J.-S. Svendsen, K. Ruud, M. Elyashberg, L. Gross, M. Jaspars, and J. Isaksson, Angew. Chemie Int. Ed. **51**, 12238 (2012).

[118] N. Pavliček, B. Fleury, M. Neu, J. Niedenführ, C. Herranz-Lancho, M. Ruben, and J. Repp, Phys. Rev. Lett. **108**, 86101 (2012).

[119] L. Gross, F. Mohn, N. Moll, B. Schuler, A. Criado, E. Guitian, D. Pena, A. Gourdon, G. Meyer, D. Peña, A. Gourdon, and G. Meyer, Science **337**, 1326 (2012).

[120] D. G. de Oteyza, P. Gorman, Y.-C. Chen, S. Wickenburg, A. Riss, D. J. Mowbray, G. Etkin, Z. Pedramrazi, H.-Z. Tsai, A. Rubio, M. F. Crommie, and F. R. Fischer, Science **340**, 1434 (2013).

[121] N. Pavliček, C. Herranz-Lancho, B. Fleury, M. Neu, J. Niedenführ, M. Ruben, and J. Repp, Phys. status solidi **250**, 2424 (2013).

[122] F. Albrecht, M. Neu, C. Quest, I. Swart, and J. Repp, J. Am. Chem. Soc. **135**, 9200 (2013).

[123] J. Zhang, P. Chen, B. Yuan, W. Ji, Z. Cheng, and X. Qiu, Science **342**, 611 (2013).

[124] G. Kichin, C. Wagner, F. S. Tautz, and R. Temirov, Phys. Rev. B **87**, 81408 (2013).

[125] B. Schuler, S. Collazos, L. Gross, G. Meyer, D. Pérez, E. Guitián, and D. Peña, Angew. Chemie **126**, 9150 (2014).

[126] A. Riss, S. Wickenburg, P. Gorman, L. Z. Tan, H.-Z. Tsai, D. G. de Oteyza, Y.-C. Chen, A. J. Bradley, M. M. Ugeda, G. Etkin, S. G. Louie, F. R. Fischer, and M. F. Crommie, Nano Lett. **14**, 2251 (2014).

[127] S. K. Hämäläinen, N. van der Heijden, J. van der Lit, S. den Hartog, P. Liljeroth, and I. Swart, Phys. Rev. Lett. **113**, 186102 (2014).

[128] M. Neu, N. Moll, L. Gross, G. Meyer, F. J. Giessibl, and J. Repp, Phys. Rev. B **89**, 205407 (2014).

[129] N. Moll, B. Schuler, S. Kawai, F. Xu, L. Peng, A. Orita, J. Otera, A. Curioni, M. Neu, J. Repp, G. Meyer, and L. Gross, Nano Lett. **14**, 6127 (2014).

[130] B. Schuler, S.-X. Liu, Y. Geng, S. Decurtins, G. Meyer, and L. Gross, Nano Lett. **14**, 3342 (2014).

[131] N. Pavliček, B. Schuler, S. Collazos, N. Moll, D. Pérez, E. Guitián, G. Meyer, D. Peña, and L. Gross, Nat. Chem. **7**, 623 (2015).

[132] S. Kawai, A. Sadeghi, F. Xu, L. Peng, A. Orita, J. Otera, S. Goedecker, and E. Meyer, ACS Nano **9**, 2574 (2015).

[133] F. Albrecht, N. Pavliček, C. Herranz-Lancho, M. Ruben, and J. Repp, J. Am. Chem. Soc. **137**, 7424 (2015).

[134] A. Mistry, B. Moreton, B. Schuler, F. Mohn, G. Meyer, L. Gross, A. Williams, P. Scott, G. Costantini, and D. J. Fox, Chem. – A Eur. J. **21**, 2011 (2015).

[135] C. Rogers, C. Chen, Z. Pedramrazi, A. A. Omrani, H.-Z. Tsai, H. S. Jung, S. Lin, M. F. Crommie, and F. R. Fischer, Angew. Chemie Int. Ed. **54**, 15143 (2015).

[136] S. P. Jarvis, A. M. Sweetman, I. Lekkas, N. R. Champness, L. Kantorovich, and P. Moriarty, J. Phys. Condens. Matter **27**, 54004 (2015).

[137] F. Albrecht, J. Repp, M. Fleischmann, M. Scheer, M. Ondráček, and P. Jelínek, Phys. Rev. Lett. **115**, 76101 (2015).

[138] S. Kawai, V. Haapasilta, B. D. Lindner, K. Tahara, P. Spijker, J. A. Buitendijk, R. Pawlak, T. Meier, Y. Tobe, A. S. Foster, and E. Meyer, Nat. Commun. **7**, 12711 (2016).

[139] J. Krüger, N. Pavliček, J. M. Alonso, D. Pérez, E. Guitián, T. Lehmann, G. Cuniberti, A. Gourdon, G. Meyer, L. Gross, F. Moresco, and D. Peña, ACS Nano **10**, 4538 (2016).

[140] J. N. Ladenthin, T. Frederiksen, M. Persson, J. C. Sharp, S. Gawinkowski, J. Waluk, and T. Kumagai, Nat Chem **8**, 935 (2016).

[141] B. Schuler, S. Fatayer, F. Mohn, N. Moll, N. Pavliček, G. Meyer, D. Peña, and L. Gross, Nat Chem **8**, 220 (2016).

[142] A. Riss, A. P. Paz, S. Wickenburg, H.-Z. Tsai, D. G. De Oteyza, A. J. Bradley, M. M. Ugeda, P. Gorman, H. S. Jung, M. F. Crommie, A. Rubio, and F. R. Fischer, Nat Chem **8**, 678 (2016).

[143] Z. Majzik, A. B. Cuenca, N. Pavliček, N. Miralles, G. Meyer, L. Gross, and E. Fernández, ACS Nano **10**, 5340 (2016).

[144] N. J. van der Heijden, P. Hapala, J. A. Rombouts, J. van der Lit, D. Smith, P. Mutombo, M. Švec, P. Jelínek, and I. Swart, ACS Nano **10**, 8517 (2016).

[145] J. Liu, T. Dienel, J. Liu, O. Groening, J. Cai, X. Feng, K. Müllen, P. Ruffieux, and R. Fasel, J. Phys. Chem. C **120**, 17588 (2016).

[146] A. Shiotari and Y. Sugimoto, Nat. Commun. **8**, 14313 (2017).

[147] B. Schuler, Y. Zhang, S. Collazos, S. Fatayer, G. Meyer, D. Perez, E. Guitian, M. R. Harper, J. D. Kushnerick, D. Pena, L. Gross, D. Peña, and L. Gross, Chem. Sci. **8**, (2017).

[148] S. Zint, D. Ebeling, T. Schlöder, S. Ahles, D. Mollenhauer, H. A. Wegner, and A. Schirmeisen, ACS Nano (2017).

[149] X.-Y. Wang, M. Richter, Y. He, J. Björk, A. Riss, R. Rajesh, M. Garnica, F. Hennersdorf, J. J. Weigand, A. Narita, R. Berger, X. Feng, W. Auwärter, J. V. Barth, C.-A. Palma, and K. Müllen, Nat. Commun. **8**, 1948 (2017).

[150] L. L. Patera, Z. Zou, C. Dri, C. Africh, J. Repp, and G. Comelli, Phys. Chem. Chem. Phys. **19**, 24605 (2017).

[151] R. Zuzak, R. Dorel, M. Krawiec, B. Such, M. Kolmer, M. Szymonski, A. M. Echavarren, and S. Godlewski, ACS Nano **11**, 9321 (2017).

[152] J. I. Urgel, H. Hayashi, M. Di Giovannantonio, C. A. Pignedoli, S. Mishra, O. Deniz, M. Yamashita, T. Dienel, P. Ruffieux, H. Yamada, and R. Fasel, J. Am. Chem. Soc. **139**, 11658 (2017).

[153] Q. Sun, B. V. Tran, L. Cai, H. Ma, X. Yu, C. Yuan, M. Stöhr, and W. Xu, Angew. Chemie Int. Ed. **56**, 12165 (2017).

[154] M. Liu, M. Liu, L. She, Z. Zha, J. Pan, S. Li, T. Li, Y. He, Z. Cai, J. Wang, Y. Zheng, X. Qiu, and D. Zhong, Nat. Commun. **8**, 14924 (2017).

[155] J. Peng, J. Guo, P. Hapala, D. Cao, R. Ma, B. Cheng, L. Xu, M. Ondráček, P. Jelínek, E. Wang, and Y. Jiang, Nat. Commun. **9**, 122 (2018).

[156] M. Di Giovannantonio, J. I. Urgel, U. Beser, A. V. Yakutovich, J. Wilhelm, C. A. Pignedoli, P. Ruffieux, A. Narita, K. Müllen, and R. Fasel, J. Am. Chem. Soc. , jacs.8b00587 (2018).

[157] Q. Sun, X. Yu, M. Bao, M. Liu, J. Pan, Z. Zha, L. Cai, H. Ma, C. Yuan, X. Qiu, and W. Xu, Angew. Chemie Int. Ed. (2018).

[158] S. Freund, A. Hinaut, N. Marinakis, E. C. Constable, E. Meyer, C. E. Housecroft, and T. Glatzel, Beilstein J. Nanotechnol. **9**, 242 (2018).

[159] Z. Majzik, N. Pavliček, M. Vilas-Varela, D. Pérez, N. Moll, E. Guitián, G. Meyer, D. Peña, and L. Gross, Nat. Commun. **9**, 1198 (2018).

[160] P. Hapala, G. Kichin, C. Wagner, F. S. Tautz, R. Temirov, and P. Jelínek, Phys. Rev. B **90**, 85421 (2014).

[161] S. P. Jarvis, M. A. Rashid, A. Sweetman, J. Leaf, S. Taylor, P. Moriarty, and J. Dunn, Phys. Rev. B **92**, 241405 (2015).

[162] C.-G. Wang, Z.-H. Cheng, X.-H. Qiu, and W. Ji, Chinese Chem. Lett. **342**, (2016).

[163] Z. Han, X. Wei, C. Xu, C.-l. Chiang, Y. Zhang, R. Wu, and W. Ho, J. Phys. Chem. Lett. **7**, 5205 (2016).

[164] P. Hapala, R. Temirov, F. S. Tautz, and P. Jelínek, Phys. Rev. Lett. **113**, 226101 (2014).

[165] A. J. Lee, Y. Sakai, M. Kim, and J. R. Chelikowsky, Appl. Phys. Lett. **108**, 193102 (2016).

[166] C.-S. Guo, X. Xin, M. A. Van Hove, X. Ren, and Y. Zhao, J. Phys. Chem. C **119**, 14195 (2015).

[167] P. Jelínek, J. Phys. Condens. Matter **29**, 343002 (2017).

[168] R. Lindner and A. Kühnle, ChemPhysChem **16**, 1582 (2015).

[169] N. Pavliček and L. Gross, Nat. Rev. Chem. **1** (2017).

[170] Q. Shen, H.-Y. Gao, and H. Fuchs, Nano Today (2017).

[171] N. Kocić, X. Liu, S. Chen, S. Decurtins, O. Krejčí, P. Jelínek, J. Repp, and S.-X. Liu, J. Am. Chem. Soc. **138**, 5585 (2016).

[172] Y. He, M. Garnica, F. Bischoff, J. Ducke, M.-L. Bocquet, M. Batzill, W. Auwärter, and J. V. Barth, Nat Chem **9**, 33 (2017).

[173] S. Kawai, S. Saito, S. Osumi, S. Yamaguchi, A. S. Foster, P. Spijker, and E. Meyer, Nat. Commun. **6**, 8098 (2015).

[174] C. Sánchez-Sánchez, T. Dienel, O. Deniz, P. Ruffieux, R. Berger, X. Feng, K. Müllen, and R. Fasel, ACS Nano **10**, 8006 (2016).

[175] P. Ruffieux, S. Wang, B. Yang, C. Sánchez-Sánchez, J. Liu, T. Dienel, L. Talirz, P. Shinde, C. A. Pignedoli, D. Passerone, T. Dumslaff, X. Feng, K. Müllen, and R. Fasel, Nature **531**, 489 (2016).

[176] E. I. Altman, M. Z. Baykara, and U. D. Schwarz, Acc. Chem. Res. **48**, 2640 (2015).

[177] J. Björk, J. Phys. Condens. Matter **28**, 83002 (2016).

[178] Y. Sugimoto, P. Pou, M. Abe, P. Jelínek, R. Pérez, S. Morita, and Ó. Custance, Nature **446**, 64 (2007).

[179] L. Gross, B. Schuler, N. Pavliček, S. Fatayer, Z. Majzik, N. Moll, D. Peña, and G. Meyer, Angew. Chemie Int. Ed. (2018).

[180] N. Pavliček, A. Mistry, Z. Majzik, N. Moll, G. Meyer, D. J. Fox, and L. Gross, Nat. Nanotechnol. **12**, 308 (2017).

[181] C. S. Guo, M. A. Van Hove, R. Q. Zhang, and C. Minot, Langmuir **26**, 16271 (2010).

[182] N. J. van der Heijden, D. Smith, G. Calogero, R. S. Koster, D. Vanmaekelbergh, M. A. van Huis, and I. Swart, Phys. Rev. B **93**, 245430 (2016).

[183] D. Ebeling, Q. Zhong, S. Ahles, L. Chi, H. A. Wegner, and A. Schirmeisen, Appl. Phys. Lett. **110**, 183102 (2017).

[184] H. Labidi, M. Koleini, T. Huff, M. Cloutier, J. Pitters, R. A. Wolkow, M. Salomons, M. Cloutier, J. Pitters, and R. A. Wolkow, Nat. Commun. **8**, 14222 (2017).

[185] N. Hauptmann, R. Robles, P. Abufager, N. Lorente, and R. Berndt, J. Phys. Chem. Lett. **7**, 1984 (2016).

[186] N. Moll, L. Gross, F. Mohn, A. Curioni, and G. Meyer, New J. Phys. **12**, 125020 (2010).

[187] Y. Sakai, A. J. Lee, and J. R. Chelikowsky, Nano Lett. **16**, 3242 (2016).

[188] C.-S. S. Guo, M. A. Van Hove, X. Ren, and Y. Zhao, J. Phys. Chem. C **119**, 1483 (2015).

[189] M. P. Boneschanscher, S. K. Hämäläinen, P. Liljeroth, and I. Swart, ACS Nano **8**, 3006 (2014).

[190] N. Moll, L. Gross, F. Mohn, A. Curioni, and G. Meyer, New J. Phys. **14**, 83023 (2012).

[191] M. Ashino, A. Schwarz, H. Hölscher, U. D. Schwarz, and R. Wiesendanger, Nanotechnology **16**, S134 (2005).

[192] S. Ciraci, A. Baratoff, and I. P. Batra, Phys. Rev. B **41**, 2763 (1990).

[193] F. Loske, R. Bechstein, J. Schütte, F. Ostendorf, M. Reichling, and A. Kühnle, Nanotechnology **20**, 65606 (2009).

[194] S. Park and C. F. Quate, Appl. Phys. Lett. **48**, 112 (1986).

[195] H. J. Mamin, E. Ganz, D. W. Abraham, R. E. Thomson, and J. Clarke, Phys. Rev. B **34**, 9015 (1986).

[196] D. Tománek, S. G. Louie, H. J. Mamin, D. W. Abraham, R. E. Thomson, E. Ganz, and J. Clarke, Phys. Rev. B **35**, 7790 (1987).

[197] E. Cisternas, F. Stavale, M. Flores, C. A. Achete, and P. Vargas, Phys. Rev. B **79**, 205431 (2009).

[198] H. A. Mizes, S.-i. Park, and W. A. Harrison, Phys. Rev. B **36**, 4491 (1987).

[199] P. Ouseph, T. Poothackanal, and G. Mathew, Phys. Lett. A **205**, 65 (1995).

[200] J. Paredes, A. Martínez-Alonso, and J. Tascón, Carbon N. Y. **39**, 476 (2001).

[201] Y. Wang, Y. Ye, and K. Wu, Surf. Sci. **600**, 729 (2006).

[202] P. Mallet, F. Varchon, C. Naud, L. Magaud, C. Berger, and J.-Y. Veuillen, Phys. Rev. B **76**, 041403 (2007).

[203] V. W. Brar, Y. Zhang, Y. Yayon, T. Ohta, J. L. McChesney, A. Bostwick, E. Rotenberg, K. Horn, and M. F. Crommie, Appl. Phys. Lett. **91**, 122102 (2007).

[204] J. Tersoff and D. R. Hamann, Phys. Rev. B **31**, 805 (1985).

[205] J. M. Blanco, C. González, P. Jelínek, J. Ortega, F. Flores, and R. Pérez, Phys. Rev. B **70**, 085405 (2004).

[206] H. Hölscher, W. Allers, U. D. Schwarz, A. Schwarz, and R. Wiesendanger, Phys. Rev. Lett. **83**, 4780 (1999).

[207] B. J. Albers, T. C. Schwendemann, M. Z. Baykara, N. Pilet, M. Liebmann, E. I. Altman, and U. D. Schwarz, Nat Nano **4**, 307 (2009).

[208] P. Pou, S. A. Ghasemi, P. Jelínek, T. Lenosky, S. Goedecker, and R. Pérez, Nanotechnology **20**, 264015 (2009).

[209] J. P. Perdew, K. Burke, and M. Ernzerhof, Phys. Rev. Lett. **77**, 3865 (1996).

[210] A. K. Geim and K. S. Novoselov, Nat. Mater. **6**, 183 (2007).

[211] P. Merino, M. Švec, A. L. Pinardi, G. Otero, and J. A. Martín-Gago, ACS Nano **5**, 5627 (2011).

[212] C. Lee, X. Wei, J. W. Kysar, and J. Hone, Science **321**, 385 (2008).

[213] A. L. Vázquez de Parga, F. Calleja, B. Borca, M. C. G. Passeggi, J. J. Hinarejos, F. Guinea, and R. Miranda, Phys. Rev. Lett. **100**, 056807 (2008).

[214] T. Land, T. Michely, R. Behm, J. Hemminger, and G. Comsa, Surf. Sci. **264**, 261 (1992).

[215] M. Castelaín, G. Martínez, P. Merino, J. Á. Martín-Gago, J. L. Segura, G. Ellis, and H. J. Salavagione, Chem. – A Eur. J. **18**, 4965 (2012).

[216] G. Giovannetti, P. A. Khomyakov, G. Brocks, V. M. Karpan, J. van den Brink, and P. J. Kelly, Phys. Rev. Lett. **101**, 026803 (2008).

[217] P. Sutter, J. T. Sadowski, and E. Sutter, Phys. Rev. B **80**, 245411 (2009).

[218] J. M. Blanco, F. Flores, and R. Pérez, Prog. Surf. Sci. **81**, 403 (2006).

[219] I. Horcas, R. Fernández, J. M. Gómez-Rodríguez, J. Colchero, J. Gómez-Herrero, and A. M. Baro, Rev. Sci. Instrum. **78**, 013705 (2007).

[220] A. J. Martínez-Galera and J. M. Gómez-Rodríguez, J. Phys. Chem. C **115**, 23036 (2011).

[221] J. P. Cleveland, S. Manne, D. Bocek, and P. K. Hansma, Rev. Sci. Instrum. **64**, 403 (1993).

[222] T. Ozaki, Phys. Rev. B **67**, 155108 (2003).

[223] S. Grimme, J. Antony, S. Ehrlich, and H. Krieg, J. Chem. Phys. **132**, 154104 (2010).

[224] A. Labuda, Y. Miyahara, L. Cockins, and P. H. Grütter, Phys. Rev. B **84**, 125433 (2011).

[225] J. M. Soler, A. M. Baro, N. Garc\'\ia, and H. Rohrer, Phys. Rev. Lett. **57**, 444 (1986).

[226] G. J. Verbiest, J. N. Simon, T. H. Oosterkamp, and M. J. Rost, Nanotechnology **23**, 145704 (2012).

[227] L. Tetard, A. Passian, and T. Thundat, Nat. Nanotechnol. **5**, 105 (2009).

[228] W. Tian, M. Chengfu, H. Wei, C. Yuhang, and C. Jiaru, Microsc. Res. Tech. **80**, 66 (2016).

[229] C. Romero-Muñiz, A. Martín-Recio, P. Pou, J. Gómez-Rodríguez, and R. Pérez, Carbon N. Y. **101**, 129 (2016).

[230] A. Martín-Recio, C. Romero-Muñiz, P. Pou, R. Pérez, and J. M. Gómez-Rodríguez, Carbon N. Y. **130**, 362 (2018).

[231] A. J. Weymouth, T. Hofmann, and F. J. Giessibl, Science **343**, 1120 (2014).

[232] M. Schneiderbauer, M. Emmrich, A. J. Weymouth, and F. J. Giessibl, Phys. Rev. Lett. **112**, 166102 (2014), arXiv:1402.5246 .

[233] C. F. Hirjibehedin, C.-Y. Lin, A. F. Otte, M. Ternes, C. P. Lutz, B. A. Jones, and A. J. Heinrich, Science **317**, 1199 LP (2007).

[234] A. Soon, L. Wong, B. Delley, and C. Stampfl, Physical Review B **77**, 125423 (2008).

[235] C. F. Hirjibehedin, C. P. Lutz, and A. J. Heinrich, Science **312**, 1021 (2006).

[236] J. E. Sader and S. P. Jarvis, Appl. Phys. Lett. **84**, 1801 (2004).

[237] R. Smoluchowski, Phys. Rev. **60**, 661 (1941).

[238] G. Teobaldi, K. Lämmle, T. Trevethan, M. Watkins, A. Schwarz, R. Wiesendanger, and A. L. Shluger, Phys. Rev. Lett. **106**, 216102 (2011).

[239] A. Schwarz, A. Köhler, J. Grenz, R. Wiesendanger, A. Köhler, J. Grenz, and R. Wiesendanger, Appl. Phys. Lett. **105**, 11606 (2014).

[240] T. Hofmann, F. Pielmeier, and F. J. Giessibl, Phys. Rev. Lett. **112**, 66101 (2014).

[241] J. Welker and F. J. Giessibl, Science **336**, 444 (2012).

[242] T. Hofmann, F. Pielmeier, and F. J. Giessibl, Physical Review Letters **115**, 109901 (2015).

[243] J. Repp, G. Meyer, S. Paavilainen, F. E. Olsson, and M. Persson, Phys. Rev. Lett. **95**, 225503 (2005).

[244] F. J. Giessibl, Science **289**, 422 (2000).

[245] R. Bennewitz, V. Barwich, M. Bammerlin, C. Loppacher, M. Guggisberg, A. Baratoff, E. Meyer, and H.-J. Güntherodt, Surf. Sci. **438**, 289 (1999).

[246] Z. Li, H.-Y. T. Chen, K. Schouteden, K. Lauwaet, E. Janssens, C. Van Haesendonck, G. Pacchioni, and P. Lievens, ACS Nano **9**, 5318 (2015).

[247] B. Schuler, M. Persson, S. Paavilainen, N. Pavliček, L. Gross, G. Meyer, and J. Repp, Phys. Rev. B **91**, 235443 (2015).

[248] G. E. Scuseria, M. D. Miller, F. Jensen, and J. Geertsen, J. Chem. Phys. **94**, 6660 (1991).

[249] T. Trevethan, M. Watkins, and A. L. Shluger, Beilstein J. Nanotechnol. **3**, 329 (2012).

[250] Z. Sun, M. P. Boneschanscher, I. Swart, D. Vanmaekelbergh, and P. Liljeroth, Phys. Rev. Lett. **106**, 046104 (2011).

[251] J. T. Yates, Surf. Sci. **299**, 731 (1994).

[252] M. Ternes, C. P. Lutz, C. F. Hirjibehedin, F. J. Giessibl, and A. J. Heinrich, Science **319**, 1066 (2008).

[253] P. Deshlahra, J. Conway, E. E. Wolf, and W. F. Schneider, Langmuir **28**, 8408 (2012).

[254] A. J. Heinrich, C. P. Lutz, J. A. Gupta, and D. M. Eigler, Science **298**, 1381 (2002).

[255] G. Kresse and J. Furthmüller, Comput. Mater. Sci. **6**, 15 (1996).

[256] B. de la Torre, *Desarrollo de un microscopio de fuerzas atómicas de no contacto en ultra-alto vacío y baja temperatura: aplicación a superficies de grafeno/Pt(111)*, Doctoral dissertation, Universidad Autónoma de Madrid (2015).

[257] A. J. Martínez-Galera and J. M. Gómez-Rodríguez, J. Phys. Chem. C **115**, 11089 (2011).

[258] D. Wang, Q.-M. Xu, L.-J. Wan, C. Wang, and C.-L. Bai, Langmuir **18**, 5133 (2002).

[259] A. Martín-Recio, A. J. Martínez-Galera, and J. M. Gómez-Rodríguez, J. Phys. Chem. C **119**, 401 (2015).

[260] D. Drakova, Reports Prog. Phys. **64**, 205 (2001).

[261] I. Palacio, A. L. Pinardi, J. I. Martínez, A. Preobrajenski, A. Cossaro, A. Jancarik, I. Stará, I. Starý, J. Méndez, J. A. Martín-Gago, and M. F. López, Phys. Chem. Chem. Phys. **19**, 22454 (2017).